Search for Heavy Neutral Leptons with IceCube DeepCore

Dissertation
zur Erlangung des akademischen Grades
doctor rerum naturalium
(Dr. rer. nat.)

im Fach: Physik
Spezialisierung: Experimentalphysik

eingereicht an der
Mathematisch-Naturwissenschaftlichen Fakultät
der Humboldt-Universität zu Berlin

von
Leander Fischer M. Sc.
geboren am 24. Oktober 1992
in Heidelberg

Präsidentin der Humboldt-Universität zu Berlin
Prof. Dr. Julia von Blumenthal

Dekanin der Mathematisch-Naturwissenschaftlichen Fakultät
Prof. Dr. Caren Tischendorf

Copyright Notice
This book is released into the public domain using the CC-BY-4.0 code.

To view a copy of the CC-BY-4.0 code, visit:
`https://creativecommons.org/licenses/by/4.0/`

Colophon
This document was typeset with the help of KOMA-Script and LaTeX using the open-source kaobook template class.

The source code of this thesis is available at:
`https://github.com/LeanderFischer/phd_thesis`

Zusammenfassung

Zusammenfassung . . .

Abstract

Abstract . . .

Todo list

Contents

List of Figures

List of Tables

Standard Model Neutrinos and Beyond

1

1.1 The Standard Model

adjust final vertical position of this reference

The *Standard Model (SM)* of particle physics is a Yang-Mills theory [1] providing very accurate predictions of weak, strong, and *electromagnetic (EM)* interactions. It is a relativistic quantum field theory that relies on gauge invariance, where all matter is made up of fermions, which are divided into quarks and leptons, and bosons describe the interactions between the fermions that have to fulfil the overall symmetry of the theory. Leptons are excitations of Dirac-type fermion fields.

[1]: Yang et al. (1954), "Conservation of Isotopic Spin and Isotopic Gauge Invariance"

The initial idea of the theory is associated with the works of Weinberg [2], Glashow [3], and Salam [4], that proposed a unified description of EM and weak interactions as a theory of a spontaneously broken SU(2) x U(1) symmetry for leptons, predicting a neutral massive vector boson Z^0, a massive charged vector boson $W^{\pm}$, and a massless photon γ as the gauge bosons. The Higgs mechanism [5], describing the breaking of the symmetry, predicts the existence of an additional scalar particle, the Higgs boson, giving the $W^{\pm}$ and Z^0 bosons their mass. The Higgs boson was discovered in 2012 at the LHC.

[2]: Weinberg (1967), "A Model of Leptons"
[3]: Glashow (1961), "Partial-symmetries of weak interactions"
[5]: Higgs (1964), "Broken symmetries, massless particles and gauge fields"

Also cite this? Didn't find a good reference, only the press releases.

Gell-Mann and Zweig proposed the quark model in 1964 [6, 7], which was completed by the discovery of non-abelian gauge theories [8] to form the SU(3) symmetry of the strong interaction called *quantum chromodynamics (QCD)*. QDC describes the interaction between quarks and gluons which completed the full picture of the SM in the mid-1970s. Together with the electroweak theory, the SM is a $SU(3)_C$ x $SU(2)_L$ x $U(1)_Y$ local gauge symmetry, with the conserved quantities C, *color*, L, *left-handed chirality*, and Y, *weak hypercharge*

[6]: Gell-Mann (1964), "A Schematic Model of Baryons and Mesons"
[7]: Zweig (1964), "An SU(3) model for strong interaction symmetry and its breaking. Version 2"

In the following, the basic properties of the SM are described, following the derivations of [9, 10].

[9]: Giunti et al. (2007), *Fundamentals of Neutrino Physics and Astrophysics*
[10]: Schwartz (2013), *Quantum Field Theory and the Standard Model*

1.1.1 Fundamental Fields

Fermions in the SM are Weyl fields with either *left-handed (LH)* or *right-handed (RH)* chirality, meaning they are eigenvectors of the chirality operator γ_5 with $\gamma_5 \psi_{R/L} = \pm \psi_{R/L}$. Only LH particles transform under $SU(2)_L$. The Higgs field is a complex scalar field, a doublet of $SU(2)_L$, which is responsible for the spontaneous symmetry breaking of $SU(2)_L$ x $U(1)_Y$ to $U(1)_{EM}$. Local gauge transformations of the fields are given by

$$\psi \longrightarrow e^{ig\theta^a(x)T^a}\psi \,, \tag{1.1}$$

where g is the coupling constant, $\theta^a(x)$ are the parameters of the transformation, and T^a are the generators of the group, with a counting them. The number of bosons is dependent on the generators of the symmetry groups, while the strength is defined by the coupling constants. There are eight massless gluons corresponding to the generators of the $SU(3)_C$ group. These

mediate the strong force which conserves color charge. The W_1, W_2, W_3, and B boson fields of the SU(2)$_L$ x U(1)$_Y$ group are mixed into the massive bosons through spontaneous symmetry breaking as

$$W^{\pm} = \frac{1}{\sqrt{2}}(W_1 \mp iW_2) \tag{1.2}$$

and

$$Z^0 = \cos\theta_W W_3 - \sin\theta_W B \ , \tag{1.3}$$

with θ_W being the *Weinberg angle*. The massless photon field is given by

$$A = \sin\theta_W W_3 + \cos\theta_W B \tag{1.4}$$

and its conserved quantity is the EM charge Q, which depends on the weak hypercharge, Y, and the third component of the weak isospin, T_3, as $Q = T_3 + Y/2$.

	Type			Q
quarks	u	c	t	+2/3
	d	s	b	-1/3
leptons	ν_e	ν_μ	ν_τ	0
	e	μ	τ	-1

Table 1.1: Fermions in the Standard Model. Shown are all three generations of quarks and leptons with their electric charge Q.

Fermions are divided into six quarks and six leptons. Weak, strong, and EM force act on the quarks, and they are always found in bound form as baryons or mesons. Leptons do not participate in the strong interaction and only the electrically charged leptons are massive and are effected by the EM force, while neutrinos are massless and only interact via the weak force. Each charged lepton has an associated neutrino, which it interacts with in *charged-current (CC)* weak interactions, that will be explained in more detail in Section 1.1.4. The fermions are listed in Table 1.1.

1.1.2 Electroweak Symmetry Breaking

To elaborate the process of spontaneous symmetry breaking through which the gauge bosons of the weak interaction acquire their masses, the Lagrangian of the Higgs field is considered as

$$\mathscr{L}_{\text{Higgs}} = (D_\mu \Phi^\dagger)(D^\mu \Phi) - \lambda\left(\Phi^\dagger\Phi - \frac{v^2}{2}\right)^2 \ , \tag{1.5}$$

with parameters λ and v, where λ is assumed to be positive. Φ is the Higgs doublet, which is defined as

$$\Phi = \begin{pmatrix} \Phi^+ \\ \Phi^0 \end{pmatrix} , \tag{1.6}$$

with the charged component Φ^+ and the neutral component Φ^0. The covariant derivative is given by

$$D_\mu = \partial_\mu - ig_2\frac{\sigma^i}{2}W_\mu^i - \frac{1}{2}ig_1 B_\mu \ , \tag{1.7}$$

with the Pauli matrices σ^i and the gauge boson fields W_μ^i and B_μ of the SU(2)$_L$ and U(1)$_Y$ groups, respectively. The coupling constants g_2 and g_1 are the respective coupling constants which are related to the Weinberg angle as $\tan\theta_W = \frac{g_1}{g_2}$. The Higgs potential has a non-zero *vacuum expectation value (vev)* at the minimum of the potential at $\Phi^\dagger\Phi = \frac{v^2}{2}$. Since the vacuum is electrically neutral, it can only come from a neutral component of the Higgs

doublet as

$$\Phi_{\text{vev}} = \frac{1}{\sqrt{2}}\begin{pmatrix}0\\ v\end{pmatrix}. \tag{1.8}$$

1.1.3 Fermion Masses

The mass term for charged fermions with spin-1/2 is given by

$$\mathcal{L}_{\text{Dirac}} = m(\bar{\Psi}_R\Psi_L - \bar{\Psi}_L\Psi_R)\,, \tag{1.9}$$

composed of the product of left- and RH Weyl spinors $\Psi_{L/R}$. This term is not invariant under SU(2)$_L$ x U(1)$_Y$ gauge transformations, but adding a Yukawa term

$$\mathcal{L}_{\text{Yukawa}} = -y\bar{L}_L\Phi e_R + h.c.\,, \tag{1.10}$$

coupling the fermion fields to the Higgs field, recovers the invariance and gives the fermions their masses. Here, y is the Yukawa coupling constant and $\bar{L}_L$ is the SU(2)$_L$ doublet. With the vev, this results in the mass term for the charged leptons and down-type quarks of $-m_e(\bar{e}_L e_R + \bar{e}_R e_L)$ with $m_e = \frac{yv}{\sqrt{2}}$. With $\tilde{\Phi} = i\sigma_2\Phi^*$, a similar Yukawa term can be written as $-y\bar{L}_L\tilde{\Phi}u_R + h.c.$, which leads to the masses of the up-type quarks.

1.1.4 Weak Interactions after Symmetry-Breaking

Introduce SM EW NC/CC Lagrangian to build upon in the next chapter

Stuff from my MSc thesis to re-write:

In the SM, weak interactions are mediated by the three massive bosons $\mathbf{W}^+$, $\mathbf{W}^-$, and $\mathbf{Z}^0$ [12]. The large boson masses ($m_{\mathbf{W}} \sim 80\,\text{GeV}$, $m_{\mathbf{Z}} \sim 90\,\text{GeV}$) result in a short range of the force of about 10×10^{-18} m. Weak interactions carried by $\mathbf{W}^\pm$ bosons are called CC interactions, because charge is transferred between the interacting particles. In CC interactions, a neutrino is converted into its corresponding charged lepton or vice versa. Neutral current (NC) interactions are those mediated by $\mathbf{Z}^0$ bosons. Here no charge is transferred. The Feynman diagrams for CC and NC interactions are shown in Figure 1.1.

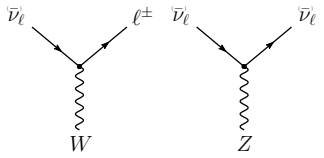

Figure 1.1: Feynman diagrams of charged-current (left) and neutral-current (right) neutrino weak interactions, taken from [11].

The observed phenomenon of neutrino oscillations (see Section Section 1.3.3) is based on the fact that there is a mass difference between the three neutrino mass eigenstates.

Plot is missing + for W and 0 for Z boson.

[12]: Thomson (2013), *Modern particle physics*

1.2 Beyond the Standard Model

Open questions related to neutrinos:

- question of neutrino nature, e.g. dirac or majorana?
- absolute mass values? (mass ordering + absolute mass scale)
- is there leptonic cp violation and what is the precise delta_cp value?
- what are the mixing angle values and is there a flavor principle
- is there additional effects like steriles, non-standard, lorentz violation

Are the fundamentals of the SM described above enough to explain *all* observed phenomena? Gravity cannot be explained by the SM, as it is incompatible with general relativity. Neither can the SM explain some cosmological observations like dark matter, and the matter-antimatter asymmetry, and it does not predict neutrinos to have mass, which is experimentally proven by neutrino oscillations, so some extensions to the SM is needed in order to explain them.

Cite and/or sidenote this.

Standard cosmology (ΛCDM) assumes that equal amounts of matter and anti-matter were produced in the early universe. However, the universe today is dominantly made up of matter. This so-called *baryon asymmetry* can be measured by the difference between the number densities of baryons and anti-baryons normalized to the number density of photons as

$$\eta_B = \frac{n_B - n_{\bar{B}}}{n_\gamma} \,, \tag{1.11}$$

where n_B, $n_{\bar{B}}$, and n_γ are the number densities of baryons, anti-baryons, and photons, respectively. Baryons are the dominant component with η_B being observed to be around 6×10^{-10}. Leptogenesis and EW baryogenesis are scenarios that could explain this phenomenon, where the former could be realized by the existence of heavy RH neutrinos.

cite this

The observation of neutrino flavor conversions and neutrino oscillations in a multitude of experiments[13–15] is the strongest evidence for physics beyond the SM measured in laboratories. The observation that neutrinos change their flavor while they propagate through space can only be explained, if at least two neutrinos have a non-zero mass. From the measurements and cosmological observations, we know that the masses are very small as compared to the lepton masses. Neither their existence, nor their smallness is not predicted by the SM, but adding additional RH neutrinos states to the theory could explain the origin of the observed non-zero neutrino masses and could be tested for by searching for corresponding signatures in experiments. But the addition of RH neutrino fields is not the only possible explanation for neutrino masses. Radiative neutrino mass mechanisms could also explain their origin and their smallness, but those would need the introduction of additional symmetries to the theory.

[13]: Davis et al. (1968), "Search for Neutrinos from the Sun"
[14]: Fukuda et al. (1998), "Evidence for Oscillation of Atmospheric Neutrinos"
[15]: Ahmad et al. (2002), "Direct Evidence for Neutrino Flavor Transformation from Neutral-Current Interactions in the Sudbury Neutrino Observatory"

cite neutrino oscillations/flavor conversions

Maybe also add this somehow: "From neutrino oscillation measurements the absolute mass scale cannot be determined, since they only depend on the mass differences, but there are upper limits on the sum of all neutrino masses from cosmological observations. These upper limits are typically between 0.3 and 1.3 eV [16]." "Actually 0.8 eV [17] from KATRIN and 1.2 eV [18, 19] from cosmological observations.

[16]: Tanabashi et al. (2018), "Review of Particle Physics"
[17]: Aker et al. (2022), "Direct neutrino-mass measurement with sub-electronvolt sensitivity"
[18]: Alam et al. (2021), "Completed SDSS-IV extended Baryon Oscillation Spectroscopic Survey: Cosmological implications from two decades of spectroscopic surveys at the Apache Point Observatory"
[19]: Aghanim et al. (2020), "Planck2018 results: VI. Cosmological parameters"

1.2.1 Mass Mechanisms

namedrop RH=sterile=HNL and why they are called like this based on the SM EW Lagrangian introduced above

There are no RH neutrinos in the SM and therefore the mass mechanism described in Section 1.1.3, which couples the Higgs field to LH and RH Weyl fields, predicts them to be massless. From experimental observations it is known that at least two of the three neutrino generations need to have a non-zero mass. Assuming the existence of RH neutrinos fields ν_R, one way of producing the neutrino masses is by adding a Yukawa coupling term

similar to the one for up-type quarks mentioned in Section 1.1.3, to write the full Yukawa Lagrangian as

$$\mathcal{L}_{\text{Yukawa}} = -Y^e_{ij}\bar{L}^i_L \Phi e^j_R - Y^\nu_{ij}\bar{L}^i_L \tilde{\Phi}\nu^j_R + h.c.\,, \tag{1.12}$$

with i, j running over the three generations of leptons e, μ, and τ, and Y^e and Y^ν being the Yukawa coupling matrices. Diagonalizing the Yukawa coupling matrices through unitary transformations U^e and U^ν leads to the **Dirac mass term** in the mass basis as

$$\mathcal{L}^{\text{mass}}_{\text{Dirac}} = \frac{v}{\sqrt{2}}\left(\bar{e}_L M_e e_R - \bar{\nu}_L M_\nu \nu_R\right)\,, \tag{1.13}$$

where M_e and M_ν are the diagonal mass matrices of leptons and neutrinos, respectively. A purely Dirac mass term would not explain the smallness of the neutrino masses in a straightforward way. Only fine-tuning the Yukawa coupling constants to small values would lead to small neutrino masses.

An additional way of generating neutrino masses is by adding a Majorana mass term of the form

$$\mathcal{L}_{\text{Majorana}} = -\frac{1}{2}M_{ij}(\nu^i_R)^c \nu^j_R + h.c.\,, \tag{1.14}$$

with M_{ij} being the Majorana mass matrix and the indices i, j running over all N_R RH neutrino generations. The superscript c denotes the charge conjugate field. Combining the charge conjugated RH neutrino fields with the LH neutrino fields as

$$\boldsymbol{N} = \begin{pmatrix} \boldsymbol{\nu}_L \\ \boldsymbol{\nu}^c_R \end{pmatrix}, \tag{1.15}$$

with $\boldsymbol{\nu}_R$ containing the N_R RH fields. The full neutrino mass Lagrangian is then given by the combined **Dirac and Majorana mass term** as

$$\mathcal{L}^{\text{mass},\nu}_{\text{Dirac+Majorana}} = \frac{1}{2}\boldsymbol{N}^T \hat{C} M^{\text{D+M}} \boldsymbol{N} + h.c.\,, \tag{1.16}$$

and the mass matrix is given by

$$M^{\text{D+M}} = \begin{pmatrix} 0 & (M^D)^T \\ M^D & M^R \end{pmatrix}. \tag{1.17}$$

On top of explaining the origin of neutrino masses itself, a combined Dirac and Majorana mass term could also solve the question of their smallness. If the mass of the RH neutrinos is very large, the masses of the active neutrino flavors is suppressed, which is known as *see-saw mechanism*.

1.2.2 Observational Avenues for Right-Handed Neutrinos

- oscillations searches for light steriles
- potential searches for heavy steriles

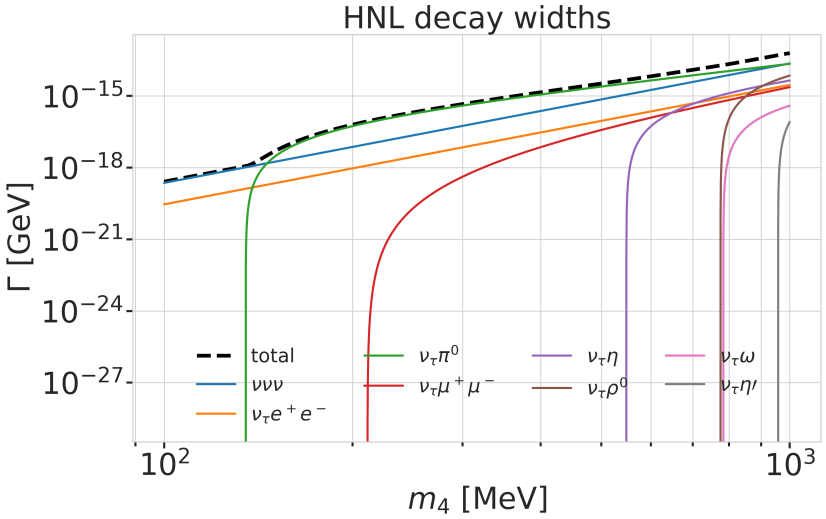

Figure 1.2: Decay widths of the HNL within the mass range considered, calculated based on the results from [20]. Given the existing constraints on $|U_{e4}|^2$ and $|U_{\mu 4}|^2$, we consider that the corresponding decay modes are negligible.

1.2.3 Searching for Heavy Neutral Leptons

Collider

Nuclear Decay

Extracted Beamlines

Atmospheric and Solar

Cosmological and Astrophysical

1.3 Atmospheric Neutrinos as Source of Heavy Neutral Leptons

write some interlude to motivate atm. neutrinos as source for HNL searches/production etc.

1.3.1 Production of Neutrinos in the Atmosphere

The analysis performed in this work is based on the sample of neutrinos observed in IceCube DeepCore at energies below 100 GeV. At these energies, the flux exclusively originates in the Earth's atmosphere. Highly relativistic cosmic rays (protons and heavier nuclei [16]) interact in the upper atmosphere, producing showers of secondary particles. Neutrinos are produced in decays of charged pions and kaons (π and K mesons) present in those showers, where the dominant contribution comes from the decay chain

$$\begin{aligned} \pi^\pm &\to \mu^\pm + \nu_\mu(\bar{\nu}_\mu) \,, \\ \mu^\pm &\to e^\pm + \bar{\nu}_\mu(\nu_\mu) + \nu_e(\bar{\nu}_e) \,, \end{aligned} \tag{1.18}$$

where muon neutrinos ν_μ and muons $\mu^\pm$ are produced in the first decay and both electron and muon neutrinos $\nu_{e/\mu}$ are produced in the second decay. Atmospheric muons, which are also produced in these decays, are the main background component for IceCube DeepCore analyses.

[16]: Tanabashi et al. (2018), "Review of Particle Physics"

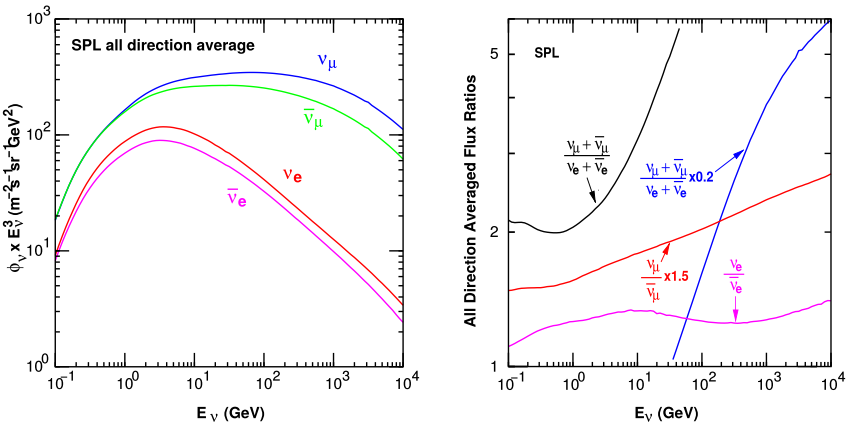

Figure 1.3: The atmospheric fluxes of different neutrino flavors as a function of energy (left) and the ratios between muon neutrinos and electron neutrinos as well as the ratios between neutrinos and antineutrinos for both those flavors (right). Results from the calculations performed for the geographic South Pole, taken from [21].

The different atmospheric flux components are shown in Figure 1.3 (left), for a much broader energy range than relevant for this work. Both neutrinos and antineutrino fluxes are shown for electron and muon neutrinos and all fluxes are the directionally averaged expectation calculated at the South Pole. Muon neutrinos are dominating the flux and from Equation 1.18 the naive assumption would be that the ratio between muon and electron neutrinos is $(\nu_\mu + \bar{\nu}_\mu)/(\nu_e + \bar{\nu}_e) = 2$. This is roughly true at energies below 1 GeV, where all muons decay in flight, but at larger energies muons can reach the detector before decaying, which increases the ratio to approximately 10:1 at around 100 GeV. Additionally, kaon decays start to contribute which also increases the number of muons and muon neutrinos. The increasing ratio can be seen in Figure 1.3 (right), which also shows the ration between neutrinos and antineutrinos for both flavors.

Charged mesons or tau particles can also be produced in cosmic ray interactions. Their decays lead to the production of tau neutrinos. At the energies relevant for this work however, the resulting tau neutrino flux is negligible as compared to the muon neutrino flux [22] and is not considered in the analysis. This is because both charged mesons and tau particles are much heavier than pions and kaons and therefore their production is suppressed at high energies.

[22]: Fedynitch et al. (2015), "Calculation of conventional and prompt lepton fluxes at very high energy"

Say something about atmospheric neutrino flux uncertainties, based on recent JP/Anatoli papers.

1.3.2 Interactions with Nuclei

The neutrino detection principle of IceCube DeepCore is explained in Chapter 2 and relies on the weak interaction processes between neutrinos and the nuclei of the Antarctic glacial ice. At neutrino energies above 5 GeV, the cross-sections are dominated by ***deep inelastic scattering (DIS)***, where the neutrino is energetic enough to resolve the underlying structure of the nucleons and interact with one of the composing quarks individually. As a result the nucleon breaks and a shower of hadronic secondary particles is produced. Depending on the type of interaction, the neutrino either remains in the final state for NC interactions or is converted into its charged lepton counterpart for CC interactions. The CC DIS interactions have the form

$$\begin{aligned} \nu_l + N &\rightarrow l^- + X \,, \\ \bar{\nu}_l + N &\rightarrow l^+ + X \,, \end{aligned} \tag{1.19}$$

where $\nu_l/\bar{\nu}_l$ and l^-/l^+ are the neutrino/antineutrino and its corresponding lepton/antilepton, and l can be either an electron, muon, or tau. N is the nucleon and X stands for any set of final state hadrons. The NC DIS interactions are

$$\begin{aligned} \nu_l + N &\rightarrow \nu_l + X \text{ and} \\ \bar{\nu}_l + N &\rightarrow \bar{\nu}_l + X \,. \end{aligned} \tag{1.20}$$

Figure 1.4 shows the Feynman diagrams for both processes DIS interactions

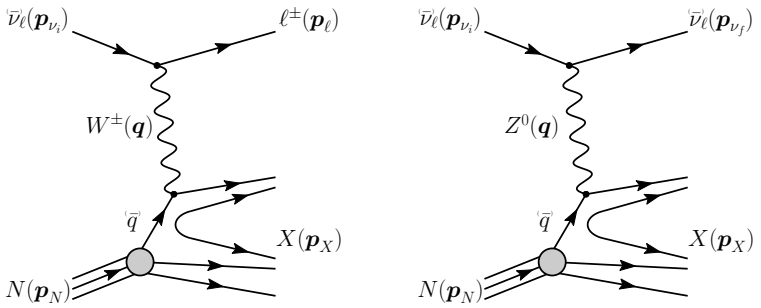

Figure 1.4: Feynman diagrams for deep inelastic scattering of a neutrino with a nucleon via charged-current (left) and neutral current (right) interactions. $\boldsymbol{p}_{\nu_i}$, $\boldsymbol{p}_N$ and $\boldsymbol{p}_{\nu_f}$, $\boldsymbol{p}_l$, $\boldsymbol{p}_N$ are the input and output four-momenta, while $\boldsymbol{q}$ is the momentum transfer. Taken from [11].

have a roughly linear energy dependent cross-section above ~20 GeV and are well measured and easy to theoretically calculate. They are the primary interaction channel for neutrinos detected with IceCube.

At energies below 5 GeV, ***quasi-elastic scattering (QE)*** and ***resonant scattering (RES)*** become important. At these energies the neutrinos interact with the approximately point-like nucleons, without breaking them up in the process. RES describes the process of a neutrino scattering off a nucleon producing an excited state of the nucleon in addition to a charged lepton. It is the dominant process at 1.5 GeV to 5 GeV for neutrinos and 1.5 GeV to 8 GeV for antineutrinos. Below 1.5 GeV QE is the main process, where protons are converted to neutrons in antineutrino interactions and vice-versa for neutrino interactions. Additionally, a charged lepton corresponding to the neutrino/antineutrino flavor is produced. The cross-sections of QE and RES scattering processes are not linear in energy and the transition region from QE/RES to DIS is poorly understood. The total cross-sections and their composition is shown in Figure 1.5. It can be seen that the interaction cross-sections are very small at the order of 10^{-38} cm^2. This is the reason why very large volume detectors are required to measure atmospheric neutrinos with sufficient statistics to perform precision measurements of their properties. The interaction length of a neutrino with $E_\nu = 10$ GeV is of $\mathcal{O}(10 \times 10^{10}$ km), for example.

1.3.3 Oscillations

So far we have described neutrinos in their flavor eigenstates, which are relevant for weak interactions. In the SM three-neutrino model the weak flavor states are ν_e, ν_μ, and ν_τ, which relate them to the charged leptons they interact with in CC interactions. There is a second way of describing neutrino wave functions based on their Hamiltonian eigenvalues [24], namely as the mass eigenstates ν_1, ν_2, and ν_3. These states are related to the flavor eigenstates by the unitary, 3x3 *Pontecorvo-Maki-Nakagawa-Sakata (PMNS)*

[24]: Bilenky et al. (1978), "Lepton mixing and neutrino oscillations"

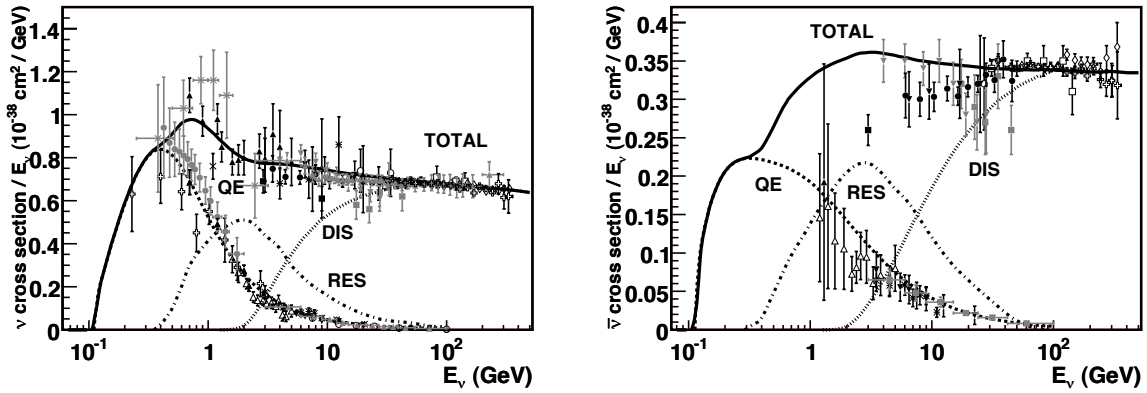

Figure 1.5: Total neutrino (left) and antineutrino (right) per nucleon cross-section divided by neutrino energy plotted against energy. The three main scattering processes quasi-elastic scattering (QE), resonant scattering (RES), and deep-inelastic scattering (DIS) are shown. Taken from [23].

matrix U, where the flavor states are a superposition of the mass states as

$$|\nu_\alpha\rangle = \sum_k U^*_{\alpha k} |\nu_k\rangle \ , \tag{1.21}$$

with the weak flavor states $|\nu_\alpha\rangle$, $\alpha = e, \mu, \tau$, and the mass states $|\nu_k\rangle$ with $k = 1, 2, 3$. The mixing matrix can be parameterized as [16]

[16]: Tanabashi et al. (2018), "Review of Particle Physics"

$$U = \begin{pmatrix} 1 & 0 & 0 \\ 0 & c_{23} & s_{23} \\ 0 & -s_{23} & c_{23} \end{pmatrix} \begin{pmatrix} c_{13} & 0 & s_{13}e^{-i\delta_{CP}} \\ 0 & 1 & 0 \\ -s_{13}e^{i\delta_{CP}} & 0 & c_{13} \end{pmatrix} \begin{pmatrix} c_{12} & s_{12} & 0 \\ -s_{12} & c_{12} & 0 \\ 0 & 0 & 1 \end{pmatrix} , \tag{1.22}$$

where $c_{ij} = \cos\theta_{ij}$ and $s_{ij} = \sin\theta_{ij}$ are cosine and sine of the mixing angle θ_{ij}, that defines the strength of the mixing between the mass eigenstates i and j, and δ_{CP} is the neutrino CP-violating phase.

add current BF values from nufit or so?

Describing neutrinos in their mass state is crucial to understand their propagation through space and time. Their propagation in vacuum can be expressed by applying a plane wave approach, where the mass eigenstates evolve as

$$|\nu_k(t)\rangle = e^{-iE_k t/\hbar} |\nu_k\rangle \ . \tag{1.23}$$

The energy of the mass eigenstate $|\nu_k\rangle$ is $E_k = \sqrt{\vec{p}^2c^2 + m_k^2c^4}$, with momentum $\vec{p}$ and mass m_k, $\hbar$ is the reduced Planck constant, and c is the speed of light in vacuum. The existence of non-zero, non-equal masses and the neutrino mixing relation in Equation 1.21, lead to the observed phenomenon of neutrino oscillations. Oscillations mean that a neutrino changes from its initial flavor, that it was produced with, to another flavor and back after traveling a certain distance. A neutrino is produced as a flavor eigenstate $|\nu_\alpha\rangle$ in a CC weak interaction, but its propagation happens as the individual mass states it is composed of. The probability of finding the neutrino with initial flavor $|\nu_\alpha\rangle$ in the flavor state $|\nu_\beta\rangle$ after the time t is calculated as

$$P_{\nu_\alpha \to \nu_\beta}(t) = |\left\langle \nu_\beta | \nu_\alpha(t) \right| \left. \nu_\beta | \nu_\alpha(t) \right\rangle|^2 \ , \tag{1.24}$$

by applying Fermi's Golden Rule [25], which defines the transition rate from one eigenstate to another by the strength of the coupling between them. This coupling strength is the square of the matrix element and using the fact that the mixing matrix is unitary ($U^{-1} = U^\dagger$) to describe the mass eigenstates

[25]: Dirac (1927), "The Quantum Theory of the Emission and Absorption of Radiation"

as flavor eigenstates, we find the time evolution of the flavor state $|\nu_\alpha(t)\rangle$, which can be inserted into Equation 1.24 to find the probability as

$$P_{\nu_\alpha \to \nu_\beta}(t) = \sum_{j,k} U^*_{\beta j} U_{\alpha j} U_{\beta k} U^*_{\alpha k} e^{-i(E_k - E_j)t/\hbar} \,. \tag{1.25}$$

The indices j and k run over the mass eigenstates. We can approximate the energy as

$$E_k \approx E + \frac{c^4 m_k^2}{2E} \quad \longrightarrow \quad E_k - E_j \approx \frac{c^4 \Delta m^2_{kj}}{2E} \,, \tag{1.26}$$

for small neutrino masses compared to their kinetic energy. Here, $\Delta m^2_{kj} = m^2_k - m^2_j$ is the mass-squared splitting between states k and j. Replacing the time in Equation 1.25 by the distance traveled by relativistic neutrinos $t \approx L/c$ we get

$$\begin{aligned} P_{\nu_\alpha \to \nu_\beta}(t) = \delta_{\alpha\beta} - 4 \sum_{j>k} \mathbf{Re}(U^*_{\beta j} U_{\alpha j} U_{\beta k} U^*_{\alpha k}) \sin^2\left(\frac{c^3 \Delta m^2_{kj}}{4E\hbar} L\right) \\ +2 \sum_{j>k} \mathbf{Im}(U^*_{\beta j} U_{\alpha j} U_{\beta k} U^*_{\alpha k}) \sin^2\left(\frac{c^3 \Delta m^2_{kj}}{4E\hbar} L\right) \,, \end{aligned} \tag{1.27}$$

which is called the survival probability if $\alpha = \beta$, and the transition probability if $\alpha \neq \beta$. Once again, this probability is only non-zero if there are neutrino mass eigenstates with masses greater than zero. Additionally, there must be a mass-squared difference Δm^2 and non-zero mixing between the states. Since we assumed propagation in vacuum in Equation 1.23, the transition and survival probabilities correspond to vacuum mixing.

say something about how this changes with matter

1.3.4 Testing Heavy Neutral Leptons with Atmospheric Neutrinos

Re-write/re-formulate this section (copied from HNL technote).

The Minimal Standard Model Extension

Extensions to the Standard Model (SM) that add *Heavy Neutral Leptons (HNLs)* provide a good explanation for the origin of neutrino masses through different seesaw mechanisms [26]. While the mixing with $\nu_{e/\mu}$ is strongly constrained ($|U^2_{\alpha 4}| \lesssim 10^{-5} - 10^{-8}, \alpha = e, \mu$), the mixing with ν_τ is much harder to probe due to the difficulty of producing and detecting ν_τ. Figure 1.6 shows the current limits on the τ-sterile mixing space for HNL masses between 0.1 GeV-10 GeV. As was first pointed out in [32], the atmospheric neutrino flux observed in IceCube offers a way to constrain the neutrino-HNL mixing parameters. By using the large fraction of atmospheric ν_μ events that oscillate into ν_τ before they reach the detector, the less constrained τ-sterile mixing space can be explored. In this document, we present the methodology and strategy of a search for HNLs with IceCube DeepCore. These additional RH neutrinos can be included in the Standard Model (SM) by extending the PMNS matrix to at least a 3x4 matrix as

[26]: Yanagida (1980), "Horizontal Symmetry and Masses of Neutrinos"

Produce similar styled plot for these limits

[32]: Coloma et al. (2017), "Double-Cascade Events from New Physics in Icecube"

$$\begin{pmatrix} \nu_e \\ \nu_\mu \\ \nu_\tau \\ \nu_s \end{pmatrix} = \begin{pmatrix} U_{e1} & U_{e2} & U_{e3} & U_{e4} \\ U_{\mu 1} & U_{\mu 2} & U_{\mu 3} & U_{\mu 4} \\ U_{\tau 1} & U_{\tau 2} & U_{\tau 3} & U_{\tau 4} \\ U_{s1} & U_{s2} & U_{s3} & U_{s4} \end{pmatrix} \begin{pmatrix} \nu_1 \\ \nu_2 \\ \nu_3 \\ \nu_4 \end{pmatrix} \,, \tag{1.28}$$

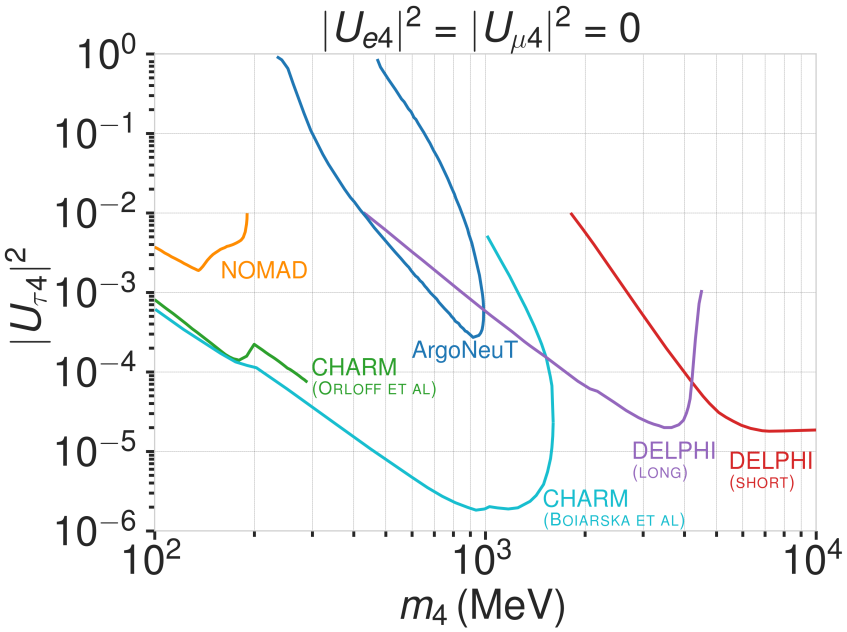

Figure 1.6: Current $|U^2_{\tau 4}| - m_4$ limits from NOMAD [27], ArgoNeut [28], CHARM [29, 30], and DELPHI [31].

where the components with index 4 define the mixing between the flavor states and the fourth sterile mass state, respectively. Note here that this is not a theoretically fully consistent picture, but rather the phenomenologically minimal model to be tested by this analysis. This can hopefully be put into the larger context of several fully consistent models, later. Due to the singlet nature of the RH neutrinos, they only interact weakly, inheriting these interactions from their LH neutrino counterparts via mixing. This mixing of the HNLs with the electron, muon, and tau neutrinos can be probed and constrained as a function of the HNL mass by searching for their production and decay. In [32, 33] this search is mainly motivated through two experimental arguments. Secondly, IceCube is ideally placed to explore the yet unconstrained $|U_{\tau 4}|^2 - m_4$ phase-space that is not easily accessible by accelerator-based experiments.

[32]: Coloma et al. (2017), "Double-Cascade Events from New Physics in Icecube"
[33]: Coloma (2019), "Icecube/DeepCore tests for novel explanations of the MiniBooNE anomaly"

This section really needs to be re-written to motivate the search for HNLs from a more generic point of view (e.g. to explain neutrino masses)

In order to probe the τ-sterile mixing parameter, it is required to look at interactions involving τ neutrinos. However, most neutrinos produced in cosmic ray interactions with the atmosphere are ν_e or ν_μ. Therefore, we need these neutrinos to oscillate to the τ flavor before reaching the detector. For this to happen at the considered energies a traveled distance of the order of the earth diameter is necessary. This is why our signal is mostly up-going and passing through the whole earth.

This section definitley needs to be elaborated in a little more detail

To explain the signature we can observe in IceCube we first have to revisit the weak interactions that the HNL inherits from its LH counterpart through mixing. We will be following the derivation in [20]. Extending the SM by n additional RH neutrinos, ν_i $(i = 3 + n)$, leads to the mass Lagrangian

[20]: Coloma et al. (2021), "GeV-scale neutrinos: interactions with mesons and DUNE sensitivity"

$$\mathscr{L}_\nu^{mass} \supset -\sum_{\alpha=e,\mu,\tau}\sum_{i=4}^{3+n} Y_{\nu,\alpha i}\bar{L}_{L,\alpha}\tilde{\phi}\nu_i - \frac{1}{2}\sum_{i=4}^{3+n} M_i\bar{\nu}_i\nu_i^c + h.c., \tag{1.29}$$

in a basis where the Majorana mass terms are diagonal. $Y_{\nu,\alpha i}$ are the Yukawa couplings to the lepton doublets and M the Majorana masses for the heavy singlets. $L_{L,\alpha}$ stands for the SM LH lepton doublet of flavor α while ϕ is the Higgs field, and $\tilde{\phi} = i\sigma_2\phi^*$ and $\nu_i^c \equiv C\bar{\nu}_i^t$, with $C = i\gamma_0\gamma_2$ in the

Not adding information about the case where the neutrinos have Dirac or pseudo-Dirac masses

Weyl representation. The full neutrino mass matrix with the Higgs vacuum expectation value $v/\sqrt{2}$ reads

$$\mathcal{M} = \begin{pmatrix} 0_{3\times3} & Y_\nu v/\sqrt{2} \\ Y_\nu^t v/\sqrt{2} & M \end{pmatrix}, \tag{1.30}$$

and can be diagonalized by a $(3+n)$ x $(3+n)$ full unitary roation U, that itself leads to neutrino masses upon diagonalization, additionally manifesting the mixing between active neutrinos and heavy states. The resulting model consists of 3 light SM neutrino mass eigenstates ν_i $(i = 1, 2, 3)$ and n heavier states, as introduced above. The flavor states will now consist of a combination of light and heavy states

$$\nu_\alpha = \sum_{i=1}^{3+n} U_{\alpha i}\nu_i, \tag{1.31}$$

and the leptonic part of the EW Lagrangian can be written as

$$\mathscr{L}_{\text{EW}}^{\ell} = \frac{g}{\sqrt{2}} W_\mu^+ \sum_\alpha \sum_i U_{\alpha i}^* \bar{\nu}_i \gamma^\mu P_L \ell_\alpha + \frac{g}{4c_w} Z_\mu \times \left\{ \sum_{i,j} C_{ij} \bar{\nu}_i \gamma^\mu P_L \nu_j + \sum_\alpha \bar{\ell}_\alpha \gamma^\mu \left[2s_w^2 P_R - (1-2s_w^2) P_L \right] \ell_\alpha \right\} + h.c.,$$

where $c_w \equiv \cos\theta_w$, $s_w \equiv \sin\theta_w$, and θ_w the SM weak mixing angle. P_L and P_R are the left and right projectors, respectively, while

$$C_{ij} \equiv \sum_\alpha U_{\alpha i}^* U_{\alpha j}. \tag{1.32}$$

The indices now sum over all $(3 + n)$ flavor and mass states.

Based on this formulation and assuming that only the mixing with the tau sector is open ($|U_{\alpha 4}^2| = 0, \alpha = e, \mu$), the relevant production diagram of the HNL can be drawn as shown in Figure 1.7. Alongside the fourth heavy mass state, a Hadronic cascade is produced. The heavy mass state will travel for some distance (dependent on mass and mixing) before it decays. The subsequent decay processes are depicted in Figure 1.8. It can be a CC or NC decay and both leptonic and mesonic modes are possible (dependent on the mass). This will produce a tau or a tau neutrino and another cascade that can be EM or Hadronic. The branching ratios corresponding to the decay modes of the HNL for the mass range of interest (i.e. between 100 MeV and 1 GeV) are shown in Figure 1.9a as a function of the HNL mass.

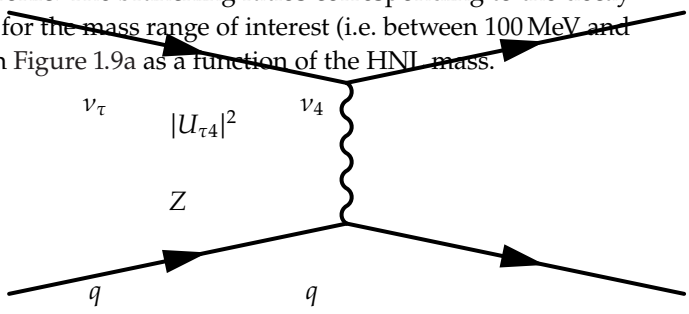

Figure 1.7: Production of a sterile neutrino in the up-scattering of a tau neutrino.

Production and Decay in IceCube DeepCore

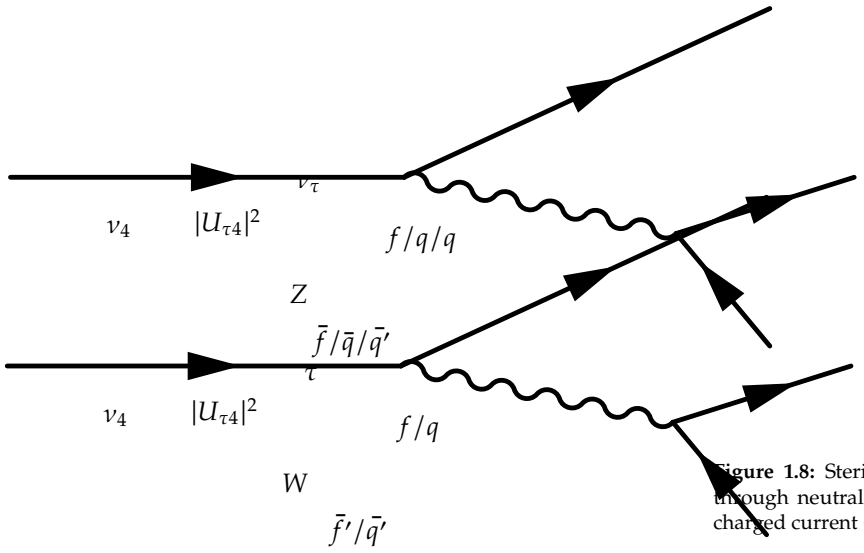

Figure 1.8: Sterile neutrino decay through neutral current (left) and charged current (right).

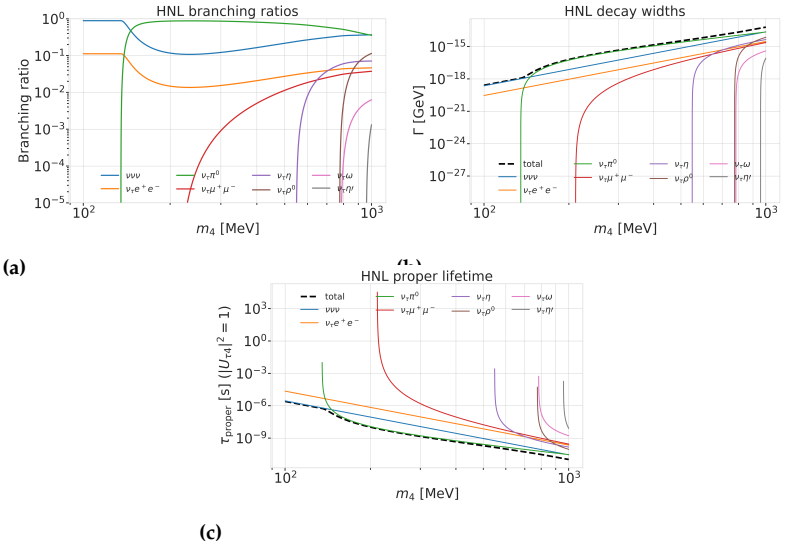

(a) **(b)** **(c)**

Figure 1.9: Branching ratios, decay widths, and proper lifetime of the HNL within the mass range considered, calculated based on the results from [20].

The IceCube Neutrino Observatory

2

add fancy icecube header picture here

The IceCube Neutrino Observatory [34] is a cubic-kilometer, ice-Cherenkov detector located at the geographic South Pole. IceCube utilizes the Antarctic glacial ice as detector medium to observe neutrinos by measuring the Cherenkov light produced from secondary charged particles. It was deployed between 2006 and 2011 and has been taking data since the installation of the first modules. The primary goal of IceCube is the observation of astrophysical neutrinos as a telescope, but it can also be used to study fundamental particle physics properties by measuring atmospheric neutrinos as well as studying cosmic rays.

This chapter first describes the main- and sub-array of the detector and its detection module in Section 2.1, the propagation of particles through ice is explained in Section 2.2, and finally, the signatures that IceCube can observe of the different particles are introduced in Section 2.3.

[34]: Aartsen et al. (2017), "The IceCube Neutrino Observatory: instrumentation and online systems"

2.1 Detector Components

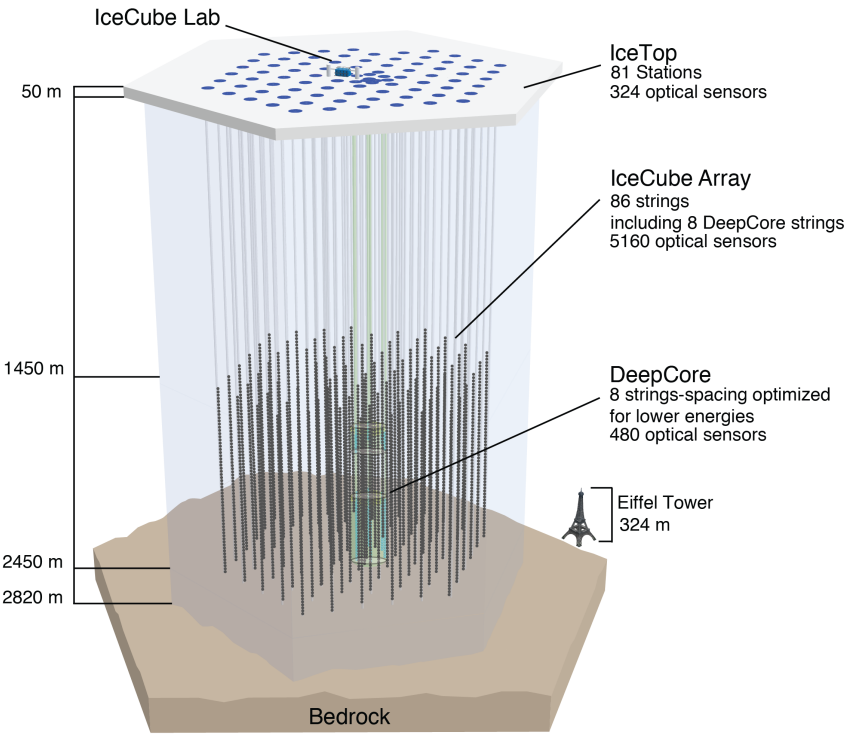

Figure 2.1: Overview of the IceCube detector showing the in-ice main- and sub-array IceCube and DeepCore, IceTop, and the IceCube Laboratory. From [34].

The full IceCube detector array consists of 86 vertical, in-ice strings and 81 surface stations as shown in Figure 2.1. The in-ice part is composed of 60 optical modules per string deployed at depths of 1450 m-2450 m below the ice, while the surface stations of the cosmic air-shower array, *IceTop*, are ice-filled tanks. The surface stations and the majority of the strings are arranged in a hexagonal grid with the operations building, the *IceCube Laboratory* (ICL), central to the grid on the surface. A top view of the hexagonal arrangement

is shown in Figure 2.4. The in-ice array is designed to detect neutrinos in the energy range from GeV to PeV.

2.1.1 Digital Optical Modules and the Antarctic Ice

The IceCube detection medium is the Antarctic glacial ice itself, which was formed over 100 000 years by accumulation of snow that was subsequently compressed by its own weight to form a dense crystal structure [35]. As a result of this formation process, the optical properties, scattering and absorption, primarily change with depth. Within the detector volume the absorption length ranges from 100 m-400 m, while the scattering length lies between 20 m and 100 m. They are correlated, with the absorption length being roughly four times the scattering length [36]. The vertical distribution of scattering and absorption length can be seen in Figure 2.2, where one dominant feature is the *dust layer* between 2000 m and 2100 m depth. This region has a higher concentration of dust particles that were deposited in a period of high volcanic activity, which leads to bad optical properties in form of larger scattering and absorption.

[35]: Price et al. (2000), "Age vs depth of glacial ice at South Pole"

SB: there are more properties than just these. Somehow need a half sentence that explains why these are particularly important to single out (see ice papers for inspiration)

CL: maybe define that absorption and scattering lengths are? they are defined differently so this invites a comparison that is not so obvious

[36]: Abbasi et al. (2022), "In-situ estimation of ice crystal properties at the South Pole using LED calibration data from the IceCube Neutrino Observatory"

Add reference for the dust layer!

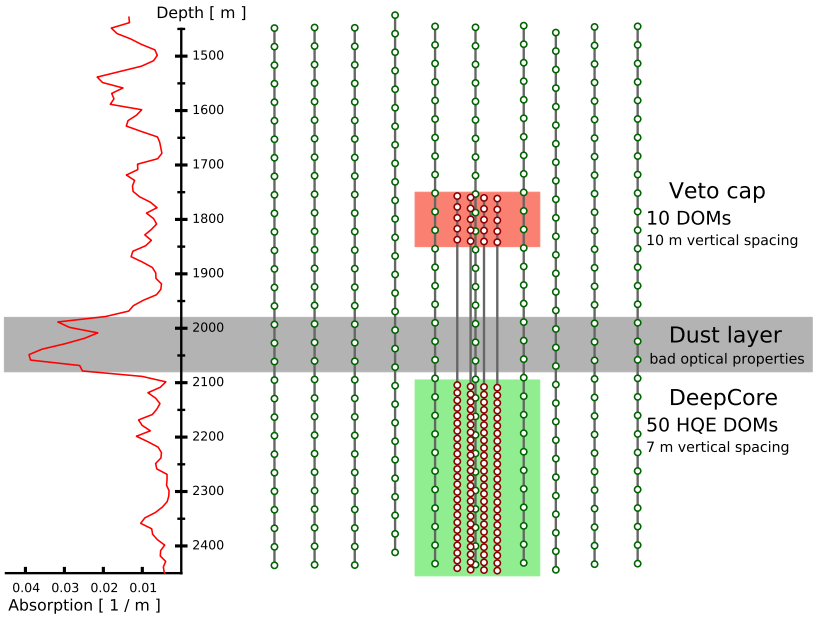

Figure 2.2: Side view of IceCube and DeepCore showing the depth dependent scattering and absorption length (left panel) and the DOM positions around the dust layer.

exchange for figure with scattering (check abs/sca is correct)

mention/cite dust logger paper/procedure?

[37]: Abbasi et al. (2009), "The IceCube data acquisition system: Signal capture, digitization, and timestamping"

The ice is instrumented by 5160 optical sensors called *Digital Optical Modules* (DOMs) [37], which can detect the Cherenkov light produced by charged particles traveling through the ice. Each DOM is made of a spherical glass housing, containing a downward-facing Photomultiplier Tube (PMT), the main-board with control, readout, and processing-electronics, and a LED flasher-board for calibration purposes. The design and the individual components of a DOM can be seen in Figure 2.3.

The majority of PMTs are the 10 " Hamamatsu R7081-02, which have a bialkali photocathode and are sensitive to wavelengths in the range of 300 nm to 650 nm, with a peak quantum efficiency of 25% at 390 nm. In the central part of the IceCube array the peak efficiency reaches 34%. The dark count rate in the temperature range of −40 °C to −20 °C is ~300 Hz. The DOM electronics measure the PMT voltage and control the gain. At a voltage crossing of the equivalent to 0.25 PE the waveform readout is activated [37]. Only when

[37]: Abbasi et al. (2009), "The IceCube data acquisition system: Signal capture, digitization, and timestamping"

either one of the nearest or next to nearest DOMs above or below also sees a voltage crossing within a 1 µs time window [1], the voltages are digitized and sent to the ICL. Through the application of a waveform unfolding algorithm, called *WaveDeform* [38], the waveforms are compressed, and the results are the reconstructed times and charges of the photo-electrons. This is the basis for all further IceCube data processing.

The PMT is covered with a mu-metal grid (made from wire mesh), shielding the photocathode from Earth's magnetic field, and it is optically coupled to the glass sphere by RTV silicone gel. The glass sphere is a pressure vessel, designed to withstand both the constant ice pressure and the temporary pressure during the refreezing process of the water in the drill hole during deployment (peaking at around 690 bar). The sphere is held by a harness that connects the DOMs along a string and also guides the cable beside them.

The flasher-board controls 12 LEDs that produce optical pulses with a wavelength of 405 nm [34]. The LEDs can be pulsed separately or in combination with variable output levels and pulse lengths. Using the known information of the light source positions and times this can be used for in-situ calibration of the detector by measuring absorption and scattering properties of the ice. Calibrating the absolute efficiency of the DOMs itself is more accurately done using minimum ionizing muons [39, 40], since the total amplitude of the LED light is not well known.

1: This is referred to as a *hard local coincidence (HLC)* [37].

[38]: Aartsen et al. (2014), "Energy Reconstruction Methods in the IceCube Neutrino Telescope"

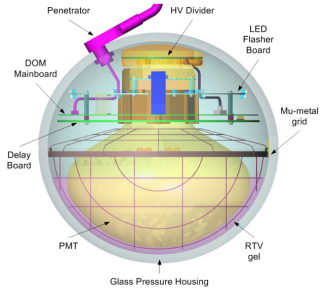

Figure 2.3: Design and components of a Digital Optical Module (DOM) [37]

[34]: Aartsen et al. (2017), "The IceCube Neutrino Observatory: instrumentation and online systems"

[39]: Feintzeig (2014), "Searches for Point-like Sources of Astrophysical Neutrinos with the IceCube Neutrino Observatory"

[40]: Kulacz (2019), "In Situ Measurement of the IceCube DOM Efficiency Factor Using Atmospheric Minimum Ionizing Muons"

Add accuracy of the efficiency calibration here.

2.1.2 IceCube

The 78 strings that are arranged in a hexagonal pattern from the main part of the in-ice array, which is called *IceCube*. With a ~125 m horizontal spacing between the strings and a ~17 m vertical spacing between DOMs, IceCube has a lower energy threshold of around 100 GeV. IceCube was designed to detect astrophysical neutrinos with energies above 1 TeV.

The coordinate system that is used in IceCube is centered at 46500'E, 52200'N at an elevation of 883.9 m [34]. Per definition, it's a right-handed coordinate system where the y-axis points along the Prime Meridian (Grid North) towards Greenwich, UK, and the x-axis points 90° clockwise from the y-axis (Grid East). The z-axis is normal to the ice surface, pointing upwards. For IceCube analyses depth is defined as the distance along the z axis from the ice surface, assumed to be at an elevation of 2832 m.

[34]: Aartsen et al. (2017), "The IceCube Neutrino Observatory: instrumentation and online systems"

Maybe throw the coordinate system in a box on the side?

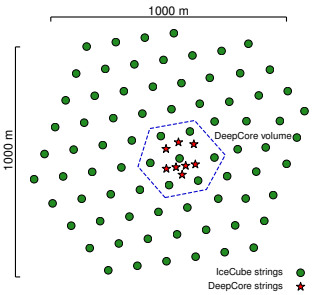

Figure 2.4: Top view of the IceCube array.

Blow up this image a bit, so it's better readable as marginfigure.

2.1.3 DeepCore

The additional 8 strings form a denser sub-array of IceCube called *DeepCore* [41]. It's located at the bottom-center of the in-ice array and its *fiducial volume* also includes the 7 surrounding IceCube strings as shown in Figure 2.4. The strings in this region have a closer average horizontal distance of about 70 m. The lower 50 DeepCore DOMs on each string are placed in the region of clear ice below the dust layer between 2100 m to 2450 m depth, where their vertical spacing is ~7 m. The remaining 10 modules on each string are placed above the dust layer to be used as veto against atmospheric muons as can be seen in Figure 2.2. Additionally, the DeepCore DOMs are equipped with higher quantum efficiency PMTs. The combination of the denser spacing, the high

[41]: Abbasi et al. (2012), "The design and performance of IceCube DeepCore"

CL: value?

quantum efficiency modules, and the most favorable ice properties below the dust layer leads to a lower energy detection threshold of around 5 GeV, allowing the more efficient observation of atmospheric neutrinos, which are mostly in the energy range of 10 GeV-100 GeV. The main analysis performed with DeepCore is an atmospheric neutrino oscillation measurement, but the large flux of atmospheric neutrinos allows for many other Beyond Standard Model searches, such as searches for dark matter, non-standard interactions, or sterile neutrinos.

SB: this needs revision. the energy range you mention is particular for oscillations already (atmopsheric neutrinos are plentiful outside of this range you mentioned). If you rewrite the first part you'll have to revisit the second part. Also in general I'd suggest not to rank analyses like Main and Other - DeepCore was orginally intended as a dark matter detector, and there are probably more DM analyses unblinded / year than oscillations. Just keep it general, no need to rank.

2.2 Particle Propagation in Ice

Neutrinos interacting in the ice via DIS produce muons, electromagnetic showers, and hadronic showers, depending on their flavor and the interaction type. The particles produced in those processes mainly lose their energy through *ionization*, *bremsstrahlung*, *pair production*, and the *photo-nuclear interaction*. Electrically charged particles also emit Cherenkov light when traveling through the ice, which is the main observable in IceCube, but only contributes a small amount to the total energy loss. The Cherenkov effect and the energy losses of the particles are described in the following sections, followed by an overview of the different particle signatures in IceCube.

2.2.1 Cherenkov Effect

When a charged particle moves through a medium with a velocity that is greater than the speed of light in that medium, it emits Cherenkov radiation, losing a very small amount of energy ($\mathcal{O}(10^{-4})$ of the total energy loss). The detection principle of IceCube DeepCore, is based on the observation of resulting Cherenkov photons that are emitted by the charged secondary particles produced in the neutrino interactions that were introduced in Section **??**. The Cherenkov effect was first observed by Pavel Cherenkov in 1934 [42] and occurs when the charged particle travels faster than the phase velocity of light, therefore polarizing the medium. Upon de-excitation the molecules emit the received energy as photons in a spherical wavefront. Since the particle moves past this wavefront, the superposition of the spherical light emissions forms a cone, which is shown in blue in the bottom panel of Figure 2.5.

[42]: Cherenkov (1937), "Visible Radiation Produced by Electrons Moving in a Medium with Velocities Exceeding that of Light"

Using trigonometry, the angle θ_c at which the Cherenkov light is emitted can be calculated as

$$\theta_c = \arccos\left(\frac{1}{\beta n}\right), \tag{2.1}$$

where β is the velocity of the particle in units of the speed of light and n is the refractive index of the medium. When the particle velocity is close to the speed of light, the equation holds and the angle is only dependent on the refractive index of the medium. For the Antarctic ice, the refractive index is $n \approx 1.3$ and as a result $\theta_c \approx 41°$.

The frequency of the emission depends on the charge z and the wavelength-dependent index of refraction $n(\omega)$ and is given by the Frank-Tamm formula [43, 44]

$$\frac{d^2N}{dxd\lambda} = \frac{2\pi\alpha z^2}{\lambda^2}\left(1 - \frac{1}{\beta^2 n(\omega)^2}\right), \tag{2.2}$$

with $\alpha \approx 1/137$ the fine structure constant, λ the wavelength of the emitted light, and x the path length traversed by the particle. Relativistic particles in ice produce roughly 250 photons per cm in the wavelength range of 300 nm-500 nm [45].

2.2.2 Energy Losses

Even though relativistic, charged particles traveling through matter produce Cherenkov radiation, their energy is mainly lost through other processes that are dependent on the particle type and energy. The exact principles of energy loss for the different types can broadly be categorized into the three groups: quasi-continuous energy loss by muons, electromagnetic cascades, and hadronic cascades.

Muons

Muons lose their energy by ionization, bremsstrahlung, pair production, and the photo-nuclear effect. The energy loss by ionization is the dominant process for muons above 1 GeV and has a weak energy dependence given by

$$\left\langle -\frac{\mathrm{d}E}{\mathrm{d}x} \right\rangle = a_I(E) + b_R(E) \cdot E \ , \tag{2.3}$$

where E is the energy and $a_I(E)$ and $b_R(E) \cdot E$ are the energy loss by ionization and the combined radiative losses, respectively. In the energy range relevant for this work (10 GeV-100 GeV), the parameters a_I and b_R only depend on energy very weakly and can be approximated by constants. The energy loss is then given by

$$\left\langle -\frac{\mathrm{d}E}{\mathrm{d}x} \right\rangle = a + b \cdot E \ . \tag{2.4}$$

Based on this description, there is a critical energy which divides the regimes where ionization and radiative losses dominate. The critical energy is given by $E_{\mathrm{crit}} = a/b$ and for muons in ice it is ~713 GeV (using $a \approx 2.59\,\mathrm{MeVcm}^{-1}$ and $b \approx 3.63 \times 10^{-6}\,\mathrm{cm}^{-1}$ [46]). Since the energy range of interest is well below this critical energy, the range of a muon can easily be related to its energy by

$$\langle L \rangle = \frac{E_0}{a} \ . \tag{2.5}$$

Measuring the length of a muon track therefore allows for an estimation of its energy if the full track is contained within the instrumented volume of IceCube. Using the given numbers a 30 GeV muon travels ~116 m. This approximate treatment does not take into account the stochastic nature of some energy losses. Bremsstrahlung and photo-nuclear interactions for example rarely occur, but when they do, they deposit a large chunk of energy. A thorough investigation of the energy losses of muons in ice can be found in [47].

Electromagnetic Showers

Photons as well as electrons and positrons are produced either directly in neutrino interactions or in secondary particle interactions. Above a critical energy E_c, they lose their energy through repeated pair production and

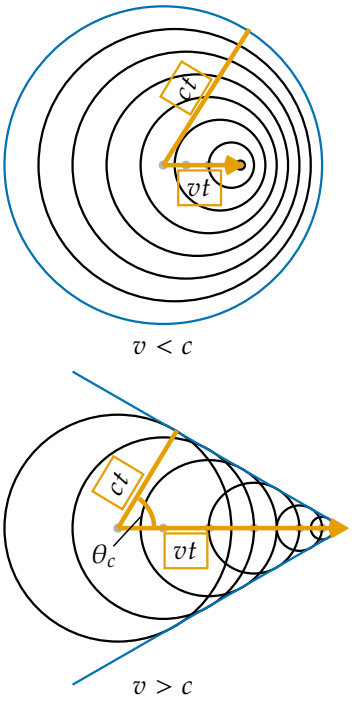

Figure 2.5: Schematic depiction of the spherical light front produced by a particle traveling slower than the speed of light in the medium (top) and the formation of the Cherenkov light front produced by a charged particle traveling faster than the speed of light in the medium (bottom). Blue is the resulting wavefront, while the black circles are spherically emitted light at each position and the orange arrows show the direction of the particle.

Cite n and θ_c

[43]: Frank et al. (1937), "Coherent visible radiation from fast electrons passing through matter"
[44]: Tamm (1991), "Radiation Emitted by Uniformly Moving Electrons"
[45]: Rädel et al. (2012), "Calculation of the Cherenkov light yield from low energetic secondary particles accompanying high-energy muons in ice and water with Geant4 simulations"

SB: you already mentioned that Cher. Rad. doesn't lead to signfiicant energy loss. I suggest to clean up the text a bit, you dont' need to emphasize that so many times. Pick one place (probably here) and eliminate it elsewhere

Add reference (PDG or find original)

[46]: Chirkin et al. (2004), "Propagating leptons through matter with Muon Monte Carlo (MMC)"

SB: i like that you give a benchmark value here, for rule of thumb or so, but it should be related to the detector geometry somehow or else it feels too out of place. Give it some context

[47]: Raedel (2012), "Simulation Studies of the Cherenkov Light Yield from Relativistic Particles in High-Energy Neutrino Telescopes with Geant4"

Add reference for these processes.

[16]: Tanabashi et al. (2018), "Review of Particle Physics"

cite em shower distribution

[47]: Raedel (2012), "Simulation Studies of the Cherenkov Light Yield from Relativistic Particles in High-Energy Neutrino Telescopes with Geant4"

[48]: Agostinelli et al. (2003), "Geant4—a simulation toolkit"

Add angular profile plot (Summer agrees!) (create one based on Leif Rädel as Alex did)

SB: rephrase gamma (from equation) is not defined

[47]: Raedel (2012), "Simulation Studies of the Cherenkov Light Yield from Relativistic Particles in High-Energy Neutrino Telescopes with Geant4"

[49]: Gabriel et al. (1994), "Energy dependence of hadronic activity"

bremsstrahlung emission forming an expanding, electromagnetic shower profile. The particles' energy reduces with every interaction and their number increases until they fall below the critical energy where ionization and excitation of surrounding atoms become the dominant energy loss processes for electrons and positrons. For photons the remaining energy is lost through the Compton effect and the photoelectric effect. Below the critical energy no new shower particles are produced. Electromagnetic cascades can be characterized by the radiation length, X_0, after which electrons/positrons reduced their energy to $1/e$ of their initial energy. For photons, it's equivalent to $7/9$ of the mean free path of pair production. The critical energy for ice is $E_c \approx 78\,\text{MeV}$, with a radiation length of $X_0 \approx 39.3\,\text{cm}$ [16].

The radiation length governs the longitudinal shower profile and using $t = x/X_0$, the shower intensity can be described by

$$\frac{dE}{dt} = E_0 b \frac{(bt)^{a-1} e^{-bt}}{\Gamma(a)} , \tag{2.6}$$

where a and b are parameters that have to be estimated from experiment. Based on the work from [47], performed with Geant4 [48], the parameters for electromagnetic showers in ice are

$$e^- : \; a \approx 2.01 + 1.45 \log_{10}(E_0/\text{GeV}),\, b \approx 0.63 , \tag{2.7a}$$
$$e^+ : \; a \approx 2.00 + 1.46 \log_{10}(E_0/\text{GeV}),\, b \approx 0.63 , \tag{2.7b}$$
$$\gamma : \; a \approx 2.84 + 1.34 \log_{10}(E_0/\text{GeV}),\, b \approx 0.65 . \tag{2.7c}$$

The maximum of the shower is at $t_{max} = (a-1)/b$ and the Cherenkov emission of the charged particles produced in the shower is peaked around the Cherenkov angle, since they are produced in the forward direction.

Hadronic Showers

The breaking nucleus or any hadronic decay products from the neutrino DIS interactions always create a hadronic cascade. It is a result of secondary particles produced in strong interactions between the hadrons and the traversed matter. The charged particles produced in the shower will emit Cherenkov radiation, while neutral particles will be invisible to the detector. There is also an electromagnetic component of the shower, due to for example the decay of neutral pions into photons. Hadronic showers of the same energy as electromagnetic showers have larger fluctuations in energy deposition and shape, since they depend on the produced particle types. Hadrons also have a higher energy threshold for Cherenkov light production, because of their higher mass. Based on [47, 49], the visible electromagnetic fraction of hadronic showers can be parameterized as

$$F(E_0) = \frac{T_{\text{hadron}}}{T_{\text{EM}}} = 1 - (1 - f_0)\left(\frac{E_0}{E_s}\right)^{-m} , \tag{2.8}$$

where $T_{\text{hadron/EM}}$ is the total track length of a hadronic/electromagnetic shower with the same energy, f_0 is the ratio of hadronic and electromagnetic light yield, E_0 is the initial energy, and E_s is an energy scale. The parameter m is an arbitrary parameter. The ratio $F(E_0)$ increases with energy, but is always smaller than 1. The variance of this distribution is given by

$$\sigma_F(E_0) = \sigma_0 \log(E_0)^{-\gamma} . \tag{2.9}$$

The parameters m, E_s, and f_0 are fit from simulation. Cherenkov light from hadronic showers also peaks around the Cherenkov angle, but the angular distribution is more smeared out, due to the variations in particle type and their energy depositions.

SB: Explain

2.3 Event Morphologies

The event morphologies produced by particles detected in IceCube are combinations of the three energy loss types described in Section 2.2.2, e.g. *cascades* from electromagnetic and hadronic showers and elongated *tracks* from muons traveling through the detector. Table 2.1 gives an overview of the possible event signatures.

Interaction	Secondary particles	Signature
CC $\overset{(-)}{\nu}_\mu$	$\mu^\pm$ track	Track-only
	$\mu^\pm$ track and hadrons	Cascade + track
CC $\overset{(-)}{\nu}_\tau$	$\tau^\pm$ decaying into $\mu^\pm$ (~17% BR), hadrons	
	$\tau^\pm$ decaying into $e^\pm$ or hadrons (~83% BR)	
CC $\overset{(-)}{\nu}_e$	$e^\pm$, hadrons	Cascade-only
NC $\overset{(-)}{\nu}_\ell$	hadrons	

Table 2.1: IceCube low energy event signatures, their underlying interaction type, and the particles that produce them. Also shown are the secondary particles produced in the interactions. Black dashed lines represent neutrinos, green lines muons, orange line leptons, and blue and red lines are particles in electromagnetic and hadronic cascades, respectively. Adapted from [11].

Neutrino interactions are observed as cascades, tracks, or a combination of both, depending on the initial flavor and the interaction type for the specific event.

In ν_μ - CC interactions, a muon is produced in addition to a hadronic shower from the breaking nucleus. If the interaction happens outside the detector, but the muon passes through the detector, this will create a track-like signature. The same happens if the interaction happens inside, but the energy transfer to the nucleus is small ($y \approx 0$). At energies relevant for this work, tracks have length at the same order of the distance between DOMs, so they can be observed as such.

Make sure I have this defined in the SM interaction chapter!

If the interaction happens inside the detector and the energy transfer to the hadronic part of the shower is larger, it will create a cascade with a track leaving it. A similar signature is observed after a ν_τ - CC interaction, in which a tau is produced that later decays into a muon, with a branching ratio of 17 %. In those cases the muon usually has a lower energy and the track will be fainter and harder to observe.

The other 83 % of ν_τ - CC interactions produce a tau that decays into an electron or hadrons, leaving a cascade-only signature through the electromagnetic or hadronic shower. All ν_e - CC interactions also produce pure cascades, since the electron quickly loses its energy in an electromagnetic shower. In all ν - NC interactions, the produced neutrino escapes and only the hadronic shower is observable. Since the size of the cascades at the energy range of interest is smaller than the spacing of the DOMs, they are approximately observed as point-like, spherical light sources. Considering the short effective scattering length (20 m-50 m), the light is almost isotropically emitted.

SB: Since your analysis depends on the ability to reconstruct cacade directions, it seems odd to emphasize that the light is nearly isotropically emitted. Of course that is true, but the emphasis should rather be on the fact that there remains some assymetry to the light profile

Atmospheric muons also produce pure track like signatures, similar to ν_μ - CC interactions happening outside the detector. They are one of the main backgrounds for analyses using atmospheric neutrinos and are therefore the target of many filter steps described in Section 4.3.1.

Heavy Neutral Lepton Signal Simulation

3

The central part of this thesis is the HNL signal simulation itself. Since this is the first search for HNLs with IceCube DeepCore, there was no prior knowledge of the number of events expected per year nor of the expected performance in terms of reconstruction and classification accuracy which governs the 90 % confidence level on estimateing the $|U_{\tau 4}|^2$ mixing matrix element. This is the first HNL simulation developed for IceCube DeepCore. Two avenues of simulation generation were pursued in parallel. The physically accurate, model dependent simulation is described in Section 3.2 and a collection of model independent simulation samples was realized and is explained in Section 3.1. The latter is used for performance benchmarking and as a cross-check for the model dependent simulation. The SM simulation generation and the default low energy event selection and processing chain are introduced in Chapter 4 and everything but the generation is applied identically to both neutrinos and HNLs.

3.1 Model Independent Simulation

To investigate the potential of IceCube to detect HNLs by identifying the unique double cascade morphology explained in Section 1.3.4, it is very valuable to have a simulation chain where the double cascade kinematics can be controlled directly. In a realistic model the decay kinematics and the absolute event expectation all depend on the specific model parameters chosen (see Section **??**). To decouple the simulation from a specific parameter choice, a model independent double cascade generator was developed. Using this generator several simulation samples were produced to investigate the performance of IceCube DeepCore to detect low energetic double cascades, dependent on their properties. All samples are produced using a collection of custom generator functions [50] that place two EM cascade vertices with variable energy and direction at choosable locations in the detector. The results of this study will be discussed in Chapter 5.

3.1.1 Simplistic Samples

Make my own DC string positions/distances plot version, viable for the margin?

Maybe just reference the one from the detector description and drop it here?

To investigate some idealistic double cascade event scenarios, two samples are produced for straight up-going events that are centered on a string and horizontal events located inside DeepCore.

The first sample is used to investigate one of the most promising scenarios to detect a double cascade, where both cascade centers are located on a DeepCore string (namely string 81) and the directions are directly up-going. The horizontal positions and distances of all DeepCore fiducial volume strings are shown in Figure 3.1 and string 81 is at a medium distance of $\sim$ 70 m to its neighboring strings. As already mentioned in Section 2.1.3, DeepCore strings have higher quantum efficiency DOMs and a denser vertical spacing, making them better to detect low energetic events that produce little light. To produce the events, the x, y position of the cascades

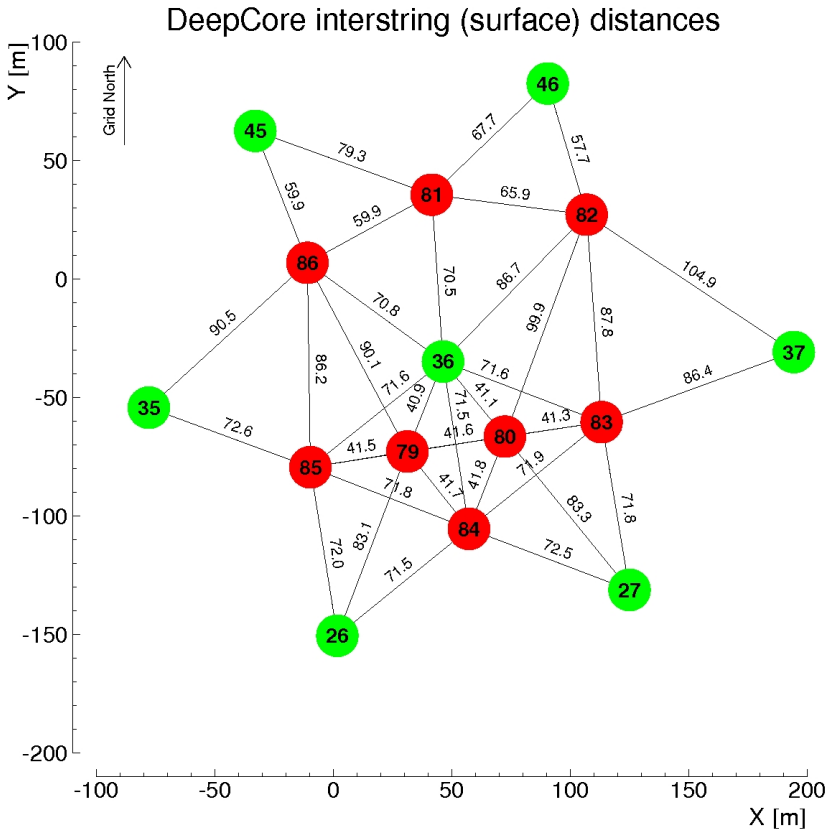

Figure 3.1: Horizontal positions and distances between DeepCore strings. Red strings are instrumented more densely (vertically) and partially have higher quantum efficiency (HQE) DOMs.

is fixed to the center of string 81 while the z position is sampled uniformly along the axis of the string. The energies are sampled uniformly between 0.0 GeV and 60.0 GeV. The specific sampling distributions/values for the cascades are listed in Table 3.1. The order of the cascades is chosen such that the lower one is first ($t_0 = 0.0$ ns) and the upper one is second ($t_1 = L/c$), assuming the speed of light c as speed of the heavy mass state, traveling between the two cascades.

Re-make plot with all energies (cascades and total, both samples (they are the same))

Re-make plot with all decay lengths (both samples)

The second sample is used to investigate the reconstruction performance for horizontal events, where the spacing between DOMs is much larger. The cascades are placed uniformly on a circle centered in DeepCore. The direction is always horizontal and azimuth is defined by the connecting vector of both cascade positions. The energies are again sampled uniformly between 0.0 GeV and 60.0 GeV and the detailed sampling distributions/values are also listed in Table 3.1. Some examples of the generation level distributions of the simplified samples are shown in Figure 3.2, while further distributions can be found in Figure A.1.

3.1.2 Realistic Sample

To thoroughly investigate the potential of IceCube DeepCore to detect double cascade events, a more realistic simulation sample is produced that aims to be as close as possible to the expected signal simulation explained in Section 3.2, while still allowing additional freedom to control the double cascade kinematics. For this purpose the total energy is sampled from an E^{-2} power law, mimicking the energy spectrum of the primary neutrinos as stated in Section 4.1.1. The total energy is divided into two parts, by randomly

Sample	Variable	Distribution	Range/Value
Up-going			
	energy	uniform	0.0 GeV to 60.0 GeV
	zenith	fixed	180.0°
	azimuth	fixed	0.0°
	x, y position	fixed	(41.6, 35.49) m
	z position	uniform	−480.0 m to −180.0 m
Horizontal			
	energy	uniform	0.0 GeV to 60.0 GeV
	zenith	fixed	90.0°
	azimuth	uniform	0.0° to 360.0°
	x, y position	uniform (circle)	c=(46.29, -34.88) m, r=150.0 m
	z position	fixed	−330.0 m

Table 3.1: Generation level sampling distributions and ranges/values of up-going and horizontal model independent simulation.

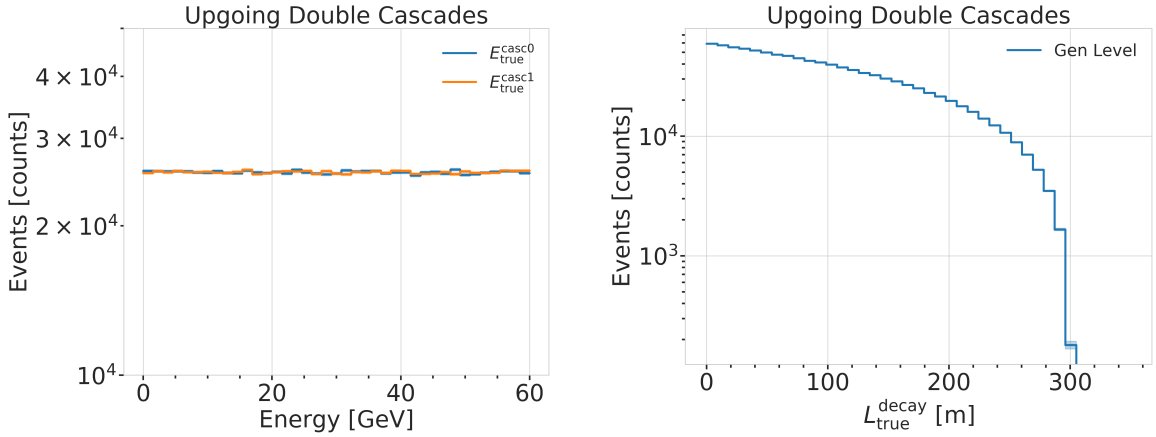

Figure 3.2: Generation level distributions of the simplistic simulation samples. Cascade and total energies (left) and decay lengths (right) of both samples are shown.

assigning a fraction between 0 % and 100 % to one cascade and the remaining part to the other cascade. This is a generic approximation of the realistic process described in Section 3.2, and chosen such that the whole sample covers various cases of energy distributions between the two cascades. To efficiently generate events in a way that produces distributions similar to what would be observed with DeepCore, one of the cascade positions is sampled inside the DeepCore volume by choosing its coordinates randomly on a cylinder that is centered in DeepCore. This is similar to a trigger condition of one cascade always being inside the DeepCore fiducial volume. By choosing the direction of the event by sampling zenith and azimuth uniformly between 70° and 180° and 0° and 360°, respectively, the position of the other cascade can be inferred for a given decay length, assuming a travel speed of c, and randomly choosing whether the cascade position that was sampled is the first cascade or the second. The decay length is sampled from an exponential distribution, as expected for a decaying heavy mass state. The sampling distributions/values are listed in Table 3.4. Example distributions of the generation level variables are shown in Figure 3.3, while further distributions can be found in Figure A.2.

Table 3.2: Generation level sampling distributions and ranges/values of the realistic model independent simulation.

Variable	Distribution	Range/Value
energy (total)	power law E^{-2}	1 GeV to 1000 GeV
decay length	exponential $e^{-0.01L}$	0 m to 1000 m
zenith	uniform	70° to 180°
azimuth	uniform	0° to 360°
x, y (one cascade)	uniform (circle)	c=(46.29, -34.88) m, r=150 m
z (one cascade)	uniform	−480.0 m to −180.0 m

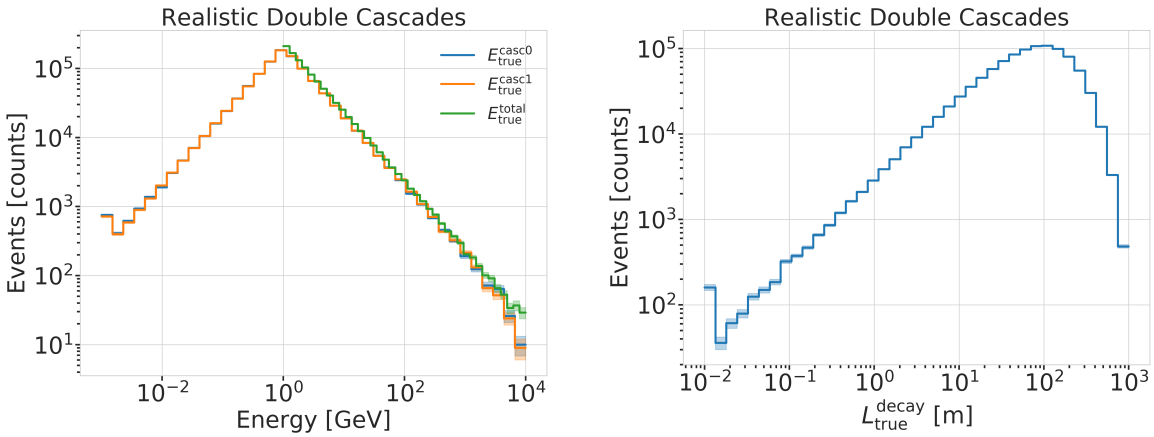

Figure 3.3: Generation level distributions of the simplistic realistic sample. Shown are the cascade and total energies (left) and decay lengths (right).

3.2 Model Dependent Simulation

To estimate the HNL event expectation in IceCube DeepCore, depending on the specific model parameters, a generator was developed that is based on the HNL theory introduced in Section **??**. For this work, only the interaction with the τ-sector was taken into account ($|U^2_{\alpha 4}| = 0$, $\alpha = e, \mu$), which reduces the physics parameters of interest and relevent for the simulation to the fourth heavy lepton mass, m_4, and the mixing, $|U^2_{\tau 4}|$. The generator uses a customized *LeptonInjector (LI)* version to create the events and *LeptonWeighter (LW)* to weight them [51]. The modified LI and the essential components needed for the HNL simulation are described in the next sections, followed by the description of the weighting scheme and the sampling distributions chosen for the simulation generation.

[51]: Abbasi et al. (2021), "LeptonInjector and LeptonWeighter: A neutrino event generator and weighter for neutrino observatories"

3.2.1 Custom LeptonInjector

In its standard version, the LI generator produces neutrino interactions by injecting a lepton and a hadronic cascade at the interaction vertex of the neutrino, where the lepton is the charged (neutral) particle produced in a CC (NC) interaction and the cascade is the hadronic cascade from the breaking nucleus. The hadronic cascade is stored as a specific object of type *Hadrons*, which triggers the correct simulation of the shower development in the following simulation steps, identical to what will be described for SM neutrino simulation on Section 4.1.1. The main differences to an EM cascade is that part of the energy will not be observed, because it goes into neutral particles, and that the spatial development of the shower is different. Both objects are injected with the same (x, y, z, t) coordinates and the kinematics

are sampled from the differential and total cross-sections that are one of the inputs to LI.

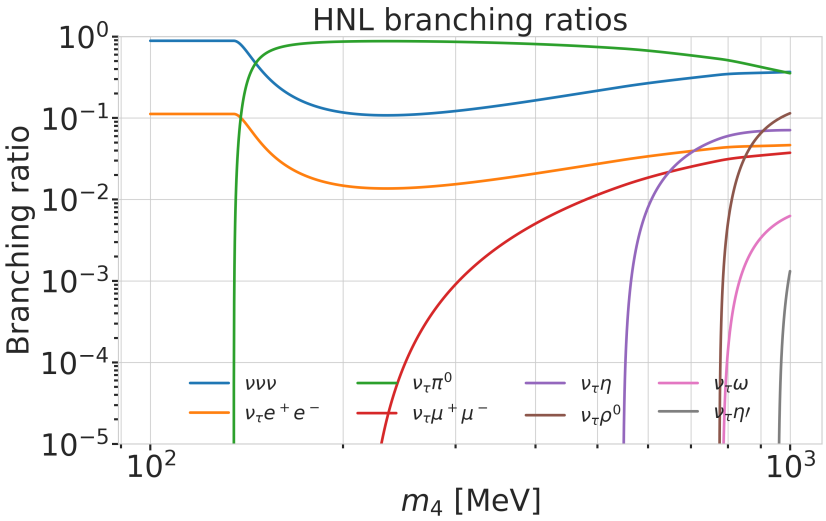

Figure 3.4: Branching ratios of the HNL within the mass range considered in this work, only considering $|U_{\tau 4}^2| \neq 0$, calculated based on the results from [20].

In the modified version, the SM lepton at the interaction vertex is replaced by the new HNL particle, where the interaction cross-sections are replaced by custom, mass dependent HNL cross-sections. The HNL is forced to decay after a chosen distance to produce secondary SM particles, where the decay mode is randomly chosen based on the mass dependent branching ratios from the kinematically accessible decay modes shown in Figure 3.4. The cross-section and decay width calculations were implemented for this purpose and will be explained in more detail in the following. Another needed addition to LI is that the decay products of the HNL are also added to the list of MC particles in each event. They are injected with the correctly displaced position and delayed time from the interaction vertex, given the HNL decay length. These HNL daughter particles form the second cascade, not as a single hadronic cascade object, but as the explicit particles forming the shower. The kinematics of the two-body decays are computed analytically, while the three-body decay kinematics are calculated with MadGraph [52], which will also be explained further below. Independent of the number of particles in the final state of the HNL decay, the kinematics are calculated/simulated at rest and then boosted along the HNL momentum.

[52]: Alwall et al. (2014), "The automated computation of tree-level and next-to-leading order differential cross sections, and their matching to parton shower simulations"

The injection is done using the LI *volume mode*, for the injection of the primary particle on a cylindrical volume, adding 50 % of the events with ν_τ and the other half with $\bar{\nu}_\tau$ as primary particle types. The generator takes the custom double-differential/total cross-section splines described below and the parameters defining the sampling distributions as inputs.

Cross-Sections

The cross-sections are calculated using the NuXSSplMkr [53] software, which is a tool to calculate neutrino cross-sections from *parton distribution functions (PDFs)* and then produce splines that can be read and used with LI/LW. The tool was customized to produce the custom HNL cross-sections, where the main modification to calculate the cross-sections for the ν_τ-NC interaction into the new heavy mass state is the addition of a kinematic condition to ensure that there is sufficient energy to produce the heavy mass

In which variables are they splined?

state. It is the same condition fulfilled for the CC case, where the outgoing charged lepton mass is non-zero. Following [54] (equation 7), the condition

$$(1 + x\delta_N)h^2 - (x + \delta_4)h + x\delta_4 \leq 0 \tag{3.1}$$

is implemented for the NC case in the NuXSSplMkr code. Here

$$\delta_4 = \frac{m_4^2}{s - M^2}\,, \tag{3.2}$$

$$\delta_N = \frac{M^2}{s - M^2}\,, \text{and} \tag{3.3}$$

$$h \overset{def}{=} xy + \delta_4\,, \tag{3.4}$$

with x and y being the Bjorken variables, m_4 and M the mass of the heavy state and the target nucleon, respectively, and s the center of mass energy squared.

[54]: Levy (2009), "Cross-section and polarization of neutrino-produced tau's made simple"

Re-make plot with 3 target masses and better

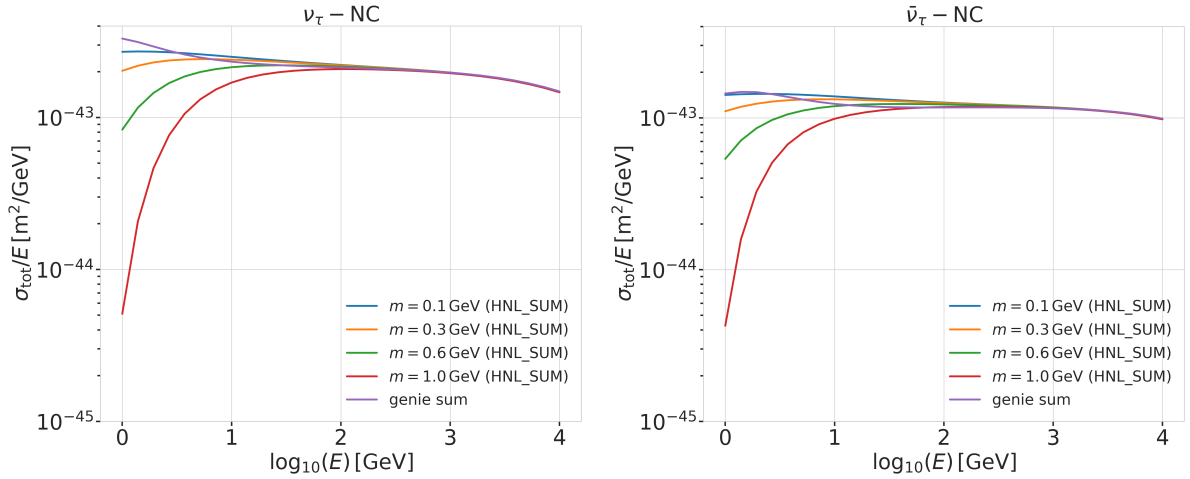

Figure 3.5: Custom HNL total cross-sections for the four target masses compared to the total ($\nu_\tau/\bar{\nu}_\tau$ NC) cross-section used for SM neutrino simulation production with GENIE.

The GRV98LO PDFs were added to the cross-section spline maker and used to create the HNL cross-sections for consistency with the SM neutrino simulation that will be explained in Section 4.1.1. The double differential ($d\sigma dxdy$) and total (σ) cross-sections were produced for the chosen target HNL masses and then splined. The produced cross-section are added to the custom LI version and used for the simulation generation and weighting. Figure 3.5 shows the total cross-sections that were produced compared to the cross-section used for the production of the SM $\nu_\tau/\bar{\nu}_\tau$ NC background simulation. Above $\sim 2 \times 10^2$ GeV they match, which is the desired result of using the identical input PDFs.

SB: emphasize the cut-off/suppression

Add comparisons of SM cross-sections between NuXSSplMkr and genie?

add varied total cross-section for a few background HNL events (for QE/RES variations?!)

Decay Channels

The accessible decay channels are dependent on the mass of the HNL and the allowed mixing. For this analysis, where only $|U_{\tau 4}|^2 \neq 0$, the decay channels considered are listed in Table 3.3 and the corresponding branching ratios are shown in Figure 3.4. The individual branching ratio for a specific mass is calculated as $\text{BR}_i(m_4) = \Gamma_i(m_4)/\Gamma_{\text{total}}(m_4)$, where $\Gamma_{\text{total}}(m_4) = \sum \Gamma_i(m_4)$.

The individual decay widths Γ_i are computed using the state-of-the-art calculations from [20], which are described in the following.

[20]: Coloma et al. (2021), "GeV-scale neutrinos: interactions with mesons and DUNE sensitivity"

2-Body Decay Widths The decay to a neutral pseudoscalar meson is

$$\Gamma_{\nu_4 \to \nu_\tau P} = |U_{\tau 4}|^2 \frac{G_F^2 m_4^3}{32\pi} f_P^2 (1 - x_p^2)^2 \,, \tag{3.5}$$

with $x_P = m_P / m_4$ and the *effective decay constants* f_P given by

$$f_{\pi^0} = +0.1300\,\text{GeV} \,, \tag{3.6}$$
$$f_\eta = +0.0816\,\text{GeV} \,, \text{and} \tag{3.7}$$
$$f_{\eta'} = -0.0946\,\text{GeV} \,, \tag{3.8}$$

while the decay to a neutral vector meson is given by

$$\Gamma_{\nu_4 \to \nu_\tau V} = |U_{\tau 4}|^2 \frac{G_F^2 m_4^3}{32\pi} \left(\frac{f_V}{m_V} \right)^2 g_V^2 (1 + 2x_V^2)(1 - x_V^2)^2 \,, \tag{3.9}$$

with $x_V = m_V / m_4$,

$$f_{\rho^0} = 0.171\,\text{GeV}^2 \,, \tag{3.10}$$
$$f_\omega = 0.155\,\text{GeV}^2 \,, \tag{3.11}$$

and

$$g_{\rho^0} = 1 - 2\sin^2\theta_w \,, \tag{3.12}$$
$$g_\omega = \frac{-2\sin^2\theta_w}{3} \,, \tag{3.13}$$

and $\sin^2\theta_w = 0.2229$ [55].

Channel	Opens	$\hat{BR}$
$\nu_4 \to \nu_\tau \nu_\alpha \bar{\nu_\alpha}$	0 MeV	1.0
$\nu_4 \to \nu_\tau e^+ e^-$	1 MeV	?
$\nu_4 \to \nu_\tau \pi^0$	135 MeV	?
$\nu_4 \to \nu_\tau \mu^+ \mu^-$	211 MeV	?
$\nu_4 \to \nu_\tau \eta$	548 MeV	?
$\nu_4 \to \nu_\tau \rho^0$	770 MeV	?
$\nu_4 \to \nu_\tau \omega$	783 MeV	?
$\nu_4 \to \nu_\tau \eta'$	958 MeV	?

Table 3.3: Possible decay channels of the HNL, considering only $|U_{\tau 4}|^2 \neq 0$. Listed is the mass at which each channel opens and the maximum branching ratio.

Calculate max BRs

[55]: Tiesinga et al. (2021), "CODATA recommended values of the fundamental physical constants: 2018"

3-Body Decay Widths The (invisible) decay to three neutrinos is

$$\Gamma_{\nu_4 \to \nu_\tau \nu_\alpha \bar{\nu_\alpha}} = |U_{\tau 4}|^2 \frac{G_F^2 m_4^5}{192\pi^3} \,, \tag{3.14}$$

while the decay to two charged leptons (using $x_\alpha = (m_\alpha / m_4)^2$) of the same flavor reads

$$\Gamma_{\nu_4 \to \nu_\tau l_\alpha^+ l_\alpha^-} = |U_{\tau 4}|^2 \frac{G_F^2 m_4^5}{192\pi^3} \left[C_1 f_1(x_\alpha) + C_2 f_2(x_\alpha) \right] \,, \tag{3.15}$$

with the constants defined as

$$C_1 = \frac{1}{4}(1 - 4s_w^2 + 8s_w^4) \,, \tag{3.16}$$
$$C_2 = \frac{1}{2}(-s_w^2 + 2s_w^4) \,, \tag{3.17}$$

the functions as

$$f_1(x_\alpha) = (1 - 14x_\alpha - 2x_\alpha^2 - 12x_\alpha^3)\sqrt{1 - 4x_\alpha} + 12x_\alpha^2(x_\alpha^2 - 1)L(x_\alpha) \,, \tag{3.18}$$

$$f_2(x_\alpha) = 4[x_\alpha(2+10x_\alpha-12x_\alpha^2)\sqrt{1-4x_\alpha}+6x_\alpha^2(1-2x_\alpha+2x_\alpha^2)L(x_\alpha)]\ , \quad (3.19)$$

and

$$L(x) = \ln\left(\frac{1-3x_\alpha-(1-x_\alpha)\sqrt{1-4x_\alpha}}{x_\alpha(1+\sqrt{1-4x_\alpha})}\right). \quad (3.20)$$

JVS: consider also writing down the (trivial) 2-body decay kinematics for completeness and consistency. This transition is a bit jarring as it is

[20]: Coloma et al. (2021), "GeV-scale neutrinos: interactions with mesons and DUNE sensitivity"

3-Body Decay Kinematics with MadGraph

The specific MadGraph version used to produce the 3-body decay kinematics is MadGraph4 v3.4.0. As input, the decay diagrams calculated with FeynRules 2.0 using the Lagrangians derived in [20]. The Universal FeynRules Output (UFO) from EFFECTIVE_HEAVYN_MAJORANA_v103 were used for our calculation. For each mass and corresponding decay channels, we produce 1×10^6 decay kinematic variations in the rest frame and store those in a text file. During event generation, we uniformly select an event from that list, to simulate the decay kinematics of a 3-body decay.

3.2.2 Sampling Distributions

In principle, the generation level sampling distributions should be chosen such that at final level of the selection chain the phase space relevant for the analysis is covered with sufficient statistics to make a reasonable estimate of the event expectation. Initial distributions insufficiently covering the phase space lead to an underestimate of the expected rates, because part of the events that would pass the selection are not produced. This limits the expected analysis potential. Three discrete simulation samples were produced with HNL masses of 0.3 GeV, 0.6 GeV and 1.0 GeV. Because during development it became clear that the low lengths component is crucial to get a reasonable event estimate, each sample consists of a part that is generated for very short decay lengths and one for long decay lengths. The remaining sampling distributions are identical for all samples and are listed in Table 3.4. The target number of events for each sample was 2.5×10^9.

Table 3.4: Generation level sampling distributions and ranges/values of the model dependent simulation samples.

Variable	Distribution	Range/Value
energy	E^{-2}	[2 GeV, 1×10^4 GeV]
zenith	uniform (in $\cos(\theta)$)	[80°, 180°]
azimuth	uniform	[0°, 360°]
vertex x, y	uniform	r=600 m
vertex z	uniform	−600 m to 0 m
m_4	fixed	[0.3, 0.6, 1.0] GeV
L_{decay}	L^{-1}	[0.0004, 1000] m

3.2.3 Weighting Scheme

To produce physically correct event distributions based on the simplified generation sampling distributions for the HNL simulation, the forward folding method that was already introduced for the SM simulation in Section 4.1 is also used. The weighting scheme that will be explained in the following is implemented in a custom stage[1] in the IceCube low energy analysis

1: An analysis in PISA is a collection of functions that are written in so-called *stages*. The stages can be combined in a *pipeline* and are executed in a specific order. This particular stage is located in `pisa/stages/aeff/weight_hnl.py`.

framework PISA [56], which will be discussed in Section 6.2.1. The only required input is the mixing strength $|U_{\tau 4}|^2$, which is the variable physics parameter in this analysis. For each event the gamma factor

$$\gamma = \frac{\sqrt{E_{\text{kin}}^2 + m_4^2}}{m_4} , \tag{3.21}$$

is calculated, with the HNL mass m_4, and its kinetic energy E_{kin}. The speed of the HNL is calculated as

$$v = c \cdot \sqrt{1 - \frac{1}{\gamma^2}} , \tag{3.22}$$

where c is the speed of light. With these, the lab frame decay length range $[s_{\text{min}}, s_{\text{max}}]$ can be converted into the rest frame lifetime range $[\tau_{\text{min}}, \tau_{\text{max}}]$ for each event

$$\tau_{\text{min/max}} = \frac{s_{\text{min/max}}}{v \cdot \gamma}. \tag{3.23}$$

The proper lifetime of each HNL event can be calculated using the total decay width Γ_{total} from Section 3.2.1 and the chosen mixing strength $|U_{\tau 4}|^2$ as

$$\tau_{\text{proper}} = \frac{\hbar}{\Gamma_{\text{total}}(m_4) \cdot |U_{\tau 4}|^2} , \tag{3.24}$$

where $\hbar$ is the reduced Planck constant. Since the decay lengths or lifetimes of the events are sampled from an inverse distribution instead of an exponential, as it would be expected from a particle decay, we have to re-weight accordingly to achieve the correct decay lengths or lifetimes distribution. This is done by using the wanted exponential distribution

$$\text{PDF}_{\text{exp}} = \frac{1}{\tau_{\text{proper}}} \cdot e^{\frac{-\tau}{\tau_{\text{proper}}}} , \tag{3.25}$$

and the inverse distribution that was sampled from

$$\text{PDF}_{\text{inv}} = \frac{1}{\tau \cdot (\ln(\tau_{\text{max}}) - \ln(\tau_{\text{min}}))} . \tag{3.26}$$

This re-weighting factor is then calculated as

$$w_{\text{lifetime}} = \frac{\text{PDF}_{\text{exp}}}{\text{PDF}_{\text{inv}}} = \frac{\Gamma_{\text{total}}(m_4) \cdot |U_{\tau 4}|^2}{\hbar} \cdot \tau \cdot (\ln(\tau_{\text{max}}) - \ln(\tau_{\text{min}})) \cdot e^{\frac{-\tau}{\tau_{\text{proper}}}} . \tag{3.27}$$

Adding another factor of $|U_{\tau 4}|^2$ to account for the mixing at the interaction vertex the total re-weighting factor becomes

$$w_{\text{total}} = |U_{\tau 4}|^2 \cdot w_{\text{lifetime}} . \tag{3.28}$$

If this additional weighting factor is multiplied to a generation weight with units m^2 (like in Equation 4.1), the livetime in s, and the oscillated primary neutrino flux in $\text{m}^{-2}\text{s}^{-1}$, it results in the number of expected events in the detector for this particular MC event for a chosen mixing (and mass).

add table with number of gen level files? mention the event number is smaller because of kinemtic condition?

3.2.4 Generation Level Distributions

Figure 3.6 shows some selected generation level distributions. Additional distributions can be found in Figure A.3.

Combine low/high plots and remove all traces

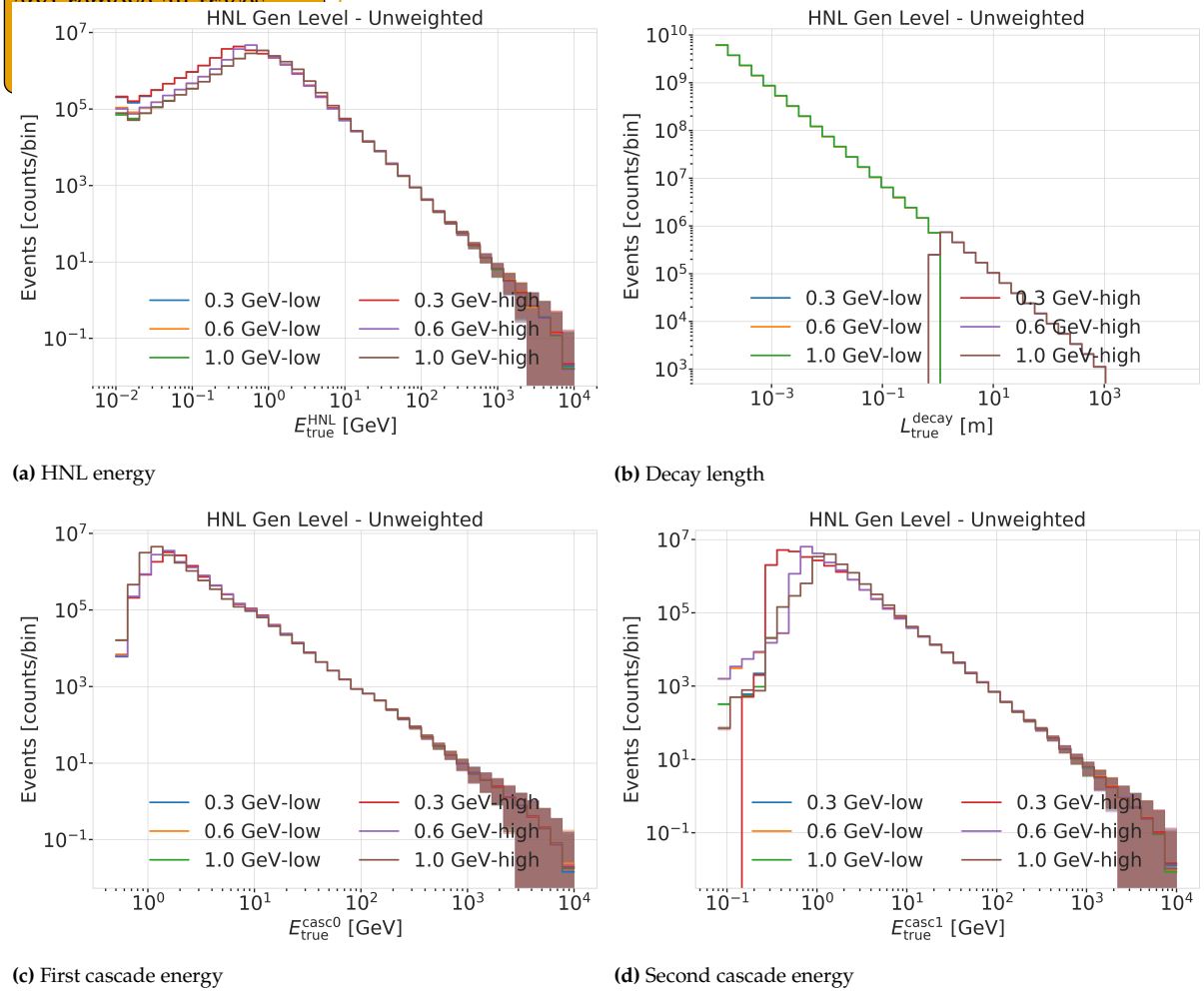

(a) HNL energy

(b) Decay length

(c) First cascade energy

(d) Second cascade energy

Figure 3.6: Generation level distributions of the model dependent simulation.

Standard Model Background Simulation and Data Processing

4

Adapt chapter to reflect switched chapter order

The analysis presented in this thesis is highly dependent on an efficient event selection to reduce the raw IceCube trigger data to a usable atmospheric neutrino sample. Based on this selection, a precise estimation of both expected SM background and expected BSM signal events can be made using MC simulations. This chapter describes the current simulation and event selection chain used for state-of-the-art IceCube neutrino oscillation measurements like [57]. The whole chain can be broadly split into 4 steps:

[57]: Abbasi et al. (2023), "Measurement of atmospheric neutrino mixing with improved IceCube DeepCore calibration and data processing"

Step 1 Event Generation: The initial step for all particle (non-noise) simulation is the generation of events from selected initial distributions and fluxes. Events are the primary particle and the particles produced in the interaction with the ice.

Step 2 Detector Simulation: The particles from the first step are propagated through the ice, producing Cherenkov photons, which are then propagated further until they reach a DOM or are absorbed. If they hit a DOM the detector response (acceptance and PMT) is simulated.

Step 3 Processing: Starting from the PMT output, both real data and simulation are processed through the in-ice trigger, the online filter and processing, and the low energy event selection to produce a neutrino dominated sample.

Step 4 Reconstruction: Once the sample is small enough for more sophisticated reconstruction techniques to be feasible to run, the events are reconstructed using a CNN and some high level variables are computed. Based on these variables the final event selection is applied.

This chapter only describes the event generation for the SM background simulation (neutrinos and muons), while the signal simulation is described in Chapter 3. The detector simulation is identical for both signal and background events while processing and reconstruction are applied to all simulation and data in the same way. Splitting the simulation steps has the advantage of reusing the outputs of for example the generation step to propagate the particles with different ice model, in order to estimate the systematic impacts of uncertainties of the ice properties. Similar approach can be taken for varying detector response and through this a more efficient (reduced) use of computing resources can be achieved. The following sections describe the different steps in more detail and the last section, Section 4.5, describes the related systematic uncertainties considered for this work.

4.1 Event Generation

The MC is used in the analysis by applying a method called *forward folding*, where a very large number of events (signal and background) is produced using sampling distribution that are tuned to have a large selection efficiency. Those distributions don't have to be physically correct distributions, but they need to cover the full parameter space of interest for the analysis. To produce a physical distribution, the events are weighted given a specific

Table 4.1: Cylinder volumes used for GENIE neutrino simulation generation. Cylinder is always centered in DeepCore at $(x, y, z) = (46.29, -34.88, -330.00)$ m.

Flavor	Energy [GeV]	Radius [m]	Length [m]	Events/File	Files
$\nu_e + \bar{\nu_e}$	1-4	250	500	450000	650
	4-12			100000	
	12-100	350	600		
	100-10000	550	1000	57500	
$\nu_\mu + \bar{\nu_\mu}$	1-5	250	500	408000	1550
	5-80	400	900	440000	
	80-1000	450	1500	57500	
	1000-10000	550		6700	
$\nu_\tau + \bar{\nu_\tau}$	1-4	250	500	1500000	350
	4-10			300000	
	10-50	350	600	375000	
	50-1000	450	800	200000	
	1000-10000	550	1500	26000	

choice of physics and nuisance parameters. The large number of raw MC events ensures a good estimation of the expected numbers and weighted distributions.

The analysis itself is then performed by comparing the weighted MC distributions to the observed data. This is done by binning them as described in Chapter 6 and calculating a loss function comparing the bin expectations to the data. The physics and nuisance parameters that best correspond to the observed data are estimated by minimizing this loss function. In order to achieve a reliable result with this method the MC needs to be precise and as close to the data as possible (at least at the final event selection).

4.1.1 Neutrinos

Due to the very low interaction rate of neutrinos, the event generation is performed in a way that forces every event to interact in a chosen sampling volume. The weight of each event is then calculated as the inverse of the simulated neutrino fluence

$$w = \frac{1}{F_{\text{sim}}} \frac{1}{N_{\text{sim}}} , \tag{4.1}$$

where F_{sim} is the number of neutrino events per energy, time, area, and solid angle and N_{sim} is the number of simulated events. If this weight is multiplied by the livetime and the theoretically expected neutrino flux for a given physical model, it results in the number of expected events in the detector for this particular MC event. The baseline neutrino flux used in this thesis, computed for the South Pole, is taken from Honda *et al.* [21].

[21]: Honda et al. (2015), "Atmospheric neutrino flux calculation using the NRLMSISE-00 atmospheric model"

The simulation volume is a cylinder centered in DeepCore with radius and height chosen such that all events possibly producing a signal are contained. The different sizes, chosen depending on energy and neutrino flavor, are shown in Table 4.1. The directions of the neutrinos are sampled isotropically and the energies are sampled from an E^{-2} power law. The number of simulated events is chosen such that the livetime is more than 70 years for each flavor. Neutrinos and antineutrinos are simulated with ratios of 70% and 30%, respectively.

To simulate the neutrino interaction with the ice, the GENIE event generator [58] (version 2.12.8) is used, resulting in the secondary particles and the kinematic and cross-section parameters. As input, the outdated GRV98LO [59] *parton distribution functions (PDFs)* was used, because it was the only option that could incorporate extrapolations to lower Q^2 [60]. Muons produced in these interactions are propagated using PROPOSAL [61], also simulating their Cherenkov light output. The shower development of gamma rays, electrons, and positrons below 100 MeV and hadronic showers below 30 GeV is simulated using GEANT4 [48] while for higher energies an analytical approximation from [45] is used.

[58]: Andreopoulos et al. (2015), "The GENIE Neutrino Monte Carlo Generator: Physics and User Manual"

[59]: Glück et al. (1998), "Dynamical parton distributions revisited"

[60]: Bodek et al. (2003), "Higher twist, xi(omega) scaling, and effective LO PDFs for lepton scattering in the few GeV region"

[61]: Koehne et al. (2013), "PROPOSAL: A tool for propagation of charged leptons"

[48]: Agostinelli et al. (2003), "Geant4—a simulation toolkit"

[45]: Rädel et al. (2012), "Calculation of the Cherenkov light yield from low energetic secondary particles accompanying high-energy muons in ice and water with Geant4 simulations"

[62]: Becherini et al. (2006), "A parameterisation of single and multiple muons in the deep water or ice"

[63]: Heck et al. (1998), "CORSIKA: A Monte Carlo code to simulate extensive air showers"

[64]: Gaisser (2012), "Spectrum of cosmic-ray nucleons, kaon production, and the atmospheric muon charge ratio"

[65]: Engel et al. (2017), "The hadronic interaction model Sibyll – past, present and future"

4.1.2 Muons

Atmospheric muons are generated on a cylinder surface enclosing the full IceCube detector array. The cylinder has a height of 1600 m and a radius of 800 m. The energy is sampled from an E^{-3} power law while the other sampling distributions (position, direction) are found from parameterizations based on [62]. This work uses full CORSIKA [63] simulations of muons to tailor the parameterizations, starting from *cosmic ray (CR)* interactions with atmospheric nuclei using the CR flux model from [64] and producing the muons applying the *hadronic interaction (HI)* model SIBYLL 2.1 [65]. After the generation, they are propagated through the ice with PROPOSAL producing photons, treating them exactly like the muons produced in neutrino interactions.

Since the offline processing and selection steps described in Section 4.3.2 and Section 4.4 reduce the muon contamination to an almost negligible level, the statistical uncertainty on the number of expected muon events at the final selection level is large and therefore two separate sets of muon simulation are produced. **A first set** including all events resulting from the above described generation to tune the lower level selection (up to L4) and **a second set** to estimate the muon contamination at higher levels (above L5), which only accepts muon events if they pass through a smaller cylinder centered in DeepCore (height of 400 m and radius of 180 m) and rejects events based on a KDE estimated muon density at L5 (in energy and zenith) increasing the simulation efficiency at L5 significantly .

put a number on this significant increase?

4.2 Detector Simulation

The detector simulation is performed after the event generation, where the initial particles and the resulting photons and secondary particles from their propagation were produced. This part of the simulation chain is applied to all muon and neutrino simulation as well as the HNL signal simulation explained in detail in Chapter 3. The detector simulation can be split into two parts, the propagation of the photons and the simulation of the detector response (including internal noise).

4.2.1 Photon Propagation

Any photon that was produced in the event generation is individually traced through the ice, simulating scattering and absorption processes. The

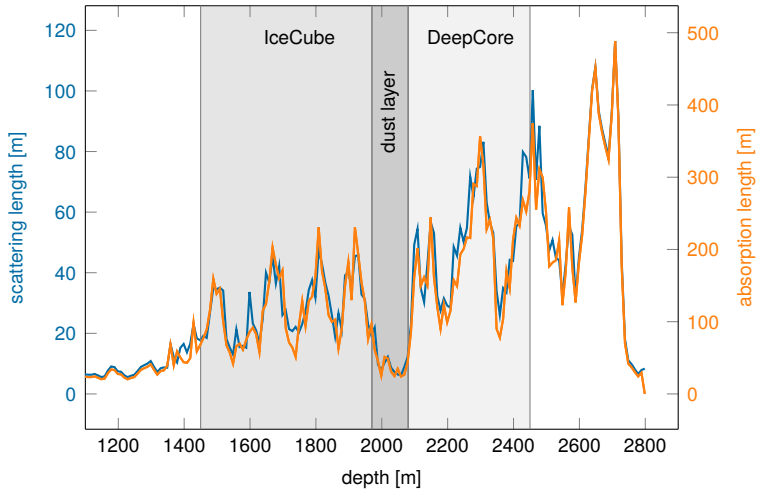

Figure 4.1: Scattering and absorption lengths in the SPICE model used for simulation production as a function of depth, modified from [69].

propagation is done using CLSIM [66] which is an implementation of the *Photon Propagation Code (PPC)* [67] in OpenCL. It is optimized to be run very efficiently on GPUs, which is what is done for IceCube simulation production. The ice is modeled as a set of 10 m thick, almost horizontal layers with specific absorption and scattering lengths. The *South Pole ice (SPICE)* model [68] accounts for the layers being tilted by a small amount () and the absorption and scattering lengths having a non-uniformity with respect to the azimuth direction. Figure 4.1 shows the values of this model for the different depths, indicating the location of IceCube, DeepCore, and the dust layer.

[67]: Chirkin et al. (2019), "Photon Propagation using GPUs by the IceCube Neutrino Observatory"

[68]: Aartsen et al. (2013), "Measurement of South Pole ice transparency with the IceCube LED calibration system"

put a number on the tilt angle?

In an initial step, each photon's absorption length is sampled from an exponential distribution with the expectation value at the current layer's absorption length. The following propagation steps are performed in parallel for all photons. In each of those steps, corresponding to a single scattering event, the photon travels a length that is sampled from an exponential distribution with the expectation value at the scattering length of the current layer and the scattering angle chosen based on a combination of a simplified Mie scattering distribution [70] and a Henyey-Greenstein distribution [71]. The parameters defining the shape of these distributions were calibrated using data from *in-situ* LED calibration runs. These steps are continuously repeated until each photon reached a DOM or was absorbed[1]. After all photons have been propagated in that manner, the final step is to output the photons that reached a DOM for further processing.

[70]: Mie (1908), "Beiträge zur Optik trüber Medien, speziell kolloidaler Metallösungen"

[71]: Henyey et al. (1941), "Diffuse radiation in the Galaxy."

1: A photon is absorbed, when it traveled its full absorption length, sampled in the initial step of the photon propagation.

4.2.2 Detector Responses

The second part of simulating the IceCube detector is the DOM response. Whether a photon that reached a DOM produces a signal depends on the total efficiency and the angular acceptance curve of the specific DOM. The total efficiency includes effects of the DOM glass, PMT quantum and photoelectron collection efficiencies, and it is wavelength dependent. Additionally, there is another angle dependent effect called *hole ice* [72]. This effect is due to varied ice properties resulting from the re-freezing process of the water column inside the borehole after deployment of the string. Accepted photons are converted into a so-called *Monte Carlo photo-electron (MCPE)*. The amount of charge measured for each MCPE is determined by sampling

[72]: Fiedlschuster (2019), "The Effect of Hole Ice on the Propagation and Detection of Light in IceCube"

from a mixture of two exponential distributions and a normal distribution. This *single photo-electron (SPE)* distribution was tuned to match the observed distribution in each DOM in an *in-situ* calibration study [73]. Figure **??** shows the distribution compared to a lab measurement. Based on the sampled charges and times of MCPEs, the voltage waveforms for the (two) different readout channels are simulated and passed on to the trigger simulation starting with *WaveDeform*, which was already mentioned in Section 2.1.1.

[73]: Aartsen et al. (2020), "In-situ calibration of the single-photoelectron charge response of the IceCube photomultiplier tubes"

Add SPE distribuiton plot

Besides the Cherenkov photons, IceCube also observes photons that are produced in radioactive decays inside the DOMs, both in the glass housing sphere and the PMT glass itself. To simulate this internal noise, the *Vuvuzela* module [74, 75] is used to create additional MCPEs that are fed into the same simulation chain described above. This module takes into account thermal and non-thermal components and their times are sampled using parameterizations of the measured distributions, where the thermal noise component is uncorrelated photons and the non-thermal component is from burst of photons. The noise hits are simulated by drawing the times from a constant rate Poisson process and the number of photons from a Poisson distribution. Then the time differences between the individual photons per hit is found, based on a Log-Normal distribution. The simulation is defined by 5 parameters that are calibrated for each DOM individually. Table 4.2 shows the average values for these parameters.

Parameter	Value
Therm. rate λ_{th}	180 Hz
Decay rate λ_{dec}	80 Hz
Decay hits η	8.5
Decay μ	4.3 $\log_{10}$(ns)
Decay σ	1.8 $\log_{10}$(ns)

Table 4.2: Typical parameter values used in the vuvuzela noise simulation. Averaged over all DOMs.

[74]: Larson (2013), "Simulation and Identification of Non-Poissonian Noise Triggers in the IceCube Neutrino Detector"
[75]: Larson (2018), "A Search for Tau Neutrino Appearance with IceCube-DeepCore"

4.3 Processing

After the detector simulation is performed, all MC and data are processed in exactly the same way. This section explains the trigger and event selection that is applied starting from the raw voltage measured by the PMTs. Most parts of this processing are identical to the procedure already described in [69, 76]. It is split in different steps run inside the ice, at the South Pole, and after the data was transferred to the North. The complexity and computational cost of the processing increases with each step, while the total number of events reduces, making it feasible and reducing the use of computational resources on events that are not of interest for the analysis.

[69]: Trettin (2023), "Search for eV-scale sterile neutrinos with IceCube DeepCore"
[76]: Lohfink (2023), "Testing non-standard neutrino interaction parameters with IceCube-DeepCore"

AT: Das klingt so, als würde die MC Simulation ein analoges Signal erzeugen, was auch digitalisiert wird. Vllt kann man das nochmal nachforschen, aber zumindest in meiner Arbeit habe ich geschrieben, dass die MCPEs direkt in ATWD und fADC Readouts umgewandelt werden.

4.3.1 Trigger and Filter

Before the data can be sent to the North, the initial signal coming from the PMT (for data) or from the detector response simulation (for MC) is a voltage waveform, which has to be digitized and information of photon hits has to be extracted. The trigger and filter explained here are tailored to select events that passed through the DeepCore volume, while rejecting background events (either from atmospheric muons or from random noise). There are other filters used in IceCube which will not be explained here, since they are not relevant for this work. A full description of the instrumentation and the online systems can be found in [77].

[77]: Aartsen et al. (2017), "The IceCube Neutrino Observatory: Instrumentation and Online Systems"

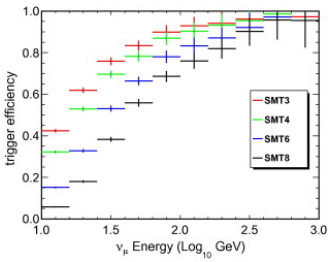

Figure 4.2: Efficiencies of different IceCube and DeepCore triggers, taken from [41].

In-ice Trigger

The trigger is applied inside the DOM in the ice before sending the information to the ICL on the surface. The time dependent voltage curves are

captured if a pre-defined threshold value is exceeded. Once the threshold set to the equivalent of 0.25 PE is crossed, 6.4 µs of the waveform are coarsely digitized by a *Fast Analog-to-Digital Converter (FADC)* with a sampling rate of 40 MHz. Additionally, the first 427 ns are digitized using an *Analog Transient Waveform Recorder (ATWD)* with a sampling rate of 300 MHz [37], but only if some trigger condition is met, because this readout frequency is too high to be sampled directly and requires some buffering. For DeepCore, the HLC condition already mentioned in Section 2.1.1 has to be met for three DOMs inside the fiducial volume within a time window of 5 µs. If this is the case, all waveforms that crossed the threshold within a 20 µs time window around the trigger are digitized and sent to the ICL for further processing. This trigger is called *Simple Multiplicity Trigger 3 (SMT-3)*. The DOM hits that are read out in this process, but do not meet the HLC condition, are called *soft local coincidence (SLC)* hits. The rate of the DeepCore SMT-3 trigger is ~250 Hz [34], accepting ~70 % of ν_μ-CC events at 10 GeV and ~90 % at 100 GeV [41]. The trigger efficiencies for different SMT triggers, including the DeepCore SMT-3, are shown in Figure 4.2.

[37]: Abbasi et al. (2009), "The IceCube data acquisition system: Signal capture, digitization, and timestamping"

[34]: Aartsen et al. (2017), "The IceCube Neutrino Observatory: instrumentation and online systems"

[41]: Abbasi et al. (2012), "The design and performance of IceCube DeepCore"

Online Filter

The digitized waveforms are sent to the ICL, where a further filter is applied *online*[2]. First, the WaveDeform algorithm is run to extract photon arrival times and charge from the waveforms, then the DeepCore filter is applied, which is an iterative hit cleaning starting from HLC hits and removing any hits outside a 125 m radius and a 500 ns time window (called *radius-time cleaning (RT-cleaning)*) of the initial hit. This mainly rejects unphysical SLC hits, which are potentially caused by random noise. The following selection steps are done using the resulting cleaned pulses.

2: Where *online* means running on hardware at the South Pole.

Next, an additional cut is applied to reject events that are likely to be caused by atmospheric muons. This is done by splitting the hits depending on whether they were inside the DeepCore fiducial volume or outside and then calculating the speed of each hit outside the fiducial volume towards the *center of gravity (COG)* of the hits inside. If one of them has a speed close to the speed of light, the whole event is rejected, because this is a strong indication for a muon event.

As input for the further selection levels, a few event properties, like vertex position and direction, are determined using fast and simple event reconstructions. After the DeepCore online filter, the rate is about 15 Hz, which can be sent to the North via satellite for further processing.

4.3.2 Event Selection

After the data was sent to the North, the *offline* filters and selection are applied to further recude reduce the background of atmospheric muons and noise. The selection is split into three levels referred to as *Level 3-5 (L3-L5)*, which bring down the neutrino and muon rate to ~1 mHz, while the remaining fraction of random noise is below 1 %.

Level 3

At the first offline filtering level, Level 3, 1D cuts are used to reduce atmospheric muons, pure noise, and coincident muons. These cuts are targeting regions where the data/MC agreement is poor, so that more sophisticated *machine learning (ML)* techniques can be applied at later levels. The cuts are made using 12 control variables, that are inexpensive to compute for the very large sample at this stage. The variables are related to position, time, and overall number of hits in the event.

Pure noise hits, that are temporally uncorrelated, are cleaned by applying a 300 ns sliding window, requiring the containment of more than 2 hits at its maximum. Additionally, an algorithm is run to check whether the hits show some directionality, accepting them only if they do.

To reduce the amount of muons a series of cuts is applied using spatial and temporal information. Events that have more than 9 hits observed above −200 m or the first HLC hit above −120 m are rejected as well as events where the fraction of hits in the first 600 ns of the event is above 0.37, ignoring the first two hit DOMs. Additionally, the ratio between hits in the veto region and the DeepCore fiducial volume is required to be below 1.5.

If a muon enters the detector after the data acquisition was already triggered, it causes events that span over a much larger time range. To reduce those coincident events, the time difference between first and last pulse cannot be above 5000 ns. This cut mainly affects a region of very poor data to MC agreement, because coincident events are not simulated at all.

The L3 cuts remove 95 % of the atmospheric muons and >99 % of pure noise hits, while keeping >60 % of the neutrino events. The sample now roughly contains muons/neutrinos/noise at a ratio of 100:10:1 with a total rate of ~0.5 Hz.

add example plots (2?) for L3 cut variables and applied cuts

Level 4

After the total rate was reduced by the simple cuts of L3 and the overall agreement between data and MC is established, ML techniques can be applied to further reduce the background. For Level 4, two *Boosted Decision Trees (BDTs)* [78] classifier are trained to separate neutrino events from atmospheric muons and noise hits, separately. The output of each classifier, a probability score, can be seen in Figure 4.3. The noise filter is applied first and an event passes the score if it is larger than 0.7, reducing the noise hits by a factor of 100, while keeping 96 % of neutrinos. Then the second BDT classifier is applied to reject muons. It was trained partly on unfiltered data, which consists of >99 % atmospheric muons, to reject the data and keeping the neutrinos from the simulation. Rejecting events with a score smaller than 0.65 removes 94 % of atmospheric muons while keeping 87 % of neutrinos. This fraction varies depending on the flavor and interaction type, ν_μ-CC events for example, which have a muon in the final state, are therefore reduced to 82.5 %. After applying the L4 cuts based on the BDT classifier outputs, the sample is still dominated by atmospheric muons, while the noise rate dropped to below most neutrino types.

[78]: Friedman (2002), "Stochastic gradient boosting"

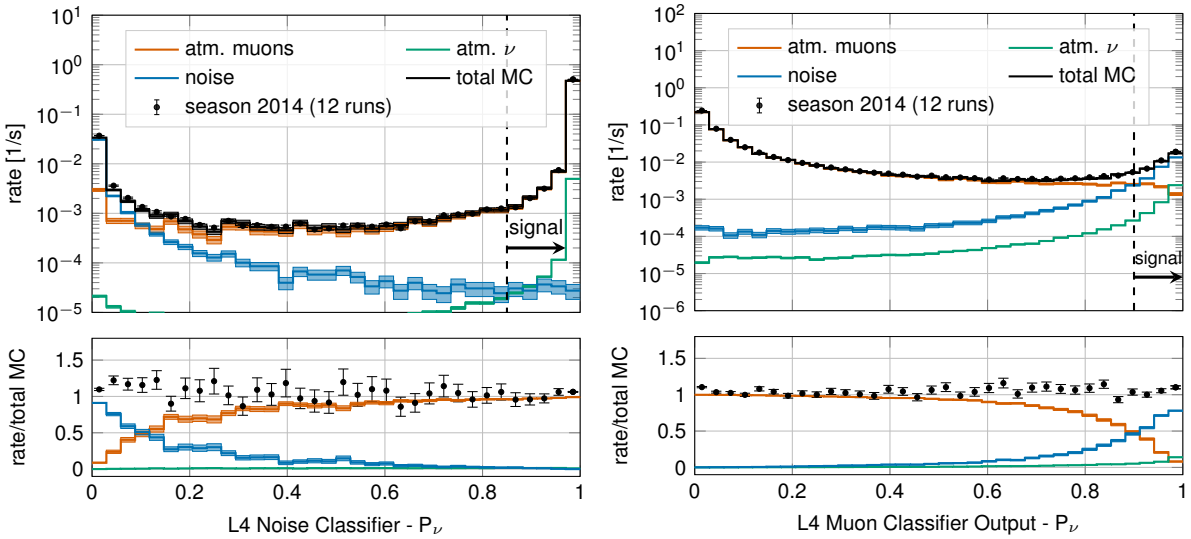

Figure 4.3: Distributions of Level 4 noise classifier output (left) and muon classifier output (right), where larger values indicate more neutrino-like and lower values more noise-like/muon-like. Taken from [57].

Level 5

Level 5 is the final selection level, before event reconstructions are applied. This level aims to reduce the remaining atmospheric muon rate below the rate of neutrinos. Muons not rejected by the earlier levels are those that produced little or no light in the veto regions. One possible reason is that they passed through one of the un-instrumented regions between the strings called *corridors*. To reject those, special corridor cuts, based on the number of hits they produced close to a potential corridor they passed through. The potential corridor in questions is identified based on a simple infinite track fit. In addition to the corridor cuts, starting containment cuts are applied to reject events that start at the edge of the fiducial volume. Events with more than seven hits in the outermost strings of the detector or those that have a down going direction in the uppermost region are rejected. This further reduces the fraction of muons by 96 % while keeping 48 % of neutrinos. The rates after this level are 1 mHz and 2 mHz for neutrinos and muons, respectively, making it a neutrino dominated sample.

add some figure showing the corridors?

add table with rates per level (split in flavor) - maybe better in analysis chapter to also show signal?

4.4 Reconstruction

In the energy range most relevant for this work, between 10 GeV and 100 GeV, the light deposition is very low and only a few DOMs detect light, making the reconstructions difficult. In [79] two classical methods are described, which have partly been applied in one recent IceCube atmospheric neutrino oscillation measurement using a sub-sample of the DeepCore sample [57]. The algorithm used in this work on the other hand, is a newer method that applies a *convolutional neural network (CNN)* to reconstruct the events and determine some discriminating quantities. The latest muon neutrino disappearance result from IceCube [80] is based on this reconstruction.

[79]: Abbasi et al. (2022), "Low energy event reconstruction in IceCube DeepCore"

[57]: Abbasi et al. (2023), "Measurement of atmospheric neutrino mixing with improved IceCube DeepCore calibration and data processing"

[80]: Yu et al. (2023), "Recent neutrino oscillation result with the IceCube experiment"

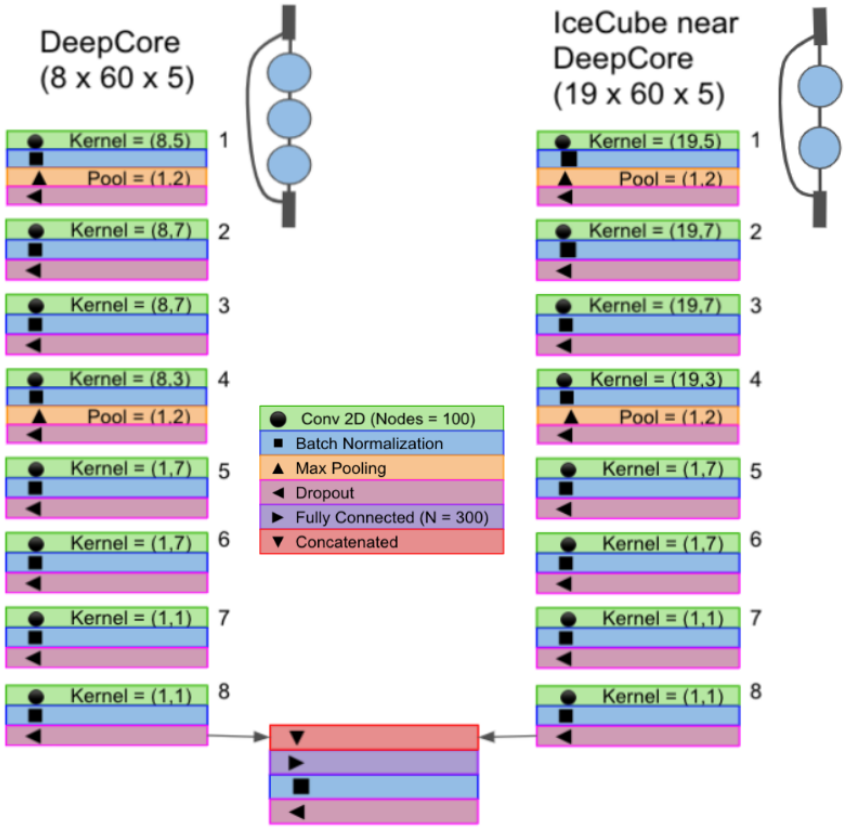

Figure 4.4: Architecture of the FLERCNN neural networks, taken from [81].

4.4.1 Fast Low Energy Reconstruction using Convolutional Neural Networks

As the name *Fast Low Energy Reconstruction using Convolutional Neural Networks (FLERCNN)* already indicates, the FLERCNN reconstruction [81, 82] is a CNN optimized to reconstruct IceCube events at low energies (<100 GeV) in a fast and efficient manner, by leveraging the approximate translational invariance of event patterns within the detector. The architecture of the network is very similar to the preexisting IceCube CNN event reconstruction [83], but optimized on low energy events and specifically tailored to include the DeepCore sub-array. Only the eight DeepCore strings and the central 19 IceCube strings are used for the reconstruction (compare to Figure 2.4). Because of the different z-positions of the DeepCore and IceCube DOMs, they are divided into two networks that are combined in the final layer of the network. The full architecture is shown in Figure 4.4. The first dimension of the network is the string index, while the second dimension is the order of the DOMs along the vertical axis. The horizontal position of the DOMs is not used, since the strings are arranged in an irregular pattern. The information from the DOM hits is summarized into five charge and time variables, which make up the last dimension of the input layer. The variables are the total summed charge, the time of the first hit, the charge weighted mean time of the hits, the time of the last hit, and the charge weighted standard deviation of the hit times.

[81]: Yu et al. (2021), "Direction reconstruction using a CNN for GeV-scale neutrinos in IceCube"
[82]: Micallef (),

[83]: Huennefeld (2017), "Deep Learning in Physics exemplified by the Reconstruction of Muon-Neutrino Events in IceCube"

add image with selected strings used for flercnn IC and DC

Five different networks are trained using this architecture. Three networks do the regression of the events' energy, zenith angle, and the starting vertex (x, y, z position), while two of them are used for classification. One is trained to predict the probability of the event being a track (used as PID) and the

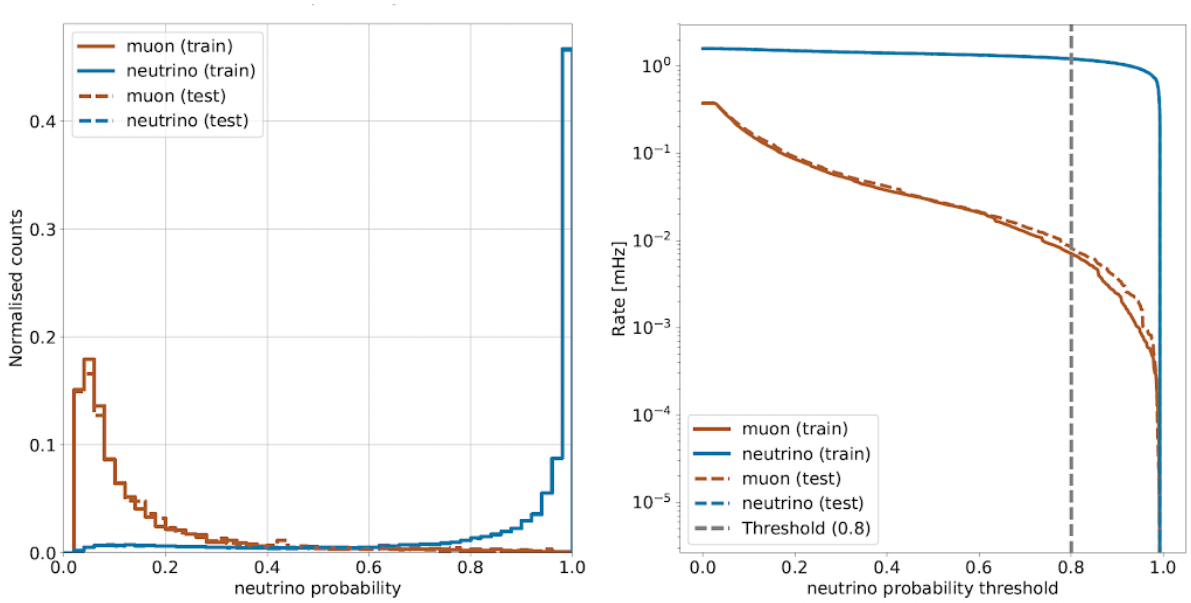

Figure 4.5: FLERCNN muon classifier output score (left) and rate of neutrinos and muons as function of muon classifier cut (right). Taken from **[flercnn_analysis_internal_note]**

other to predict the probability of the event being a muon. Each network is trained with an MC sample modified to have a flat distribution in the target variable, to be unbiased for that variable and ideally extending outside the target reconstruction region. For the classification tasks the loss function is the *binary cross entropy* and the activation function is a *sigmoid*. To perform the regression of zenith and vertex position, the loss function is the *mean squared error (MSE)*, while for the energy it is the *mean absolute percentage error*. The activation for all regression tasks is *linear*.

add some performance plots of the FLERCNN reconstruction

There is more information on pre-processing the samples and preparing the input features, and training each cnn, but I'm not sure if that might be too much detail?

4.4.2 Analysis Selection

Before the reconstruction is applied a few additional high level variables are computed, which are from fast and inexpensive algorithms. Then the reconstruction is performed by applying the trained FLERCNN networks to get the output quantities. After that, another BDT classifier is trained to further reduce the muon background for the final sample. The BDT is trained on five high level variables, where three are FLERCNN reconstruction variables (vertex z, ρ_{36}[3], and muon probability) and two are lower level variables (L4 muon classifier output and L5 corridor cut variable). To train the BDT, the FLERCNN nominal simulation set is used, only using events with $\cos(\theta_{zenith}) \leq 0.3$. The output of the BDT is the neutrino probability and a cut at 0.8 is applied to reject events with a high probability of being a muon. Figure 4.5 shows the output of the BDT classifier, where the neutrinos in both training and testing sets are gathered at 1 and muons are around 0, which shows great classification power.

3: A radial variable that is often used in IceCube, is the horizontal distance to string 36 called ρ_{36}, which is basically the distance to the center of IceCube.

add reference for flercnn analysis internal note

To get the final, pure sample of well reconstructed neutrinos another set of cuts is applied. The first cuts are meant to reject events with poor reconstruction quality, by requiring the events to fall into the DeepCore volume, where the denser, better instrumented detector leads to enhanced resolution. The cuts are applied on the vertex z and ρ_{36} and are listed in Table 4.3. The FLERCNN reconstruction was optimized for atmospheric

Variable	Threshold	Removed
Number of hit DOMs	≥ 7	1.05 %
Radial distance	$< 200\,\mathrm{m}$	0.09 %
Vertical position	$-495\,\mathrm{m} < z < -225\,\mathrm{m}$	5.48 %
Energy	$5\,\mathrm{GeV} < E < 100\,\mathrm{GeV}$	20.70 %
Cosine of zenith angle	< 0.04	19.66 %
Number of direct hits	> 2.5	10.50 %
Number of hits in top layers	< 0.5	0.03 %
Number of hits in outer layer	< 7.5	0.001 %
Muon classifier score	≥ 0.8	23.90 %

Table 4.3: Cuts performed to select the final analysis sample. Parts of the cuts are meant to increase the data/MC agreement, while others are meant to reject events with poor reconstruction quality.

neutrino analyses which are mainly in the region below 100 GeV and there are very few events with energies below 5 GeV, so the reconstructed energy is required to be in that range. Additionally, rejecting events with fewer than seven hits in the selected DOMs used for FLERCNN showed to increase the resolution.

Another set of cuts is applied to make sure the agreement between data and MC is good. To remove coincident muon and neutrino events, cuts are applied to the number of hits in the top 15 layers of IceCube DOMs and the number of hits in the outermost IceCube strings. Coincident random noise events are removed by requiring more than three hit DOMs from direct photons[4]. Neither of the two coincident event types are simulated, which can be seen as bad agreement between data and MC. The last cut is on the reconstructed cosine zenith, which is required to be smaller than 0.04 to reject down-going muons.

4: *Direct photons* are photons that were not scattered on their way from the interaction vertex to the DOM.

add final sample composition, but maybe also in analysis chapter to show signal and background?

at some place I will want a selection efficiency plot for SM BG and HNL signal, but I'm not sure where to put it yet

4.5 Systematic Uncertainties

There are multiple sources of systematic uncertainties related to the event generation and processing explained in this chapter. All uncertainties considered in this work are implemented with parameters that can be varied continuously so that a simultaneous fit of the physics and systematic parameters can be performed. Where possible, a correct model of the effect is used, but in many cases the variations are captured by effective parameters. Uncertainties that solely scale the total event rate are not included individually, since the analysis only uses the relative distribution of events and a single scaling parameter N_ν is used to scale the total neutrino rate instead.

4.5.1 Atmospheric Flux Uncertainties

The flux of atmospheric neutrinos is influenced by multiple factors, the spectrum and composition of CRs, the assumed atmospheric conditions, and the HI model used to describe the air showers development. Uncertainties of the neutrino flux are therefore dictated by the uncertainties on these components, where the variations in atmospheric conditions were found to have negligible effect [57].

[57]: Abbasi et al. (2023), "Measurement of atmospheric neutrino mixing with improved IceCube DeepCore calibration and data processing"

Cosmic ray flux: The selected sample of atmospheric neutrinos lies around energies of up to 100 GeV. The initial primary particles in the CR flux can have 100 times larger energies and therefore the CR flux between 10 GeV and 10 TeV is important, which dominantly consists of hydrogen and helium

nuclei [84]. The uncertainty in this CR flux component can be described as a power law correction [85, 86]

$$\Phi'_\nu = \Phi_\nu \left(\frac{E}{E^\star} \right)^{\Delta\gamma} , \tag{4.2}$$

where $E^\star$ is the pivot energy and $\Delta\gamma$ is the correction to the power law exponent. This modification propagates into the neutrino flux, which is therefore corrected in the same way. $E^\star$ was chosen to be 24 GeV as to minimize the dependence of the overall flux scale on $\Delta\gamma$ [57].

Hadronic interaction model: Neutrinos are produced in the decaying hadrons in CR air showers, spanning a large parameter space that is sparsely evaluated by experimental data. To include uncertainties based on energy, direction, and neutrino flavor, the MCEq package [87] is used to compute the distribution of atmospheric leptons and to estimate the impact of varying their contributions. The calculations result in the change in flux $d\Phi_l/dB$ for a variation dB of some parameter B. Scaling this variation by some value b, the modified total flux, s is then given by

$$\Phi'_l = \Phi_l + \left(b \cdot \frac{d\Phi_l}{dB} \right) . \tag{4.3}$$

Matching the work in [88], the parameter space is divided in regions of the primary energy E_i and the energy fraction of the secondary meson x_{lab}, with varying uncertainties, derived from fixed target experiment data. The Sibyll2.3c [89] HI model and the GSF CR flux [84] were used to calculate the related flux changes[5] for the different regions in E_i and x_{lab}, resulting in 17 variables, encoding the possible changes.

add figure with Barr blocks?

4.5.2 Cross-Section Uncertainties

The uncertainties related to the cross-sections are split into low and high energy components, since there is no coherent model to explain both DIS interactions, which are the dominant processes above 20 GeV, and *charged current resonance production (CCRES)* and *charged current quasi elastic scattering (CCQE)*, which are relevant below 20 GeV where interactions with the nucleons as a whole are important. Three parameters are included to account for all relevant cross-sections uncertainties.

At low energies two parameters are included accounting for uncertainties in form factors of CCQE and CCRES events. These uncertainties are due to uncertainties in the *axial mass* M_A, which enters the form factor as in

$$F(Q^2) \sim \frac{1}{(1 - (\frac{Q}{M_A})^2)^2} , \tag{4.4}$$

where Q^2 is the momentum transfer squared. The axial mass can be determined experimentally and to include uncertainties on the values of M_A^{CCQE} and M_A^{CCRES}, the cross-sections are computed with GENIE, where the form factors are calculated varying the axial mass by $\pm 20\%(1\sigma)/\pm 40\%(1\sigma)$ around the nominal value. This is an approximation of the recommended uncertainties by the GENIE collaboration, which are -15%, $+25\%$ for M_A^{CCQE} and

which experiments measure the axial mass?

[84]: Dembinski et al. (2017), "Data-driven model of the cosmic-ray flux and mass composition from 10 GeV to 10^{11} GeV"
[85]: Barr et al. (2006), "Uncertainties in atmospheric neutrino fluxes"
[86]: Evans et al. (2017), "Uncertainties in atmospheric muon-neutrino fluxes arising from cosmic-ray primaries"
[57]: Abbasi et al. (2023), "Measurement of atmospheric neutrino mixing with improved IceCube DeepCore calibration and data processing"
[88]: Barr et al. (2006), "Uncertainties in Atmospheric Neutrino Fluxes"
[89]: Riehn et al. (2020), "Hadronic interaction model sibyll 2.3d and extensive air showers"
[84]: Dembinski et al. (2017), "Data-driven model of the cosmic-ray flux and mass composition from 10 GeV to 10^{11} GeV"
5: The choice of flux and HI model have minor impact on the variations.

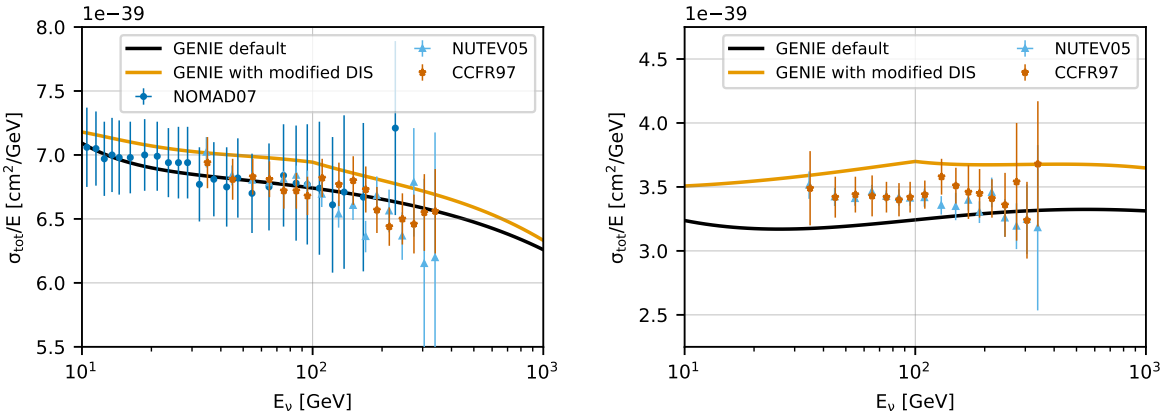

Figure 4.6: Inclusive total neutrino-nucleon cross-sections on an isoscalar target (black) for neutrinos (left) and antineutrinos (right) calculated with GENIE, comparing to measurements from NOMAD [91], NUTEV [92], and CCFR [93]. The scaled GENIE cross-section (orange) is also shown. Taken from [57].

±20% for M_A^{CCRES} [58]. To apply a continuous uncertainty variation of the axial mass in a fit, the total cross-section is fit with a quadratic function to interpolate between the cross-sections computed with the different axial masses.

Even though the DIS interactions can be calculated very precisely, there are still uncertainties in the input PDF, describing the probability of finding a specific parton (quark) with a specific momentum fraction x inside a nucleon. To account for differences between the used method and more sophisticated methods using newer PDFs seen at high energies, an uncertainty parameter is introduced. The parameter is based on the discrepancy between the cross-sections computed with GENIE and the ones computed with CSMS [90] above 100 GeV. The included parameter scales the cross-section from the GENIE values to the CSMS values, which are considered more accurate above 100 GeV. The scaling is done as a function of energy and inelasticity and to guarantee continuity, the scaling is extrapolated linearly below 100 GeV. The parameter is designed such that a value of 0.0 corresponds to the GENIE cross-sections and a value of 1.0 gives an approximation of the CSMS cross-sections. A comparison of the total cross-sections GENIE (scaled/unscaled) with the data is shown in Figure 4.6.

[90]: Cooper-Sarkar et al. (2011), "The high energy neutrino cross-section in the Standard Model and its uncertainty"

4.5.3 Detector Calibration Uncertainties

There are multiple sources of systematic uncertainties related to the detection process of neutrinos in IceCube. Dominant for this analysis are the effects of the properties of the ice itself and the optical efficiency of the DOMs. None of these uncertainties can be described by an analytic expression, so they have to be estimated using MC simulation. The method used to derive the continuous variations based on the MC simulation is described in Section 4.5.5. The five relevant uncertainty parameters are the absolute efficiency of the DOMs, a global scaling of bulk ice scattering and absorption lengths, and variations of the relative angular acceptance due to hole ice variations in two parameters.

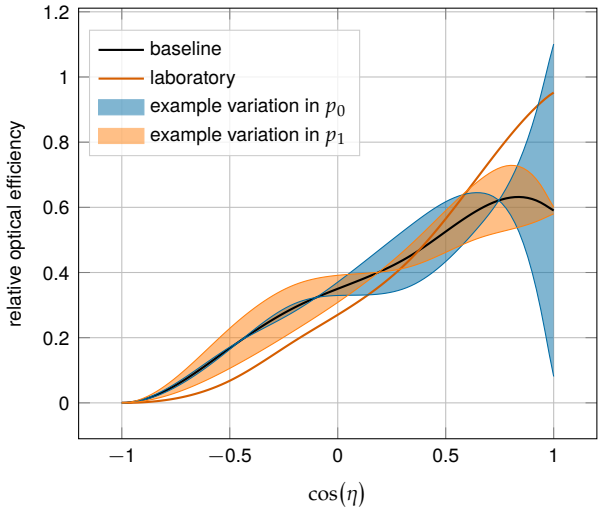

Figure 4.7: Relative angular acceptance modification due to hole ice. Shown is the current baseline model, the variations from changing p_0 and p_1, and a laboratory measurement. Modified from [69].

DOM efficiency: As was already mentioned in Section 2.1.1, the absolute efficiency of the DOMs, ϵ_{DOM} is calibrated using minimum ionizing muons from air showers, due to the lack of a calibrated light source in the detector. Using the muons as a steady, controlled source of light, the efficiency can be estimated by comparing simulated muon data sets with varied DOM response to the measured data. Since the uncertainties found in multiple iterations of this study [39, 40] are at the order of 10 %, this systematic is highly relevant and has to be included in the analysis.

[39]: Feintzeig (2014), "Searches for Point-like Sources of Astrophysical Neutrinos with the IceCube Neutrino Observatory"
[40]: Kulacz (2019), "In Situ Measurement of the IceCube DOM Efficiency Factor Using Atmospheric Minimum Ionizing Muons"

Bulk ice scattering and absorption: Absorption and scattering length are the most important properties that govern the propagation of photons through the ice. The simulation principle and how the depth dependent absorption and scattering coefficients are used was already explained in Section 4.2.1. To account for uncertainties on this model of the bulk ice coefficients, a global scaling for each of the two parameters (global absoprtion, global scatteriong) is applied.

Hole ice angular acceptance: Due to bubble formation in the re-freezing process of the boreholes, the hole ice seems to be less transparent in the center of the columns [94]. This effectively decreases the chance of photons hitting the DOMs directly from below, which can be described as an additional angular modification of the DOM acceptance. The modification is parameterized by a two dimensional, normalized[6] function, where the two dominant of the parameters (p_0, p_1), dictating its form, are enough to describe all past and the current hole ice models from both *in-situ* and laboratory measurements. Figure 4.7 shows the acceptance modification as a function of the incident photon angle $\cos(\eta)$. The current baseline model, the variations achieved through modifying p_0 and p_1, and a laboratory measurement can be seen.

[94]: Rongen, Martin (2016), "Measuring the optical properties of IceCube drill holes"

6: The hole ice angular acceptance modification is normalized so that it does not affect the total charge.

4.5.4 Muon Uncertainties

The muon fraction in the final level selection (see Section 4.4.2) is below 1 %, therefore additional muon systematic uncertainties apart from the spectral index are not implemented, but rather a total muon scaling parameter is

added. This total scale is somewhat degenerate with the DOM efficiency, since an increased DOM efficiency leads to better muon rejection. Both the total muon scaling and the muon spectral index have a very small impact on the analysis as will be shown in Section **??**.

cite this?

4.5.5 Treatment of Detector Response Uncertainties via a Likelihood-Free Inference Method

[95]

[95]: Fischer et al. (2023), "Treating detector systematics via a likelihood free inference method"

Copy paste from OVS PRD about hypersurfaces (and interpolation of those):

To evaluate the expected impact of detection uncertainties, data sets are produced with different variations of detector response, processed to the final level of selection, and then they are parameterized following a model of the uncertainties to evaluate how the final sample would look like for any reasonable choice of parameters. The parametrizations are done at the analysis bin level, assuming that every effect considered is independent and that they can be approximated by a linear function. Under these assumptions we can compute a reweighting factor in every bin that depends on N parameters, which correspond to the number of systematic effects being considered, plus an offset c, as

$$f(p_1, ..., p_N) = c + \sum_{n=1}^{N} m_n \Delta p_n. \tag{4.5}$$

Here m_n are the reweighting factors obtained from simulation sets with a systematic variation and Δp_n is the test value of a specific systematic variation.

The fit of the parameters m_n is done over all systematic MC sets, reducing the uncertainty on the MC prediction in each bin as a side effect since the error on the fitted function is smaller than the statistical error from the nominal MC set. The set of all fitted functions in all histogram bins are called "hypersurfaces". An example of such a fit from a single bin, projected onto one dimension, is shown in Fig. **??**.

The event counts coming from different flavors and interactions have a different response to varying the same detector parameter. Therefore, the hypersurfaces in each bin are fit separately for three groups of events:

- $(\nu_{\text{all}} + \bar{\nu}_{\text{all}})$ NC + $(\nu_e + \bar{\nu}_e)$ CC: These events all produce cascade signatures in the detector.
- $(\nu_\tau + \bar{\nu}_\tau)$ CC: These interactions may differ from the previous group because they have a production threshold of $E_\nu \gtrsim 3.5\,\text{GeV}$ and also produce muons with a branching ratio of 17%.
- $(\nu_\mu + \bar{\nu}_\mu)$ CC: These interactions produce track-like signatures.

The distribution of χ^2/d.o.f. from the fits in all analysis bins is used as a diagnostic to ensure that the fitted, linear hypersurfaces provide a good estimate for the expected number of events for the full range of simulated detector configurations. We find that the means of these χ^2/d.o.f. distributions are all consistent with 1.0 as expected from good fits for each of the three categories described above (NC + ν_e CC, ν_τ CC and ν_μ CC). Attempts

to use higher order polynomial fits did not yield a significantly improved χ^2/d.o.f., and in fact often rendered the fits less stable.

To produce the histograms for fitting the hypersurfaces, a choice must be made for the values of flux, cross-section and oscillation parameters. We found that the hypersurface fits are sensitive to the choice of parameters that have correlations with the effect they encode. Most notably, this effect is observed between the mass splitting and DOM optical efficiency as demonstrated in Fig. **??**, which shows the difference between fitted hypersurface gradients for the DOM efficiency dimension for two values of Δm^2_{32}.

This problem arises because we are only fitting the hypersurfaces in reconstructed phase space, without accounting for the different true energy and zenith distributions of MC in each analysis bin, which change with each detector systematic variation. To mitigate this problem, we fit the hypersurfaces for 20 different values in mass splitting between 1.5×10^{-3} eV^2 and 3.5×10^{-3} eV^2, and then apply a piece-wise linear interpolation to all slopes, intercepts and covariance matrix elements. The oscillation parameter fit can then dynamically adapt the hypersurfaces for each value of Δm^2_{32} that is tested using these interpolated functions. The effects of other parameter choices were evaluated as well, but none were found to introduce a significant bias.

Detecting Low Energetic Double Cascades

5

5.1 Reconstruction

All existing reconstruction algorithms applied for low energetic atmospheric neutrino events mentioned in Section 4.4 are either assuming a single cascade hypothesis or a track and cascade hypothesis, which are the two SM morphologies observable at these energies, as was described in Section 2.3. A HNL being produced and decaying inside the IceCube detector however, will produce two cascade like light depositions. The morphology and how the cascade properties and their spatial separation depend on the model parameters was introduced in Section 1.3.4. To investigate the performance of the detector to observe these events, a low energetic double cascade reconstruction algorithm was developed, based on a pre-existing algorithm used to search for double cascades produced from high energetic astrophysical tau neutrinos [96] that was established in [97], but first mentioned in [98].

[96]: Abbasi et al. (2020), "Measurement of Astrophysical Tau Neutrinos in IceCube's High-Energy Starting Events"
[97]: Usner (2018), "Search for Astrophysical Tau-Neutrinos in Six Years of High-Energy Starting Events in the IceCube Detector"
[98]: Hallen (2013), "On the Measurement of High-Energy Tau Neutrinos with IceCube"

5.1.1 Table-Based Minimum Likelihood Algorithms

The reconstruction is relying on a maximum likelihood algorithm, which is the *classical* approach to IceCube event reconstructions, as opposed to ML based methods. A Poissonian likelihood is constructed, which compares the observed photon numbers, n, with their arrival times to the expected light depositions, μ, for a given even hypothesis as

maybe I want a figure for this, or not so important?

$$\ln(L) = \sum_j \sum_t n_{j,t} \cdot \ln\big(\mu_{j,t}(\Theta) + \rho_{j,t}\big) - \big(\mu_{j,t}(\Theta) + \rho_{j,t}\big) - \ln\big(n_{j,t}!\big) \,, \quad (5.1)$$

where ρ are the number of expected photons from noise, Θ are the parameters governing the source hypothesis, and the likelihood is calculated summing over all DOMs j splitting observed photons into time bins t. The light expectations are calculated using look-up tables that contain the results from MC simulations of reference cascade events or track segments. By varying the parameters defining the event hypothesis, the likelihood of describing the observed light pattern by the expected light depositions is maximized to find the reconstructed event. Algorithms of this kind used in IceCube are described in great detail in [38]. For the table production a specific choice of ice model has to be made, while the calibrated DOM information is taken from the measurement itself.

cite photonics tables?

[38]: Aartsen et al. (2014), "Energy Reconstruction Methods in the IceCube Neutrino Telescope"

5.1.2 Double Cascade Hypothesis

Based on the tabulated light expectations for cascades and track segments, various event hypothesis can be constructed, like the common cascade only or the track and cascade hypotheses. The hypothesis describing the double cascade signature of the HNL is using two reference cascades that are separated by a certain distance. The whole hypothesis is defined by 9 parameters and assumes that the two cascades are aligned with each other,

Elaborate whether this is the case (show it in a plot?). Discuss directionality of cascades in general.

which is a safe assumption for strongly forward boosted interactions. The parameters are the position of the first cascade x, y, z, the direction of both cascades ϕ, θ, and its time t as well as the decay length L between the two cascades. Assuming the speed of the HNL to be the speed of light, c, this already defines the full signature. The HNL particle does not produce any light while traveling, as it is electrically neutral. The full 9 parameters describing the event are $\Theta = (x, y, z, t, \theta, \phi, E_0, E_1, L)$. To compute the full likelihood the term in Equation 5.1 is summed over both cascade parts, i, as $\sum_i \ln(L_i)$.

5.1.3 Optimization for Low Energy Events

Things to mention about the sample and the selection level where this optimization was done:

- Which simulation set was used for this?
- Which selection level was this run on?
- Which reco chain was run before running Taupede?
- Which seed was used as input for Taupede?

Decay Length Seeds

The full 9 dimensional likelihood space is very complex and can have many local minima, depending on the specific event and its location in the detector. Especially the seed value of the length between the two cascades was found to have a very strong impact on whether the global minimum was found during the minimization. To mitigate this effect, multiple fits are performed, seeding with variations of the input length at different orders of magnitude. The best result is used, selected based on the total likelihood value of the best fit parameter set. A small improvement in the decay length resolution can be found by using this approach as compared to a single length seed. The effect can be seen in the left part of Figure 5.1, which shows the median, absolute, fractional decay length resolution.

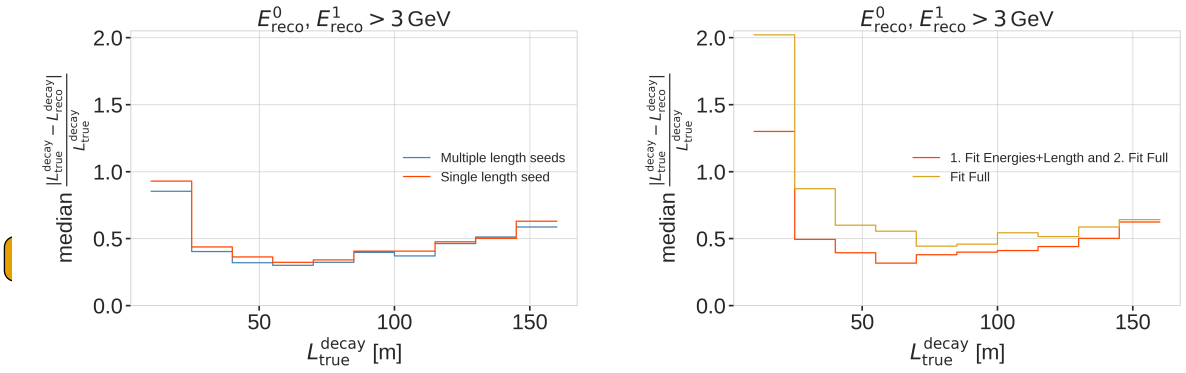

Figure 5.1

Fit Routine

Because the length seed showed to have such a large impact on the reconstruction performance, a more sophisticated fit routine, than just fitting all 9 parameters at once, was tested. In a first fit iteration, some parameters are fixed and the resulting best fit point is used to fit all 9 parameters in a second iteration. In the right part of Figure 5.1 it can be seen how a fit split into two consecutive steps, where the first step fits only both cascade energies and the decay length and the second step fits the full 9 parameters, performs better as compared to a single, full 9 parameter fit. The initial seed for both routines is the same.

Minimizer Settings: Unfortunately it was not possible to use more sophisticated minimization routines, circumventing the fitting to local minima, but the accessible minimizers within the Millipede framework were tested. In **??** the resulting resolutions from fits using three different minimizers are shown. The default Millipede minimizer Minuit1 Simplex seems to perform best out of these three.

Missing Points

- Taupede reconstruction chain
- MuMillipede "reconstruction"
- Flipped cascades (for events where the cascades changed order in time e.g. *negative decay lengths events*)
- badly reconstructed population and why this happened.

Add a table with fit runtimes and success rates?

The runtimes for these fit variations was also tracked alongside with the number of succesfull fits.

Chosen Reconstructions Chain/Settings Minuit1 Simplex 0.5x/1.0x/1.5x decay length seeding (multiplied by the Retro bf track length) iterative fit approach: 1. Fitting energies/decay length (3 seeds) 2. Full 9 parameter fit

5.2 Cross Checks

5.2.1 Simplistic Sets

After generation the events are processed with standard Photon, Detector, L1, and L2 processing and then Taupede+MuMillipede is run on top of the L2 files. Multiple versions with different parameters were produced, some with the OscNext baseline parameters, some without detector noise (in Det level) and some with h2-50cm holeice model, to match the holeice model that was used to generate the photonics tables.

BrightDom Cleaning To investigate the effect of the BrightDom cleaning cut the 194601 set without detector noise (and baseline hole ice model) is used. The BrightDom cleaning is needed to stop a few DOMs with many photon hits to drive the reconstruction because this leads to large biases in the energy estimations. Historically, the BrightDom cleaning was removing all DOMs that had a charge larger than 10 times the mean charge. After quickly checking some charge distributions and how the mean behaves it was clear that the cut should better be defined based on a metric that is less affected by outliers, like the median. Figure **??** shows where the mean and the median are located for an example event. The cut was re-defined to use the median instead of the mean and 10% of the simulation were processed with Taupede using 30x and 100x the median as BrightDom cutoff. Figure **??** shows where these values fall for the same example event.

As a quick check of the performance of both cuts the decay length resolution/bias and the resolutions/biases of all energies were checked. The reconstructed decay length is almost not affected by applying this cut, which is as expected, because it is mostly dependent on the arrival time of the photons. The effect on the reconstructed energy is much stronger, where a looser cut (100x) shows a significantly larger bias than the tighter cut at (30x). Even though this was not a highly sophisticated optimization of the BrightDom cut, an improvement was achieved by changing from mean to median and selecting the tighter cut (of the two tested). It's hard to tell how this would perform for high energy events, but I'm quite certain that a definition based on the median would be more reliable than on the mean.

5.3 Performance

5.3.1 Energy/Decay Length Resolution

describe the "good fit" selection

2-D Histograms

Things to mention about the 2d-hists:

- total energy resolution looks very good, above 10 GeV it's almost unbiased and the 1-sigma resolution band is below 20 %
- individual cascade resolutions mirror this behavior, but are starting to stabilize in energy at lower energies around 5 GeV to 6 GeV with a broader resolution band of 50 %, but reducing drastically with increasing energy (down to 20 % at 100 GeV)
- interestingly, the second cascade energy reconstruction performs slightly worse, although they have the same energy ranges. This could hint at an asymmetry in the reconstruction process (might relate to how the two cascades are parameterized) or be due to the different positions and the dominantly up-going direction used in the sampling combined with the DOMs looking down (relate this to the sampling distribuitons explained/shown in the previous chapter)
- the decay length resolution looks much worse. In the region between 20 m and 80 m it's roughly unbiased, but 1-sigma resolution band is quite wide with a lot of outliers towards short reconstructed lengths. Below 20 m the reconstructed lengths are always over-estimating the true and above 80 m a population of events start to dominate where the

decay lengths isn't getting reconstructed at all, which might indicate that one of the cascades wasn't observers. (Relate to the fact that this marginalizes over all energies, meaning also all events which have one cascade with very low energy are included here.)

- another interesting feature is the band of reconstructed lengths around 100 m, which is probabaly related to the spacing between most of the strings, which favors the reconstruction to be around this value, because that's the distance at which light can be observed, just from the fact that the DOMs are spaced at this distance (for low energetic cascades, this can dominate the reconstruction)

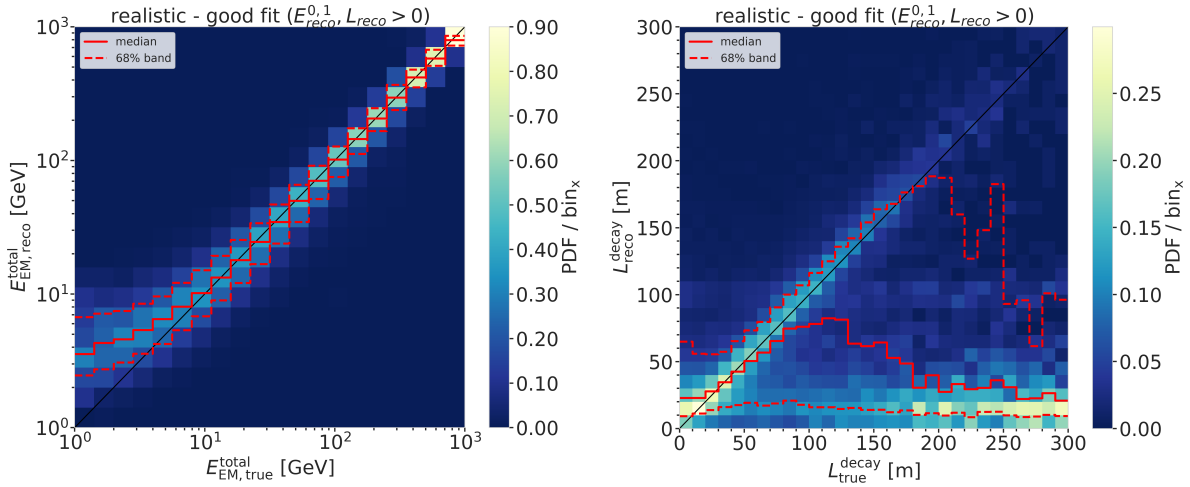

Figure 5.2

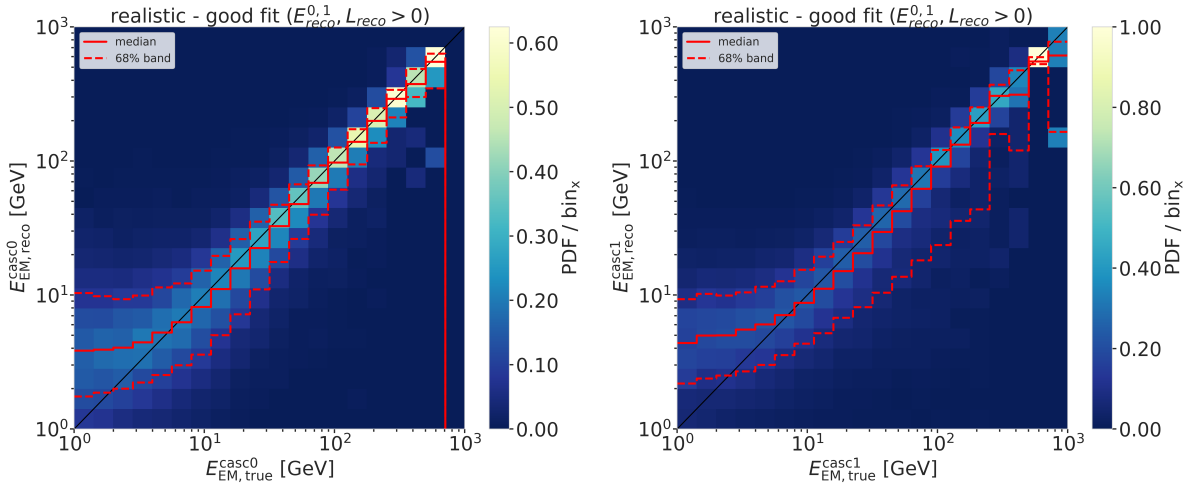

Figure 5.3

Energy Resolution

Things to mention about the energy resolution:

- Here it can be seen more clearly how the median total energy resolution starts to stabilize around 0.0 at 10 GeV, while for lower energies the reconstruction is over-estimating the true energy. This is a known behavior of energy reconstructions in IceCube, which is mainly due to

a selection effect. Only events with a certain amount of light can be reconstructed, which means that the ones with true small energies that are still in the sample are events with over average light production due to fluctuations or other effects?

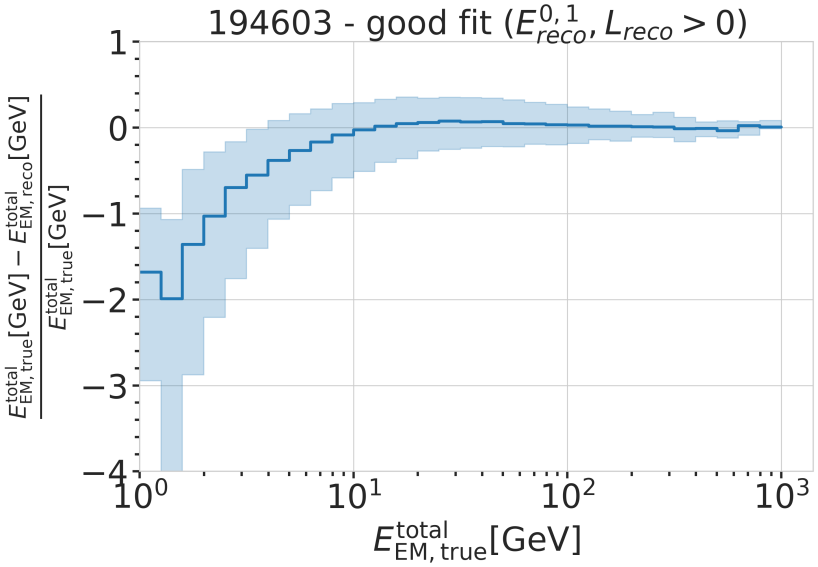

Figure 5.4

Decay Length Resolution

Things to mention about the decay length resolution:

- As already mentioned before, the decay length resolution is much worse than the energy resolutions. Figure 5.5 also shows that the median is below 0.0 for short true length and above 0.0 and approaching 1.0 for long true lengths.
- To investigate whether this is really due to the fact that one of the cascades is not observed, the decay length resolution was plotted against the total energy of the event and the minimum energy of the two cascades Figure 5.6.
- It can be seen that the median of the decay length resolution stabilizes at 0.0 for a total energy above 20 GeV, but the spread of the distribution is still quite large with a 1-sigma band of 80 % to 100 %.
- From the plot against the minimum energy it can be seen that the decay length resolution starts to be unbiased for a minimum energy of the cascades of 7 GeV, with an equivalently large spread.
- A preliminary takeaway from this is that the decay length reconstruction is not reliable at all for events with a total energy below 20 GeV or a minimum cascade energy below 7 GeV.

5.3.2 Double Cascade Classification

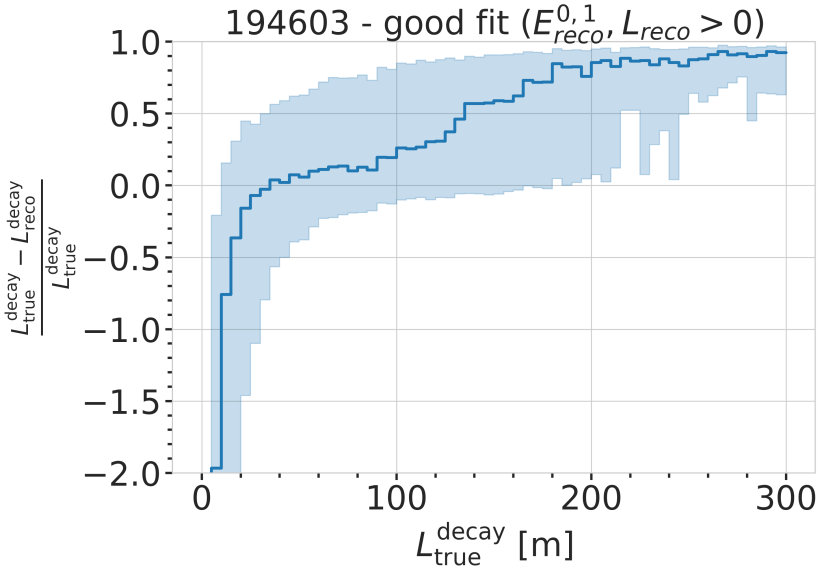

Figure 5.5

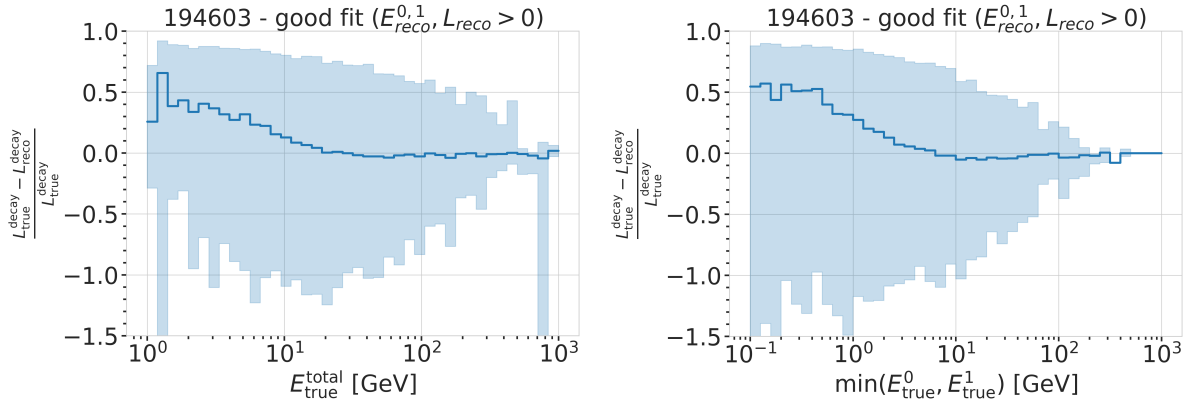

Figure 5.6

5.4 Low Energy Event Selection Efficiency

Make plot to show efficiency of the OscNext selection for HNL events.

Discussion ideas:

- At which level does the selection reduce the HNL the most?
- Is there a place to improve the HNL selection? (Might have to factor in the BG efficiency, as well..)
- What of this might change with Upgrade? (maybe rather for the discussion)

Search for an Excess of Heavy Neutral Lepton Events

6

The measurement performed in this thesis is the search for an excess of HNL events in the 10 years of IceCube DeepCore data. In principle the two physics parameters to be probed are the mass of the HNL, m_4, and the mixing between the fourth heavy mass state and the SM τ sector, $|U_{\tau 4}|^2$. Since the mass itself influences the production and decay kinematics of the event and the accessible decay modes, individual mass samples were produced as described in Section 3.2. IceCube DeepCore is suited to measure the excess which appears around and below 20 GeV, due to its production from the atmospheric tau neutrinos, although a reduced lower energy threshold might improve the analysis. The measurement will be performed for the three mass samples individually, while the mixing is the parameter that can be varied continuously and will be measured in the fit.

6.1 Final Level Sample

The final level sample of this analysis always consists of the neutrino and muon MC introduced in Section 4.1 and one of the three HNL samples explained in Section 3.2. All of those simulation sets and the 10 years of IceCube DeepCore data are processed through the full processing and event selection chain described in Section 4.3 and Section 4.4 leading to the final level sample. Since applying the final cuts from Section 4.4.2 leaves an insignificant amount of pure noise events in the sample, the noise simulation is not included in the analysis and will not be listed here.

add information about the matter profile used

add information about the oscillation probability calculation and the software used for it

6.1.1 Expected Rates/Events

The rates and the expected number of events for the SM background are shown in Table 6.1 with around 175000 total events expected in the 10 years. The explicit, good detector livetime in this data taking period is 9.28 years. The rates are calculated by summing the weights of all events in the final level sample, while the uncertainties are calculated by taking the square root of the sum of the weights squared. The expected number of events is calculated by multiplying the rate with the livetime. The individual fractions show that this sample is neutrino dominated where the majority of events are ν_μ-CC events.

Type	**Rate** [mHz]	**Events (in** 9.28 years**)**	**Fraction** [%]
ν_μ^{CC}	0.3531	103321 ± 113	58.9
ν_e^{CC}	0.1418	41490 ± 69	23.7
ν_{NC}	0.0666	19491 ± 47	11.1
ν_τ^{CC}	0.0345	10094 ± 22	5.8
μ	0.0032	936 ± 15	0.5
total	0.5991	175336 ± 143	100.0

Table 6.1: Final level rates and event expectation of the SM background particle types.

Should I adapt the total numbers to match the sum of the rounded individual parts?

Table 6.2 shows the rates and expected number of events for the HNL signal simulation. The expectation depends on the mass and the mixing and shown

here are two example mixings for all the three masses that are being tested in this work. A mixing of 0.0 would result in no HNL events at all. It can already be seen that for the smaller mixing of $|U_{\tau 4}|^2 = 10^{-3}$ the expected number of events is very low, while at the larger mixing of $|U_{\tau 4}|^2 = 10^{-1}$ the number is comparable to the amount of muons in the background sample.

Table 6.2: Final level rates and event expectations of the HNL signal for all three masses and two example mixing values.

HNL mass	**Rate** [μHz]	**Events (in** 9.28 years**)**
$\|U_{\tau 4}\|^2 = 10^{-1}$		
0.3 GeV	3.3298 ± 0.0053	974.5 ± 1.6
0.6 GeV	3.0583 ± 0.0058	895.0 ± 1.7
1.0 GeV	2.4988 ± 0.0059	731.3 ± 1.7
$\|U_{\tau 4}\|^2 = 10^{-3}$		
0.3 GeV	0.0057	1.67 ± 0.01
0.6 GeV	0.0220	6.44 ± 0.01
1.0 GeV	0.0248	7.27 ± 0.01

6.1.2 Analysis Binning

[80]: Yu et al. (2023), "Recent neutrino oscillation result with the IceCube experiment"

The identical binning to the analysis performed in [80] is used. It was chosen such that the track-like bin has the largest ν_μ-CC fraction. Extending the binning towards lower energies or increasing the number of bins in energy or cosine of the zenith angle did not improve the HNL sensitivities significantly. It also has to be considered that sufficient data events need to end up in the individual bins to result in a good fit, which was already investigated in the previous analysis. To mitigate the low data statistics, a few bins were not taken into account in the analysis. There are three bins in PID (cascade-like, mixed, and track-like), 12 bins in reconstructed energy, and 8 bins in cosine of the reconstructed zenith angle as specified in Table 6.3. Originally, there were two more bins in $\cos(\theta)$, which were removed to reduce muons coming from the horizon and some low energy bins in the cascade-like bin are removed due to the low event statistics.

Table 6.3: Three dimensional binning used in the analysis. All variables are from the PLERCNN reconstruction. Variable definitions can be found in Section 4.4.

Variable	N_{bins}	**Edges**	**Step**
P_ν	3	[0.00, 0.25, 0.55, 1.00]	linear
E	12	[5.00, 100.00]	logarithmic
$\cos(\theta)$	8	[-1.00, 0.04]	linear

add 3D expectation and/or S/sqrt(B) plots

Add fractions of the different particle types in the bins for benchmark mass/mixing (another table?)

6.2 Statistical Analysis

6.2.1 Low Energy Analysis Framework

[99]: Aartsen et al. (2020), "Computational techniques for the analysis of small signals in high-statistics neutrino oscillation experiments"

Do I want more information about the different pipelines and stages? Could link back to the extra stage I wrote and add the earth model and oscillation calculation information here, I guess?!

The analysis is performed using the PISA [99] [56] software framework, which was developed to perform analyses "of small signals in high-statistics neutrino oscillation experiments". It is used to generate the expected event distributions from several MC samples, which can then be compared to the observed data. The expectation for each sample is calculated in parallel, applying physics and nuisance parameter effects in a stage-wise manner, before combining the final expectation from all the samples.

6.2.2 Test Statistic

I feel like I have to be a bit more precise on what is the fit metric (e.g. the mod chi2) and what is the TS, as in the mod chi2 difference, which is the actual TS, right?

The measurements are performed by comparing the weighted MC to the data. Through variation of the nuisance and physics parameters that govern the weights, the best matching set of parameters can be found. The comparison is done using a modified χ^2 defined as

$$\chi^2_{\text{mod}} = \sum_{i \in \text{bins}} \frac{(N_i^{\text{exp}} - N_i^{\text{obs}})^2}{N_i^{\text{exp}} + (\sigma_i^{\nu})^2 + (\sigma_i^{\mu})^2 + (\sigma_i^{\text{HNL}})^2} + \sum_{j \in \text{syst}} \frac{(s_j - \hat{s_j})^2}{\sigma^2_{s_j}}, \quad (6.1)$$

as the *test statistic (TS)*. The total even expectation is $N_i^{\text{exp}} = N_i^{\nu} + N_i^{\mu} + N_i^{\text{HNL}}$, where N_i^{ν}, N_i^{μ}, and N_i^{HNL} are the expected number of events in bin i from neutrinos, atmospheric muons, and HNLs, while N_i^{obs} is the observed number of events in bin i. The expected number of events from each particle type is calculated by summing the weights of all events in the bin $N_i^{\text{type}} = \sum_i^{\text{type}} \omega_i$, with the statistical uncertainty being $(\sigma_i^{\text{type}})^2 = \sum_i^{\text{type}} \omega_i^2$. The additional term in Equation 6.1 is included to apply a penalty term for prior knowledge of the systematic uncertainties of the parameters where they are known. s_j are the systematic parameters that are varied in the fit, while $\hat{s_j}$ are their nominal values and σ_{s_j} are the known uncertainties.

Do I want/need to include the description of the KDE muon estimation?

6.2.3 Physics Parameters

The variable physics parameter in this analysis is the mixing between the HNL and the SM τ sector, $|U_{\tau 4}|^2$. It can be changed continuously in the range of [0.0 , 1.0] by applying the weighting scheme described in Section 3.2.3. The fit is initialized at an off-nominal value of 0.1 The other physics parameter, the mass m_4 of the HNL, is fixed to one of the three discrete masses to be tested, by using the corresponding sample of the HNL simulation described in Section 3.2.

6.2.4 Nuisance Parameters

To decide which systematic uncertainties should be included in the fit, we test the potential impact they have on the TS if they are neglected. The test is performed by creating Asimov data using the 1.0 GeV sample at a mixing value of 0.1, which is around the value where the analysis starts to become sensitive. The systematic parameter of interest is set to a value above its nominal expectation, either pulled up by $+1\sigma$ or by an educated estimate for parameters without a well-defined uncertainty. A fit is performed fixing the systematic parameter of interesting and leaving all additional parameters free. The resulting TS is the mis-modeling significance between this fit and a fit with all parameters free, which would result in a TS of 0.0 for this Asimov test. Parameters below a significance of 0.1 σ are fixed and the test is perfomed in an iterative manner until the final set of free parameters is found. Figure 6.1 shows the resulting significances of one of these tests. In the final selection of free parameters the Barr h_{π^+} parameter was also left free and the ice absorption is still kept free, despite showing a small significance. This is done because the bulk ice parameters are not well constrained and are known to have a large impact, which might be concealed in the test, due to correlations with the other parameters.

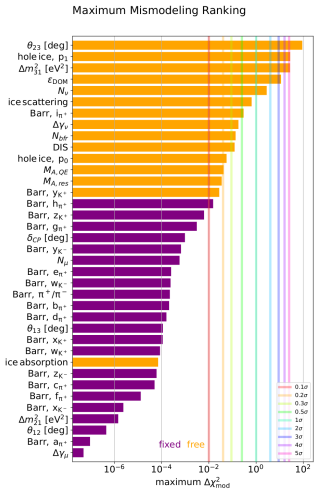

Figure 6.1: "calculated at a mixing of 0.1 and for the 1.0 GeV sample"

Blow up labels/legend/title and make it more readable in the margin

I don't like this formulation, but don't know better right now..

elaborate why this is also done to cover the whole energy range for the pion production, referencing the Barr Block plot that I haven't included yet :D

I truly dislike this sentence, too, better ideas?

Table 6.4: Systematic uncertainty parameters that are left free to float in the fit. Their allowed fit ranges are shown with the nominal value and the Gaussian prior width if applicable.

Parameter	Nominal	Range	Prior
$\Delta\gamma_\nu$	0.0	[-0.5, 0.5]	0.1
Barr h_{π^+}	0.0	[-0.75, 0.75]	0.15
Barr i_{π^+}	0.0	[-3.05, 3.05]	0.61
Barr y_{K^+}	0.0	[-1.5, 1.5]	0.3
$\theta_{23}[^\circ]$	47.5047	[0.0, 90.0]	-
$\Delta m^2_{31}[\mathrm{eV}^2]$	0.002475	[0.001, 0.004]	-
DIS	0.0	[-0.5, 1.5]	1.0
N_ν	1.0	[0.1, 2.0]	-
ϵ_{DOM}	1.0	[0.8, 1.2]	0.1
hole ice p_0	0.101569	[-0.6, 0.5]	-
hole ice p_1	-0.049344	[-0.2, 0.2]	-
bulk ice absorption	1.0	[0.85, 1.15]	-
bulk ice scattering	1.05	[0.9, 1.2]	-
N_{bfr}	0.0	[-0.2, 1.2]	-
$M_{\mathrm{A,QE}}$	0.0	[-2.0, 2.0]	1.0
$M_{\mathrm{A,res}}$	0.0	[-2.0, 2.0]	1.0

I'm just writing out the data from the table, but I need to mention/motivate the included priors here and maybe just point to the table for the ranges/nominal values? (Not quite sure about this)

The scaling parameter N_ν is included to account for the unknown overall normalization of the neutrino rate. It has the identical effect on the SM neutrino events and the BSM HNL events and its nominal value is set to 1.0 with a wide range of [0.1, 2.0].

Concerning the atmospheric neutrino flux, the CR power law flux correction factor $\Delta\gamma_\nu$ is included with nominal value of 0.0 and a range of $[-0.5, 0.5]$. The nominal value corresponds to a CR power law of E^{-2} and a slightly conservative prior of 0.1 is applied to the parameter, while latest measurements have an uncertainty of 0.05 [86].

[86]: Evans et al. (2017), "Uncertainties in atmospheric muon-neutrino fluxes arising from cosmic-ray primaries"

say something about their priors

Additionally, the Barr h_{π^+}, Barr i_{π^+}, and Barr y_{K^+} parameters of the pion and kaon production uncertainties are included with nominal values of 0.0 and ranges of $[-0.75, 0.75]$, $[-3.05, 3.05]$, and $[-1.5, 1.5]$, respectively.

say something about their priors

From the cross-section uncertainties introduced in Section 4.5.2, all three parameters, DIS, $M_{\mathrm{A,QE}}$, and $M_{\mathrm{A,res}}$ are included in the fit with nominal values of 0.0 for all of them and range $[-0.5, 1.5]$ for DIS and $[-2.0, 2.0]$ for the axial mass parameters $M_{\mathrm{A,QE}}$, and $M_{\mathrm{A,res}}$.

[39]: Feintzeig (2014), "Searches for Point-like Sources of Astrophysical Neutrinos with the IceCube Neutrino Observatory"
[40]: Kulacz (2019), "In Situ Measurement of the IceCube DOM Efficiency Factor Using Atmospheric Minimum Ionizing Muons"

cite?!

All the detector systematic uncertainties are included in the fit. The DOM efficiency ϵ_{DOM} has a nominal value of 1.0 and a range of [0.8, 1.2]. It is constrained by a Gaussian prior with a width of 0.1, which is a conservative estimate based on the studies of the optical efficiency using minimum ionizing muons from [39, 40]. The hole ice model parameters p_0 and p_1 are included with nominal values of 0.101569 and -0.049344, respectively, and ranges of $[-0.6, 0.5]$ and $[-0.2, 0.2]$. The bulk ice absorption and scattering parameters are included with nominal values of 1.0 and 1.05, respectively, and ranges of [0.85, 1.15] and [0.9, 1.2]. They are unconstrained in the fit and the ranges are set to be conservative determined from calibration data

I think I will need to mention here that I did no inlcude MA-RES and MA-QE for the HNL simulation..

The two atmospheric neutrino oscillation parameters θ_{23} and Δm^2_{31} are also included in the fit with nominal values of 47.5047° and $2.475 \times 10^{-3}\,\mathrm{eV}^2$, respectively. Since they govern the shape and the strength of the tau neutrino flux, by defining the oscillation from ν_μ to ν_τ, they are also relevant for the HNL signal shape. Their ranges are set to $[0.0^\circ, 90.0^\circ]$ and $[0.001\,\mathrm{eV}^2, 0.004\,\mathrm{eV}^2]$.

add final level effects of varying the axial mass parameters (or example of one)

6.3 Analysis Checks

add final level effects of varying the DIS parameter (or example of one)

Fitting to data will be performed in a *blind* manner, where the analyzer does not immediately see the fitted physics and nuisance parameter values, but first checks that a set of pre-defined *goodness of fit (GOF)* criteria are fulfilled. At this point changes to the analysis can still be made, if the criteria are not met. This is done to circumvent the so-called *confirmation bias* [100], where the analyzer might be tempted to construct the analysis in a way that confirms their expectation. After the GOF criteria are met to satisfaction, the fit results are unblinded and the full result can be revealed. Before these blind fits to data are performed, the robustness of the analysis method is tested using pseudo-data that is generated from the MC.

[100]: Nickerson (1998), "Confirmation Bias: A Ubiquitous Phenomenon in Many Guises"

6.3.1 Minimization Robustness

To find the set of parameters that describes the data best, a staged minimization routine is used. In the first stage, a fit with coarse minimizer settings is performed to find a rough estimate of the *best fit point (BFP)*. In the second stage, the fit is performed again in both octants[1] of θ_{23}, starting from the BFP of the coarse fit. For each individual fit the *MIGRAD* routine of IMINUIT [101] is used to minimize the χ^2_{mod} TS defined in Equation 6.1. Iminuit is a fast, python compatible minimizer based on the MINUIT2 C++ library [102]. The individual minimizer settings for both stages are shown in Table 6.5.

1: There is a degeneracy between the lower octant ($\theta_{23} < 45°$) and the upper octant ($\theta_{23} > 45°$), which can lead to TS minima (local and global) at two positions that are mirrored around 45° in θ_{23}.

[101]: Dembinski et al. (2022), *scikit-hep/iminuit: v2.17.0*

again, I think fit metric and TS are mixed up a bit

To test the minimization routine and to make sure it consistently recovers any injected physics parameters, pseudo-data sets are produced from the MC by choosing the nominal nuisance parameters and specific physics parameters, without adding any statistical or systematic fluctuations to it. These so-called *Asimov*[2] data sets are then fit back with the full analysis chain. This type of test is called *Asimov inject/recover test*. A set of mixing values between 10^{-3} and 10^{0} is injected and fit back. Even though this range is well within the excluded regions by other experiments, discussed in Section 1.2.3, this covers the current sensitive region of the analysis in IceCube DeepCore. Without fluctuations the fit is expected to always recover the injected parameters (both physics and nuisance parameters). The fitted mixing values from the Asimov inject/recover tests are compared to the true injected values in Figure 6.2 for the 0.6 GeV sample. As expected, the fit is always able to recover the injected physcis parameter and the nuisance paramters. The same is true for the other mass samples and the additional plots for the other mass samples can be found in Section B.1.

[102]: James et al. (1975), "Minuit: A System for Function Minimization and Analysis of the Parameter Errors and Correlations"

Fit	Err.	Prec.	Tol.
Coarse	1e-1	1e-8	1e-1
Fine	1e-5	1e-14	1e-5

Table 6.5: Migrad settings for the two stages in the minimization routine. *Err.* are the step size for the numerical gradient estimation, *Prec.* is the precision with which the LLH is calculated, and *Tol.* is the tolerance for the minimization.

6.3.2 Goodness of Fit

2: A pseudo-data set without statistical fluctuations is called Asimov data set.

Do I want additional plots for this (fit diff, LLH distr, minim. stats, param. fits)?

To estimate the GOF, pseudo-data is generated from the MC by injecting the BFP parameters as true parameters and then fluctuating the expected bin counts to account for MC uncertainty and Poisson fluctuations in data. First, the expectation value of each bin is drawn from a Gaussian distribution centered at the nominal expectation value with a standard deviation corresponding to the MC uncertainty of the bin. Based on this sampled expectation value, each bin count is drawn from a Poisson distribution, independently, to get the final pseudo-data set. These pseudo-data sets are then fit back with the analysis chain. By comparing the distribution of TS

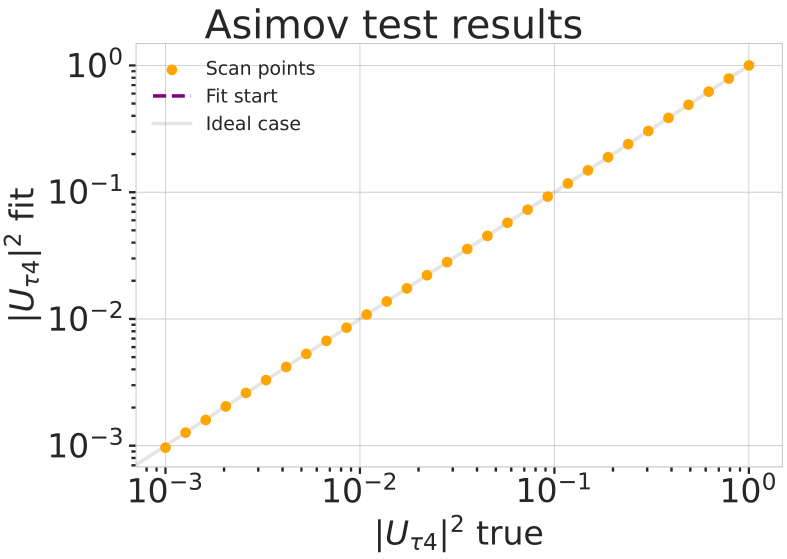

Figure 6.2: Asimov inject/recover test for the 0.6 GeV mass sample. Mixing values between 10^{-3} and 10^{0} are injected and fit back with the full analysis chain. The injected parameter is always recovered within the statistical uncertainty.

here again, this is just the fit metric, right?

Add bin-wise TS distribution? Add 3D TS maps?

values from this *ensemble* of pseudo-data trials to the TS of the fit to real data, a p-value can be calculated. The p-value is the probability of finding a TS value at least as large as the one from the data fit. Figure 6.3 shows the TS distribution from the ensemble tests for the 0.6 GeV mass sample and the observed TS value from the fit, resulting in a p-value of 28.5 %. The p-values for the 0.3 GeV and 1.0 GeV are 28.3 % and 26.0 %, respectively and the correspoinding plots are shown in Section B.1.1. Based on this test, it is concluded that the fit result is compatible with the expectation from the ensemble of pseudo-data trials.

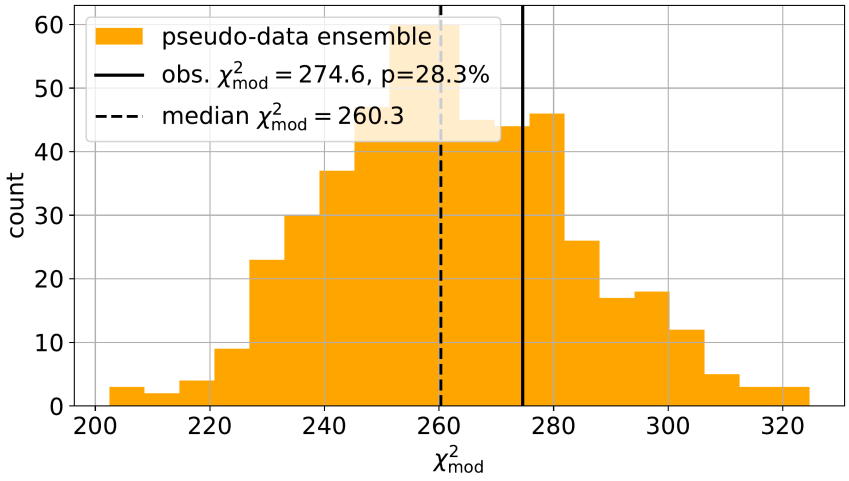

Figure 6.3: Observed fit TS and TS distribution from pseudo-data trials for the 0.6 GeV mass sample.

6.4 Results

6.4.1 Best Fit Nuisance Parameters

The resulting nuisance parameter values from the fits are illustrated in Figure 6.4, where the differences to the nominal values are shown, normalized by the distance to the closest boundary. The results from all three fits are shown in the same plot and the fits prefer values of the same size for all

three mass samples. For parameters that had a Gaussian prior, the 1 σ range is also displayed. As was already confirmed during the blind fit procedure, all fitted parameters are within this range, but the Barr h_{π^+} parameter is smaller and the Barr i_{π^+} is larger than expected, both being very close within the +1 σ and the −1 σ range, respectively. The DIS parameter fits to a smaller value than the nominal and all ice parameters, both hole ice p_0, and p_1 as well as bulk ice absorption, and scattering are found at values lower than the nominal. The effective ice model parameter, N_{bfr}, prefers a value of ~0.74 , indicating that the data is more *BFR*-like (value of 1.0) than *Spice 3.2.1*-like (value of 0.0). For completeness's sake, the explicit results are listed in Table C.1. There, the nominal values and the absolute differences to the best fit value are also presented.

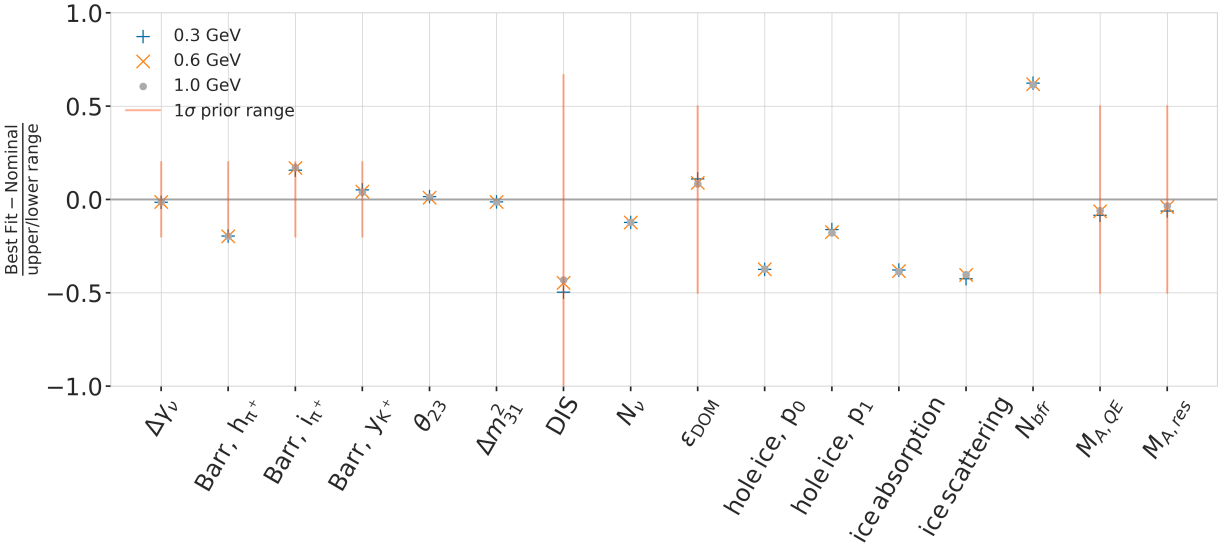

Figure 6.4: Best fit nuisance parameter distances to the nominal values, normalized by the distance to the closest boundary. For parameters with a Gaussian prior, the +1 σ range is also shown.

sort the variables also by type, same as in the table "best_fit_parameters"?

Show best fit hole ice angular acceptance compared to nominal and flasher/in-situ fits, maybe?

Discuss what it means that the parameters are at these values? Here, or somewhere else?

6.4.2 Best Fit Parameters and Limits

The fitted mixing values are

$$|U_{\tau 4}|^2_{\text{BFP}}(0.3\,\text{GeV}) = 0.003^{+0.084}\,,$$
$$|U_{\tau 4}|^2_{\text{BFP}}(0.6\,\text{GeV}) = 0.080^{+0.134}\,,\text{and}$$
$$|U_{\tau 4}|^2_{\text{BFP}}(1.0\,\text{GeV}) = 0.106^{+0.132}\,,$$

with their +1 σ uncertainty. All of them are compatible with the null hypothesis of 0.0 mixing, although the 0.6 GeV and 1.0 GeV fits indicate a mixing value around 0.09 The best fit mixing values and the corresponding upper limits at 68 % and 90 % *confidence level (CL)* are listed in Table 6.6, also showing the CL at the null hypothesis, which is the probability of excluding the null hypothesis with this fit. The CLs are estimated by assuming that *Wilks' theorem* [103] holds, meaning that the TS follows a χ^2 distribution with one degree of freedom.

[103]: Wilks (1938), "The Large-Sample Distribution of the Likelihood Ratio for Testing Composite Hypotheses"

Figure 6.5 shows the observed likelihood profile for the 0.6 GeV sample, which is the difference in χ^2_{mod} between the best fit and each scan point in $|U_{\tau 4}|^2$. Also shown is the expected likelihood profile, based on a scan over

fix table caption

Table 6.6: xx

HNL mass	$\lvert U_{\tau 4}\rvert^2_{\text{BFP}}$	68 % CL	90 % CL	$\text{CL}_{\text{null hypo}}$
0.3 GeV	0.003	0.087	0.194	0.03 %
0.6 GeV	0.080	0.214	0.355	21.29 %
1.0 GeV	0.106	0.238	0.396	37.25 %

fix once I have them produced

fix once I have the brazil bands

Asimov data produced at the BFP. The observed CLs are slightly larger/smaller than the expected CL. To ensure this is compatible with random fluctuations, the expected likelihood is also profiled for 100 pseudo-data sets, which are generated at the BFP and then fluctuated using both Poisson and Gaussian fluctuations, to include the data and the MC uncertainty, as was already done for the ensemble tests. The resulting CLs are shown as the colored areas and the observed contour is well within the 68 % band, confirming that it is compatible with data fluctuations. Figure C.1 shows the same likelihood profiles and bands for the other two mass samples. For both of them the observed CLs are also slightly larger/smaller than the expected, but still within the 68 % band of the pseudo-data trials, so they are also compatible with random fluctuations.

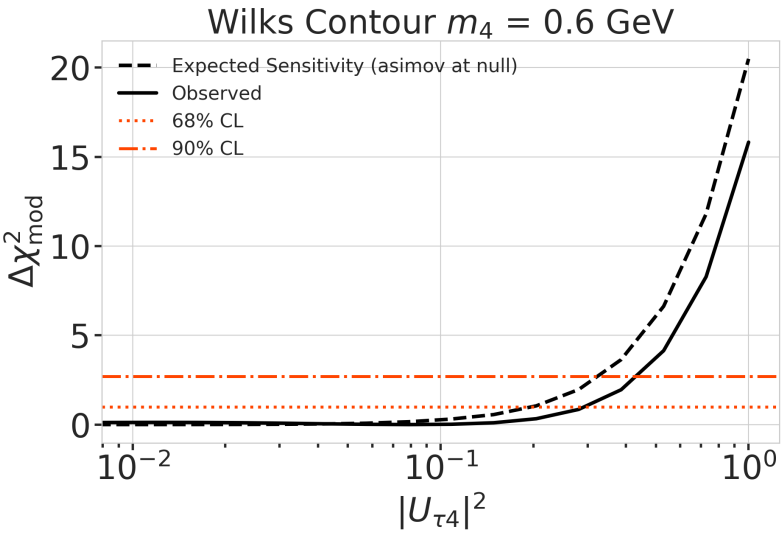

Figure 6.5: xx

fix caption for this figure

make plot with BFPs and limit, comparing to upper limits from other experiments

6.4.3 Data/MC Agreement

specify which they are, once I have them

At the BFP, the agreement between the data and simulation is probed by comparing the 1-dimensional analysis distributions for PID, energy, and cosine of the zenith angle. As an example, two distributions for the 0.6 GeV mass sample are shown in Figure **??**. The data is compared to the total MC expectation, which is also split up into its composing parts. Good agreement can be observed in the pull distributions and is quantified by a reduced χ^2, which is close to 1.0 for all distributions. The reduced χ^2 for all investigated distributions is listed in Table **??**, while the distributions themselves can be found in Section **??**.

add 1-d data/mc agreement for example mass sample (0.6?) and all 3 analysis variables

add table with reduced chi2 for all 1-d distributions

Appendix

A

Heavy Neutral Lepton Signal Simulation

A.1 Model Independent Simulation Distributions

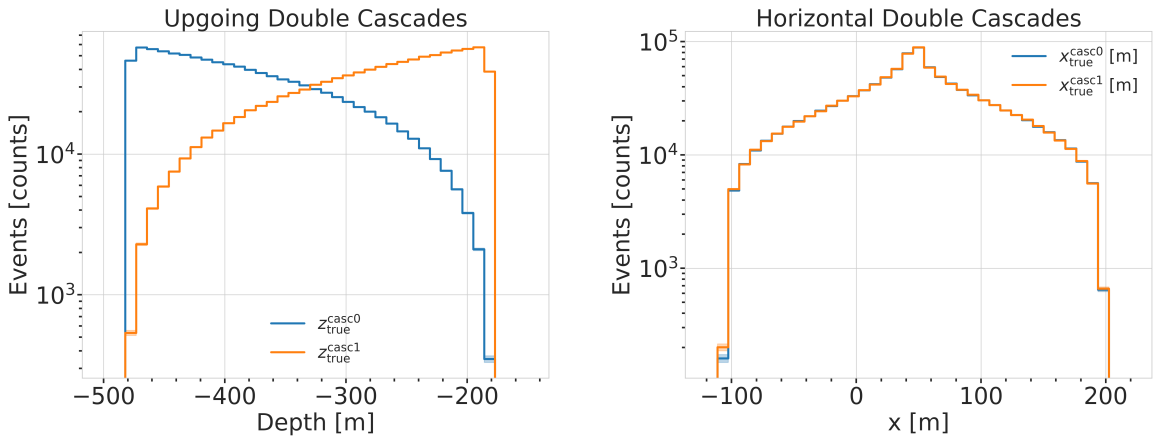

Figure A.1: Generation level distributions of the simplistic simulation sets. Vertical positions (left) and horizontal positions (right) of both sets are shown.

- Re-make plot with x,y for horizontal set one plot!
- Re-make plot with x, y, z for both cascades in one.
- Re-arrange plots in a more sensible way.

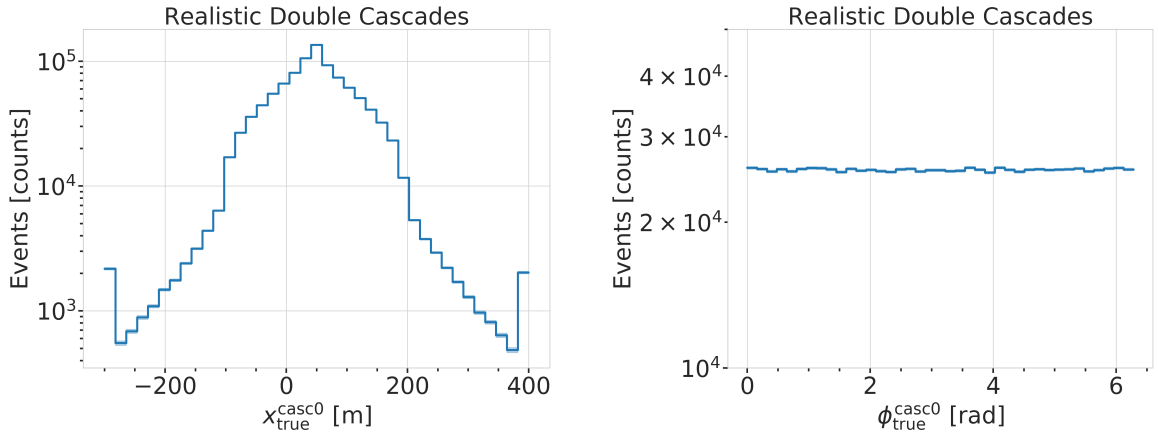

Figure A.2: Generation level distributions of the realistic simulation set. Shown are the cascade x, y, z positions (left) and direction angles (right).

A.2 Model Dependent Simulation Distributions

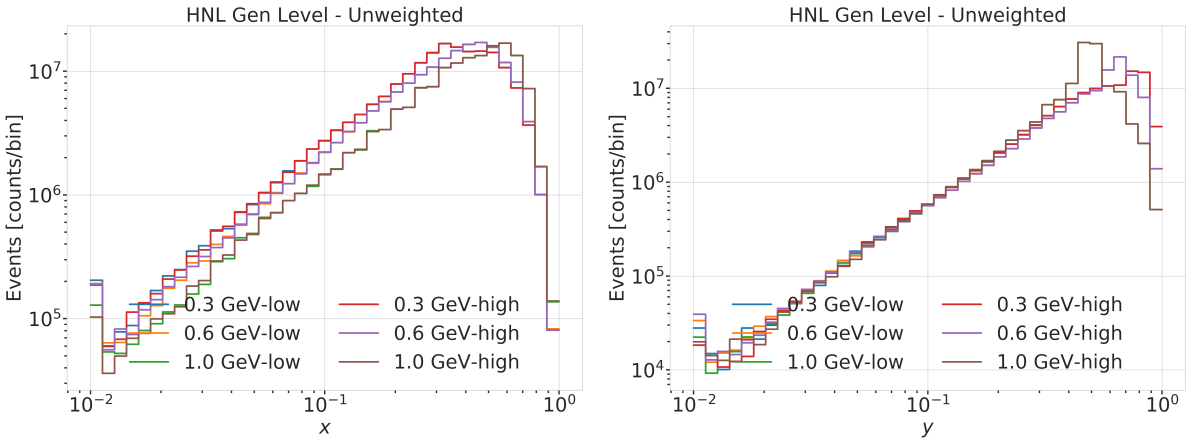

(a) Bjorken x

(b) Bjorken y

Figure A.3: Generation level distributions of the model dependent simulation.

B

Analysis Checks

B.1 Minimization Robustness

Figure B.1 shows additional Asimov inject/recover tests for the 0.3 GeV and the 1.0 GeV mass sets. The tests were described in Section 6.3.1.

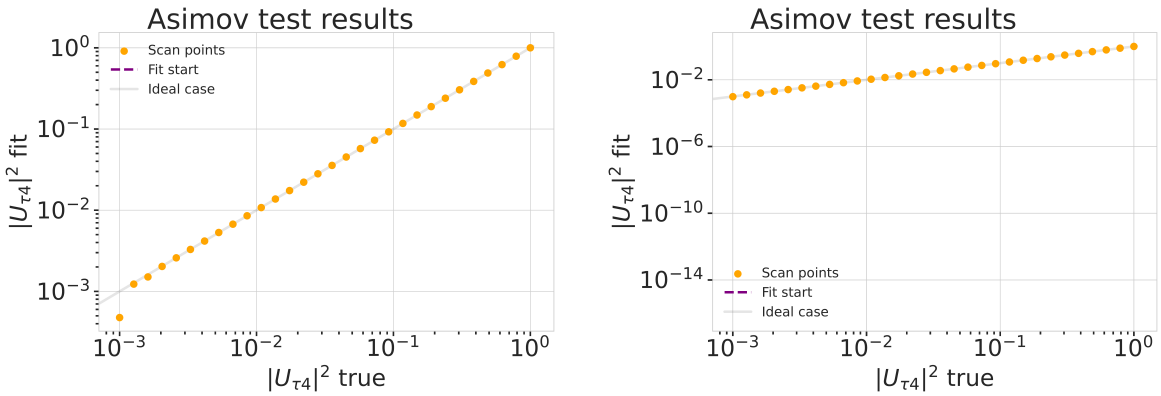

Figure B.1: Asimov inject/recover test for the 0.3 GeV (left) and the 1.0 GeV (right) mass sets. Mixing values between 10^{-3} and 10^{0} are injected and fit back with the full analysis chain. The injected parameter is always recovered within the statistical uncertainty.

B.1.1 Ensemble Tests

Figure B.2 shows additional TS distributions from pseudo-data trials and the observed TS from the fit to the data for the ensemble for the 0.3 GeV and the 1.0 GeV mass sets. The tests were described in Section 6.3.2.

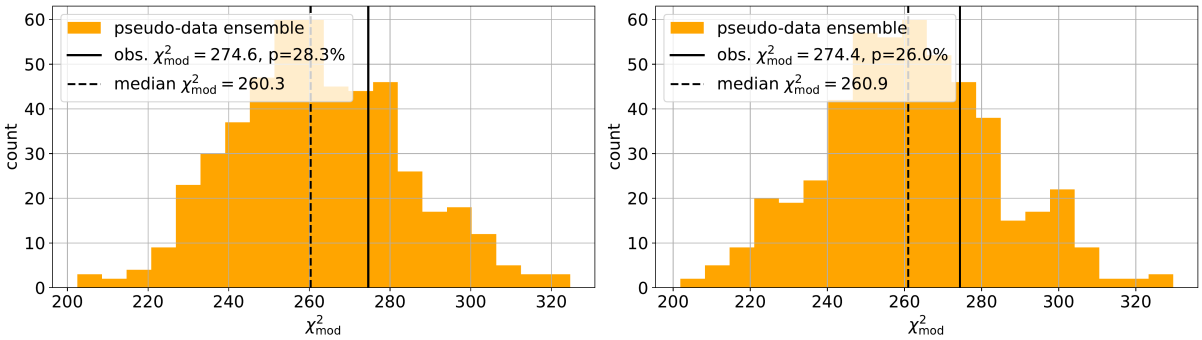

Figure B.2: Observed fit TS and TS distribution from pseudo-data trials for the 0.3 GeV (left) and the 1.0 GeV (right) mass set.

C

Analysis Results

C.0.1 Best Fit Nuisance Parameters

Table C.1: xx

Parameter	Nominal	Best Fit			Nominal - Best Fit		
		0.3 GeV	0.6 GeV	1.0 GeV	0.3 GeV	0.6 GeV	1.0 GeV
$\Delta\gamma_\nu$	0.000000	−0.007926	−0.006692	−0.006596	0.007926	0.006692	0.006596
Barr h_{π^+}	0.000000	−0.147475	−0.148481	−0.148059	0.147475	0.148481	0.148059
Barr i_{π^+}	0.000000	0.475448	0.513393	0.521626	−0.475448	−0.513393	−0.521626
Barr y_{K^+}	0.000000	0.076176	0.062893	0.057548	−0.076176	−0.062893	−0.057548
$\theta_{23}[^\circ]$	47.504700	48.117185	47.918758	48.010986	−0.612485	−0.414058	−0.506286
$\Delta m^2_{31}[\mathrm{eV}^2]$	0.002475	0.002454	0.002454	0.002455	0.000020	0.000021	0.000019
DIS	0.000000	−0.248709	−0.223302	−0.215666	0.248709	0.223302	0.215666
N_ν	1.000000	0.889149	0.889055	0.889559	0.110851	0.110945	0.110441
$\lvert U_{\tau 4}\rvert^2$	0.100000	0.003019	0.080494	0.106141	0.096981	0.019506	−0.006141
ϵ_{DOM}	1.000000	1.021984	1.017789	1.016689	−0.021984	−0.017789	−0.016689
hole ice p_0	0.101569	−0.161341	−0.161051	−0.160129	0.262910	0.262620	0.261698
hole ice p_1	−0.049344	−0.073701	−0.075596	−0.076261	0.024357	0.026252	0.026917
ice absorption	1.000000	0.943261	0.942463	0.942000	0.056739	0.057537	0.058000
ice scattering	1.050000	0.986152	0.989289	0.989438	0.063848	0.060711	0.060562
N_{bfr}	0.000000	0.746684	0.740255	0.736215	−0.746684	−0.740255	−0.736215
$M_{\mathrm{A,QE}}$	0.000000	−0.170528	−0.128150	−0.120345	0.170528	0.128150	0.120345
$M_{\mathrm{A,res}}$	0.000000	−0.125855	−0.080875	−0.070716	0.125855	0.080875	0.070716

sort these by type of nuisance parameter?

C.0.2 Best Fit Parameters and Limits

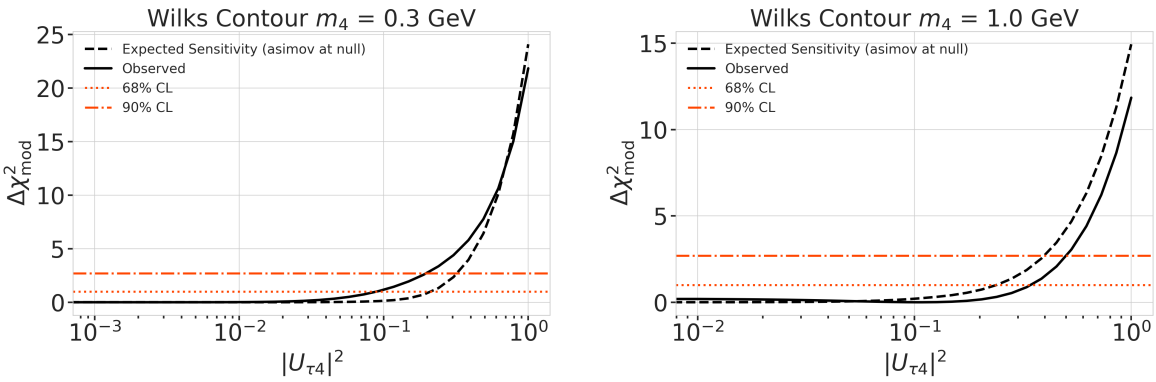
Wilks Contour m_4 = 0.3 GeV
Expected Sensitivity (asimov at null)
Observed
68% CL
90% CL
$\Delta\chi^2_{\text{mod}}$
$|U_{\tau 4}|^2$
Wilks Contour m_4 = 1.0 GeV
Expected Sensitivity (asimov at null)
Observed
68% CL
90% CL
$\Delta\chi^2_{\text{mod}}$
$|U_{\tau 4}|^2$

Figure C.1: xx

Bibliography

Here are the references in citation order.

[1] C. N. Yang and R. L. Mills. "Conservation of Isotopic Spin and Isotopic Gauge Invariance". In: *Physical Review* 96.1 (Oct. 1954), pp. 191–195. DOI: 10.1103/PhysRev.96.191 (cited on page 1).

[2] S. Weinberg. "A Model of Leptons". In: *Phys. Rev. Lett.* 19 (21 Nov. 1967), pp. 1264–1266. DOI: 10.1103/PhysRevLett.19.1264 (cited on page 1).

[3] S. L. Glashow. "Partial-symmetries of weak interactions". In: *Nuclear Physics* 22.4 (Feb. 1961), pp. 579–588. DOI: 10.1016/0029-5582(61)90469-2 (cited on page 1).

[4] R. Jackiw. "Physical Formulations: Elementary Particle Theory. Relativistic Groups and Analyticity. Proceedings of the eighth Nobel Symposium, Aspenäsgården, Lerum, Sweden, May 1968. Nils Svartholm, Ed. Interscience (Wiley), New York, and Almqvist and Wiksell, Stockholm, 1969. 400 pp., illus. $31.75." In: *Science* 168.3936 (1970), pp. 1196–1197. DOI: 10.1126/science.168.3936.1196.b (cited on page 1).

[5] P. Higgs. "Broken symmetries, massless particles and gauge fields". In: *Physics Letters* 12.2 (1964), pp. 132–133. DOI: https://doi.org/10.1016/0031-9163(64)91136-9 (cited on page 1).

[6] M. Gell-Mann. "A Schematic Model of Baryons and Mesons". In: *Resonance* 24 (1964), pp. 923–925 (cited on page 1).

[7] G. Zweig. "An SU(3) model for strong interaction symmetry and its breaking. Version 2". In: *DEVELOPMENTS IN THE QUARK THEORY OF HADRONS. VOL. 1. 1964 - 1978*. Ed. by D. B. Lichtenberg and S. P. Rosen. Feb. 1964, pp. 22–101 (cited on page 1).

[8] D. J. Gross and F. Wilczek. "Ultraviolet Behavior of Non-Abelian Gauge Theories". In: *PRL* 30.26 (June 1973), pp. 1343–1346. DOI: 10.1103/PhysRevLett.30.1343 (cited on page 1).

[9] C. Giunti and C. W. Kim. *Fundamentals of Neutrino Physics and Astrophysics*. Oxford University Press, Mar. 2007 (cited on page 1).

[10] M. D. Schwartz. *Quantum Field Theory and the Standard Model*. Cambridge University Press, 2013 (cited on page 1).

[11] A. Terliuk. "Measurement of atmospheric neutrino oscillations and search for sterile neutrino mixing with IceCube DeepCore". PhD thesis. Berlin, Germany: Humboldt-Universität zu Berlin, Mathematisch-Naturwissenschaftliche Fakultät, 2018. DOI: 10.18452/19304 (cited on pages 3, 8, 21).

[12] M. Thomson. *Modern particle physics*. Cambridge [u.a.]: Cambridge University Press, 2013, XVI, 554 S. (Cited on page 3).

[13] R. Davis, D. S. Harmer, and K. C. Hoffman. "Search for Neutrinos from the Sun". In: *Phys. Rev. Lett.* 20 (21 May 1968), pp. 1205–1209. DOI: 10.1103/PhysRevLett.20.1205 (cited on page 4).

[14] Y. Fukuda et al. "Evidence for Oscillation of Atmospheric Neutrinos". In: *Phys. Rev. Lett.* 81 (8 Aug. 1998), pp. 1562–1567. DOI: 10.1103/PhysRevLett.81.1562 (cited on page 4).

[15] Q. R. Ahmad and other. "Direct Evidence for Neutrino Flavor Transformation from Neutral-Current Interactions in the Sudbury Neutrino Observatory". In: *Phys. Rev. Lett.* 89 (1 June 2002), p. 011301. DOI: 10.1103/PhysRevLett.89.011301 (cited on page 4).

[16] M. Tanabashi et al. "Review of Particle Physics". In: *Phys. Rev. D* 98 (3 Aug. 2018), p. 030001. DOI: 10.1103/PhysRevD.98.030001 (cited on pages 4, 6, 9, 20).

[17] M. Aker et al. "Direct neutrino-mass measurement with sub-electronvolt sensitivity". In: *Nature Phys.* 18.2 (2022), pp. 160–166. DOI: 10.1038/s41567-021-01463-1 (cited on page 4).

[18] S. Alam et al. “Completed SDSS-IV extended Baryon Oscillation Spectroscopic Survey: Cosmological implications from two decades of spectroscopic surveys at the Apache Point Observatory”. In: *Phys. Rev. D* 103 (8 Apr. 2021), p. 083533. DOI: 10.1103/PhysRevD.103.083533 (cited on page 4).

[19] N. Aghanim et al. “Planck2018 results: VI. Cosmological parameters”. In: *Astronomy & Astrophysics* 641 (Sept. 2020), A6. DOI: 10.1051/0004-6361/201833910 (cited on page 4).

[20] P. Coloma et al. “GeV-scale neutrinos: interactions with mesons and DUNE sensitivity”. In: *Eur. Phys. J. C* 81.1 (2021), p. 78. DOI: 10.1140/epjc/s10052-021-08861-y (cited on pages 6, 11, 13, 27, 29, 30).

[21] M. Honda et al. “Atmospheric neutrino flux calculation using the NRLMSISE-00 atmospheric model”. In: *Phys. Rev. D* 92 (2 July 2015), p. 023004. DOI: 10.1103/PhysRevD.92.023004 (cited on pages 7, 34).

[22] A. Fedynitch et al. “Calculation of conventional and prompt lepton fluxes at very high energy”. In: *European Physical Journal Web of Conferences*. Vol. 99. European Physical Journal Web of Conferences. Aug. 2015, p. 08001. DOI: 10.1051/epjconf/20159908001 (cited on page 7).

[23] J. A. Formaggio and G. P. Zeller. “From eV to EeV: Neutrino cross sections across energy scales”. In: *Rev. Mod. Phys.* 84 (3 Sept. 2012), pp. 1307–1341. DOI: 10.1103/RevModPhys.84.1307 (cited on page 9).

[24] S. Bilenky and B. Pontecorvo. “Lepton mixing and neutrino oscillations”. In: *Physics Reports* 41.4 (1978), pp. 225–261. DOI: 10.1016/0370-1573(78)90095-9 (cited on page 8).

[25] P. A. M. Dirac. “The Quantum Theory of the Emission and Absorption of Radiation”. In: *Proceedings of the Royal Society of London Series A* 114.767 (Mar. 1927), pp. 243–265. DOI: 10.1098/rspa.1927.0039 (cited on page 9).

[26] T. Yanagida. “Horizontal Symmetry and Masses of Neutrinos”. In: *Progress of Theoretical Physics* 64.3 (Sept. 1980), pp. 1103–1105. DOI: PTP.64.1103 (cited on page 10).

[27] P. Astier et al. “Search for heavy neutrinos mixing with tau neutrinos”. In: *Phys. Lett. B* 506 (2001), pp. 27–38. DOI: 10.1016/S0370-2693(01)00362-8 (cited on page 11).

[28] R. Acciarri et al. “New Constraints on Tau-Coupled Heavy Neutral Leptons with Masses mN=280–970 MeV”. In: *Phys. Rev. Lett.* 127.12 (2021), p. 121801. DOI: 10.1103/PhysRevLett.127.121801 (cited on page 11).

[29] J. Orloff, A. N. Rozanov, and C. Santoni. “Limits on the mixing of tau neutrino to heavy neutrinos”. In: *Phys. Lett. B* 550 (2002), pp. 8–15. DOI: 10.1016/S0370-2693(02)02769-7 (cited on page 11).

[30] I. Boiarska et al. “Blast from the past: constraints from the CHARM experiment on Heavy Neutral Leptons with tau mixing”. In: (July 2021) (cited on page 11).

[31] P. Abreu et al. “Search for neutral heavy leptons produced in Z decays”. In: *Z. Phys. C* 74 (1997). [Erratum: Z.Phys.C 75, 580 (1997)], pp. 57–71. DOI: 10.1007/s002880050370 (cited on page 11).

[32] P. Coloma et al. “Double-Cascade Events from New Physics in Icecube”. In: *Phys. Rev. Lett.* 119.20 (2017), p. 201804. DOI: 10.1103/PhysRevLett.119.201804 (cited on pages 10, 11).

[33] P. Coloma. “Icecube/DeepCore tests for novel explanations of the MiniBooNE anomaly”. In: *Eur. Phys. J. C* 79.9 (2019), p. 748. DOI: 10.1140/epjc/s10052-019-7256-8 (cited on page 11).

[34] M. G. Aartsen et al. “The IceCube Neutrino Observatory: instrumentation and online systems”. In: *Journal of Instrumentation* 12.3 (Mar. 2017), P03012. DOI: 10.1088/1748-0221/12/03/P03012 (cited on pages 15, 17, 38).

[35] P. B. Price, K. Woschnagg, and D. Chirkin. “Age vs depth of glacial ice at South Pole”. In: *Geophysical Research Letters* 27.14 (2000), pp. 2129–2132. DOI: https://doi.org/10.1029/2000GL011351 (cited on page 16).

[36] R. Abbasi et al. “In-situ estimation of ice crystal properties at the South Pole using LED calibration data from the IceCube Neutrino Observatory”. In: *The Cryosphere Discussions* 2022 (2022), pp. 1–48. DOI: 10.5194/tc-2022-174 (cited on page 16).

[37] R. Abbasi et al. “The IceCube data acquisition system: Signal capture, digitization, and timestamping”. In: *Nuclear Instruments and Methods in Physics Research Section A: Accelerators, Spectrometers, Detectors and Associated Equipment* 601.3 (2009), pp. 294–316. DOI: https://doi.org/10.1016/j.nima.2009.01.001 (cited on pages 16, 17, 38).

[38] M. G. Aartsen et al. “Energy Reconstruction Methods in the IceCube Neutrino Telescope”. In: *JINST* 9 (2014), P03009. DOI: 10.1088/1748-0221/9/03/P03009 (cited on pages 17, 49).

[39] J. Feintzeig. “Searches for Point-like Sources of Astrophysical Neutrinos with the IceCube Neutrino Observatory”. PhD thesis. University of Wisconsin, Madison, Jan. 2014 (cited on pages 17, 46, 60).

[40] N. Kulacz. “In Situ Measurement of the IceCube DOM Efficiency Factor Using Atmospheric Minimum Ionizing Muons”. MA thesis. University of Alberta, 2019 (cited on pages 17, 46, 60).

[41] R. Abbasi et al. “The design and performance of IceCube DeepCore”. In: *Astropart. Phys.* 35.10 (2012), pp. 615–624. DOI: 10.1016/j.astropartphys.2012.01.004 (cited on pages 17, 37, 38).

[42] P. A. Cherenkov. “Visible Radiation Produced by Electrons Moving in a Medium with Velocities Exceeding that of Light”. In: *Phys. Rev.* 52 (4 Aug. 1937), pp. 378–379. DOI: 10.1103/PhysRev.52.378 (cited on page 18).

[43] I. Frank and I. Tamm. “Coherent visible radiation from fast electrons passing through matter”. In: *C. R. Acad. Sci. USSR* 14 (1937), pp. 109–114 (cited on pages 18, 19).

[44] I. Tamm. “Radiation Emitted by Uniformly Moving Electrons”. In: *Selected Papers*. Ed. by B. M. Bolotovskii, V. Y. Frenkel, and R. Peierls. Berlin, Heidelberg: Springer Berlin Heidelberg, 1991, pp. 37–53. DOI: 10.1007/978-3-642-74626-0_3 (cited on pages 18, 19).

[45] L. Rädel and C. Wiebusch. “Calculation of the Cherenkov light yield from low energetic secondary particles accompanying high-energy muons in ice and water with Geant4 simulations”. In: *Astroparticle Physics* 38 (Oct. 2012), pp. 53–67. DOI: 10.1016/j.astropartphys.2012.09.008 (cited on pages 19, 35).

[46] D. Chirkin and W. Rhode. “Propagating leptons through matter with Muon Monte Carlo (MMC)”. In: (July 2004) (cited on pages 19, 20).

[47] L. Raedel. “Simulation Studies of the Cherenkov Light Yield from Relativistic Particles in High-Energy Neutrino Telescopes with Geant4”. MA thesis. Aachen, Germany: Rheinisch-Westfälischen Technischen Hochschule, 2012 (cited on pages 19, 20).

[48] S. Agostinelli et al. “Geant4—a simulation toolkit”. In: *Nucl. Instr. Meth. Phys. Res.* 506.3 (July 2003), pp. 250–303. DOI: 10.1016/s0168-9002(03)01368-8 (cited on pages 20, 35).

[49] T. Gabriel et al. “Energy dependence of hadronic activity”. In: *Nuclear Instruments and Methods in Physics Research Section A: Accelerators, Spectrometers, Detectors and Associated Equipment* 338.2 (1994), pp. 336–347. DOI: https://doi.org/10.1016/0168-9002(94)91317-X (cited on page 20).

[50] L. Fischer. https://github.com/LeanderFischer/icetray_double_cascade_generator_functions (cited on page 23).

[51] R. Abbasi et al. “LeptonInjector and LeptonWeighter: A neutrino event generator and weighter for neutrino observatories”. In: *Comput. Phys. Commun.* 266 (2021), p. 108018. DOI: 10.1016/j.cpc.2021.108018 (cited on page 26).

[52] J. Alwall et al. “The automated computation of tree-level and next-to-leading order differential cross sections, and their matching to parton shower simulations”. In: *JHEP* 07 (2014), p. 079. DOI: 10.1007/JHEP07(2014)079 (cited on page 27).

[53] C. Argüelles. https://github.com/arguelles/NuXSSplMkr (cited on page 27).

[54] J.-M. Levy. “Cross-section and polarization of neutrino-produced tau’s made simple”. In: *J. Phys. G* 36 (2009), p. 055002. DOI: 10.1088/0954-3899/36/5/055002 (cited on page 28).

[55] E. Tiesinga et al. “CODATA recommended values of the fundamental physical constants: 2018”. In: *Rev. Mod. Phys.* 93 (2 July 2021), p. 025010. DOI: 10.1103/RevModPhys.93.025010 (cited on page 29).

[56] https://github.com/icecube/pisa (cited on pages 31, 58).

[57] R. Abbasi et al. “Measurement of atmospheric neutrino mixing with improved IceCube DeepCore calibration and data processing”. In: *Phys. Rev. D* 108 (1 July 2023), p. 012014. DOI: 10.1103/PhysRevD.108.012014 (cited on pages 33, 40, 43–45).

[58] C. Andreopoulos et al. “The GENIE Neutrino Monte Carlo Generator: Physics and User Manual”. In: (2015) (cited on pages 35, 45).

[59] M. Glück, E. Reya, and A. Vogt. “Dynamical parton distributions revisited”. In: *The European Physical Journal C* 5 (Sept. 1998), pp. 461–470. DOI: 10.1007/s100529800978 (cited on page 35).

[60] A. Bodek and U. K. Yang. “Higher twist, xi(omega) scaling, and effective LO PDFs for lepton scattering in the few GeV region”. In: *Journal of Physics G: Nuclear and Particle Physics* 29.8 (2003), p. 1899. DOI: 10.1088/0954-3899/29/8/369 (cited on page 35).

[61] J.-H. Koehne et al. “PROPOSAL: A tool for propagation of charged leptons”. In: *Computer Physics Communications* 184.9 (2013), pp. 2070–2090. DOI: https://doi.org/10.1016/j.cpc.2013.04.001 (cited on page 35).

[62] Y. Becherini et al. “A parameterisation of single and multiple muons in the deep water or ice”. In: *Astroparticle Physics* 25.1 (2006), pp. 1–13. DOI: https://doi.org/10.1016/j.astropartphys.2005.10.005 (cited on page 35).

[63] D. Heck et al. “CORSIKA: A Monte Carlo code to simulate extensive air showers”. In: (Feb. 1998) (cited on page 35).

[64] T. K. Gaisser. “Spectrum of cosmic-ray nucleons, kaon production, and the atmospheric muon charge ratio”. In: *Astropart. Phys.* 35 (2012), pp. 801–806. DOI: 10.1016/j.astropartphys.2012.02.010 (cited on page 35).

[65] R. Engel et al. “The hadronic interaction model Sibyll – past, present and future”. In: *EPJ Web Conf.* 145 (2017). Ed. by B. Pattison, p. 08001. DOI: 10.1051/epjconf/201614508001 (cited on page 35).

[66] C. Kopper et al. https://github.com/claudiok/clsim (cited on page 36).

[67] D. Chirkin et al. “Photon Propagation using GPUs by the IceCube Neutrino Observatory”. In: *2019 15th International Conference on eScience (eScience)*. 2019, pp. 388–393. DOI: 10.1109/eScience.2019.00050 (cited on page 36).

[68] M. G. Aartsen et al. “Measurement of South Pole ice transparency with the IceCube LED calibration system”. In: *Nucl. Instrum. Meth. A* 711 (2013), pp. 73–89. DOI: 10.1016/j.nima.2013.01.054 (cited on page 36).

[69] A. Trettin. “Search for eV-scale sterile neutrinos with IceCube DeepCore”. PhD thesis. Berlin, Germany: Humboldt-Universität zu Berlin, Mathematisch-Naturwissenschaftliche Fakultät, 2023. DOI: https://github.com/atrettin/PhD-Thesis (cited on pages 36, 37, 46).

[70] G. Mie. “Beiträge zur Optik trüber Medien, speziell kolloidaler Metallösungen”. In: *Annalen der Physik* 330.3 (1908), pp. 377–445. DOI: https://doi.org/10.1002/andp.19083300302 (cited on page 36).

[71] L. G. Henyey and J. L. Greenstein. “Diffuse radiation in the Galaxy.” In: *apj* 93 (Jan. 1941), pp. 70–83. DOI: 10.1086/144246 (cited on page 36).

[72] S. Fiedlschuster. “The Effect of Hole Ice on the Propagation and Detection of Light in IceCube”. In: (Apr. 2019) (cited on page 36).

[73] M. G. Aartsen et al. “In-situ calibration of the single-photoelectron charge response of the IceCube photomultiplier tubes”. In: *Journal of Instrumentation* 15.6 (June 2020), P06032. DOI: 10.1088/1748-0221/15/06/P06032 (cited on page 37).

[74] M. Larson. “Simulation and Identification of Non-Poissonian Noise Triggers in the IceCube Neutrino Detector”. Available at https://ir.ua.edu/handle/123456789/1927. MA thesis. University of Alabama, Tuscaloosa, AL, USA, 2013 (cited on page 37).

[75] M. Larson. “A Search for Tau Neutrino Appearance with IceCube-DeepCore”. available at https://discoverycenter.nbi.ku.dk/teaching/thesis_page/mjlarson_thesis.pdf. PhD thesis. University of Copenhagen, Denmark, 2018 (cited on page 37).

[76] E. Lohfink. “Testing nonstandard neutrino interaction parameters with IceCube-DeepCore”. PhD thesis. Mainz, Germany: Johannes Gutenberg-Universität Mainz, Fachbereich für Physik, Mathematik und Informatik, 2023. DOI: http://doi.org/10.25358/openscience-9288 (cited on page 37).

[77] M. G. Aartsen et al. “The IceCube Neutrino Observatory: Instrumentation and Online Systems”. In: *JINST* 12.03 (2017), P03012. DOI: 10.1088/1748-0221/12/03/P03012 (cited on page 37).

[78] J. H. Friedman. “Stochastic gradient boosting”. In: *Computational Statistics & Data Analysis* 38 (2002), pp. 367–378 (cited on page 39).

[79] R. Abbasi et al. “Low energy event reconstruction in IceCube DeepCore”. In: *Eur. Phys. J. C* 82.9 (2022), p. 807. DOI: 10.1140/epjc/s10052-022-10721-2 (cited on page 40).

[80] S. Yu and J. Micallef. “Recent neutrino oscillation result with the IceCube experiment”. In: *38th International Cosmic Ray Conference*. July 2023 (cited on pages 40, 58).

[81] S. Yu and on behalf of the IceCube collaboration. “Direction reconstruction using a CNN for GeV-scale neutrinos in IceCube”. In: *Journal of Instrumentation* 16.11 (2021), p. C11001. DOI: 10.1088/1748-0221/16/11/C11001 (cited on page 41).

[82] J. Micallef. https://github.com/jessimic/LowEnergyNeuralNetwork (cited on page 41).

[83] M. Huennefeld. “Deep Learning in Physics exemplified by the Reconstruction of Muon-Neutrino Events in IceCube”. In: *PoS* ICRC2017 (2017), p. 1057. DOI: 10.22323/1.301.1057 (cited on page 41).

[84] H. Dembinski et al. “Data-driven model of the cosmic-ray flux and mass composition from 10 GeV to 10^{11} GeV”. In: *PoS* ICRC2017 (2017), p. 533. DOI: 10.22323/1.301.0533 (cited on page 44).

[85] G. D. Barr et al. “Uncertainties in atmospheric neutrino fluxes”. In: *Phys. Rev. D* 74 (9 Nov. 2006), p. 094009. DOI: 10.1103/PhysRevD.74.094009 (cited on page 44).

[86] J. Evans et al. “Uncertainties in atmospheric muon-neutrino fluxes arising from cosmic-ray primaries”. In: *Phys. Rev. D* 95 (2 Jan. 2017), p. 023012. DOI: 10.1103/PhysRevD.95.023012 (cited on pages 44, 60).

[87] A. Fedynitch et al. https://github.com/afedynitch/MCEq (cited on page 44).

[88] G. D. Barr et al. “Uncertainties in Atmospheric Neutrino Fluxes”. In: *Phys. Rev. D* 74 (2006), p. 094009. DOI: 10.1103/PhysRevD.74.094009 (cited on page 44).

[89] F. Riehn et al. “Hadronic interaction model sibyll 2.3d and extensive air showers”. In: *Phys. Rev. D* 102 (6 Sept. 2020), p. 063002. DOI: 10.1103/PhysRevD.102.063002 (cited on page 44).

[90] A. Cooper-Sarkar, P. Mertsch, and S. Sarkar. “The high energy neutrino cross-section in the Standard Model and its uncertainty”. In: *JHEP* 08 (2011), p. 042. DOI: 10.1007/JHEP08(2011)042 (cited on page 45).

[91] Q. Wu et al. “A precise measurement of the muon neutrino–nucleon inclusive charged current cross section off an isoscalar target in the energy range 2.5<E<40 GeV by NOMAD”. In: *Physics Letters B* 660.1 (2008), pp. 19–25. DOI: https://doi.org/10.1016/j.physletb.2007.12.027 (cited on page 45).

[92] M. M. Tzanov. “Precise measurement of neutrino and anti-neutrino differential cross sections on iron”. PhD thesis. University of Pittsburgh, Pennsylvania, Jan. 2005 (cited on page 45).

[93] W. G. Seligman. “A next-to-leading-order QCD analysis of neutrino-iron structure functions at the Tevatron”. PhD thesis. Columbia University, New York, Aug. 1997 (cited on page 45).

[94] Rongen, Martin. “Measuring the optical properties of IceCube drill holes”. In: *EPJ Web of Conferences* 116 (2016), p. 06011. DOI: 10.1051/epjconf/201611606011 (cited on page 46).

[95] L. Fischer, R. Naab, and A. Trettin. “Treating detector systematics via a likelihood free inference method”. In: *Journal of Instrumentation* 18.10 (2023), P10019. DOI: 10.1088/1748-0221/18/10/P10019 (cited on page 47).

[96] R. Abbasi et al. “Measurement of Astrophysical Tau Neutrinos in IceCube’s High-Energy Starting Events”. In: *arXiv e-prints* (Nov. 2020) (cited on page 49).

[97] M. Usner. “Search for Astrophysical Tau-Neutrinos in Six Years of High-Energy Starting Events in the IceCube Detector”. PhD thesis. Berlin, Germany: Humboldt-Universität zu Berlin, Mathematisch-Naturwissenschaftliche Fakultät, 2018. DOI: 10.18452/19458 (cited on page 49).

[98] P. Hallen. “On the Measurement of High-Energy Tau Neutrinos with IceCube”. MA thesis. Aachen, Germany: RWTH Aachen Universisty, 2013 (cited on page 49).

[99] M. G. Aartsen et al. “Computational techniques for the analysis of small signals in high-statistics neutrino oscillation experiments”. In: *Nucl. Instrum. Meth. A* 977 (2020), p. 164332. DOI: 10.1016/j.nima.2020.164332 (cited on page 58).

[100] R. S. Nickerson. “Confirmation Bias: A Ubiquitous Phenomenon in Many Guises”. In: *Review of General Psychology* 2 (1998), pp. 175–220 (cited on page 61).

[101] H. Dembinski et al. *scikit-hep/iminuit: v2.17.0*. Version v2.17.0. Sept. 2022. DOI: 10.5281/zenodo.7115916 (cited on page 61).

[102] F. James and M. Roos. “Minuit: A System for Function Minimization and Analysis of the Parameter Errors and Correlations”. In: *Comput. Phys. Commun.* 10 (1975), pp. 343–367. DOI: 10.1016/0010-4655(75)90039-9 (cited on page 61).

[103] S. S. Wilks. “The Large-Sample Distribution of the Likelihood Ratio for Testing Composite Hypotheses”. In: *The Annals of Mathematical Statistics* 9.1 (1938), pp. 60–62. DOI: 10.1214/aoms/1177732360 (cited on page 63).